Theses and Dissertations

9-14-2017

Special Features of the Air-to-Space Neutron Transport Problem

Whitman T. Dailey

SPECIAL FEATURES OF THE AIR-TO-SPACE NEUTRON TRANSPORT PROBLEM

DISSERTATION

Whitman T. Dailey, Major, USAF

AFIT/ENP/DS-17-S-022

DEPARTMENT OF THE AIR FORCE

AIR UNIVERSITY

AIR FORCE INSTITUTE OF TECHNOLOGY

Wright-Patterson Air Force Base, Ohio

APPROVED FOR PUBLIC RELEASE; DISTRIBUTION UNLIMITED

AFIT/ENP/DS-17-S-022

SPECIAL FEATURES OF THE AIR-TO-SPACE NEUTRON
TRANSPORT PROBLEM

DISSERTATION

Presented to the Faculty

Graduate School of Engineering and Management

Air Force Institute of Technology

Air University

Air Education and Training Command

In Partial Fulfillment of the Requirements for the

Degree of Doctor of Philosophy

Whitman T. Dailey, BS, MS
Major, USAF

September 2017

AFIT/ENP/DS-17-S-022

SPECIAL FEATURES OF THE AIR-TO-SPACE NEUTRON TRANSPORT PROBLEM

Whitman T. Dailey, BS, MS
Major, USAF

Committee Membership:

Kirk A. Mathews, PhD
Chairman

Lt Col Briana J. Singleton, PhD
Member

David W. Gerts, PhD
Member

William P. Baker, PhD
Member

ADEDJI B. BADIRU, PhD
Dean, Graduate School of Engineering and Management

AFIT/ENP/DS-17-S-022

Abstract

Special features of the air-to-space neutron transport problem are identified, characterized, and quantified to provide information on features that should be included in Monte Carlo simulations to obtain accurate predictions. Currently available codes and tools for Monte Carlo neutron transport calculations do not provide an adequate (in accuracy nor precision nor efficiency) framework for practical transport calculations in the context of the air-to-space neutron transport problem. A new Fortran code, High Altitude Transport to Space for Neutrons (HATS-n), is developed and tested to perform high fidelity Monte Carlo neutron transport calculations for this class of problems. Special features of the air-to-space neutron transport are identified and categorized: The influence of relative motions, the influence of gravity, the influence of the implementation of the atmosphere model, and the influence of radioactive decay of free neutrons. Each special feature is examined individually and methods and procedures are developed for research and practical implementations. Finally, the features are demonstrated in concert using the new HATS-n code.

For her... And the two of them.

Acknowledgements

I would like to sincerely thank my research advisor, Dr. Kirk Mathews, for his guidance, insight, and patience throughout the course of this research: His ability to guide me to the right questions was instrumental in the successful completion of this dissertation. I would also like to thank the members of my committee for their support and interest on this subject: I look forward to continuing the work with you all. Additionally, the faculty, staff, and students of AFIT/ENP provided invaluable aid and support throughout this research. My greatest debt of gratitude is owed to my family for their patience and sacrifice during this all-too-long process. I am lucky to have a loving wife and two tough boys to support me and keep me focused on what is most important.

Table of Contents

List of Figures

xviii

List of Tables

I. Introduction

The Air-to-Space Neutron Transport Problem

A point source in space and time, in the earth's atmosphere or at some distance above it, emits neutrons that may reach a satellite in orbit. Upon emission from the source or a subsequent interaction in the atmosphere, the probability of the *next* interaction occurring at the satellite may be computed. The distribution in time, energy, and direction of neutrons arriving at the satellite is of interest. The general transport problem is illustrated in Figure 1.
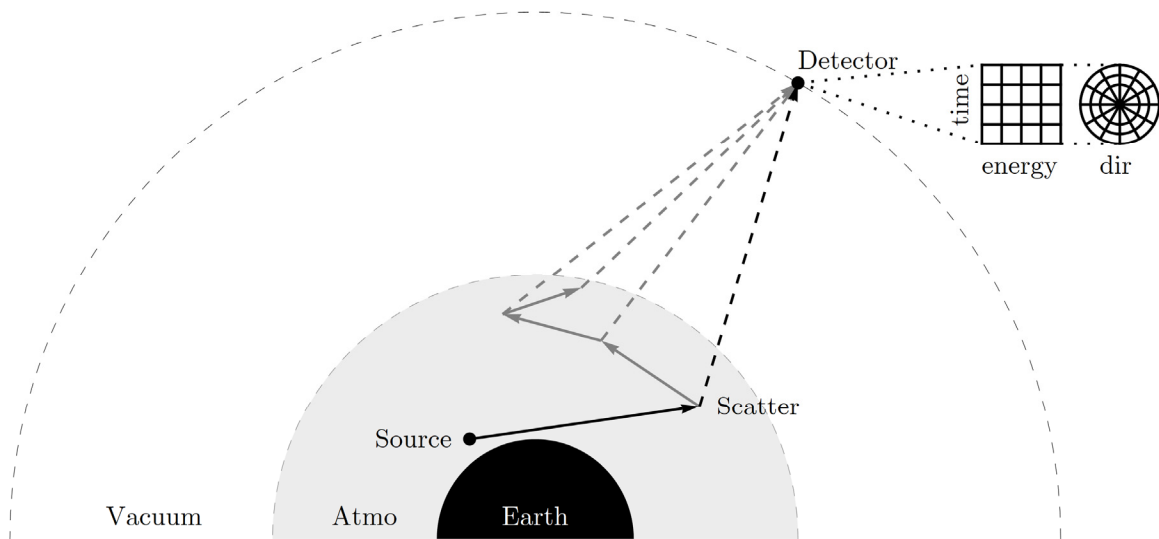
Figure 1: The air-to-space neutron transport problem.

Monte Carlo for the Air to Space Neutron Transport Problem

An estimate of the time-energy-direction distribution of neutrons at the satellite may be obtained using Monte Carlo methods to generate neutron histories that may result in contributions to neutron current at the satellite. The contributions accumulated over a large enough number of histories may be used to describe the expected distribution of neutrons in time, energy, and direction. The general procedure for simulating a neutron history consists of six steps: start a neutron, move the neutron, compute a next-event probability, interact the neutron, kill or continue the neutron, and then tally the history:

1. *Start Neutron*: A neutron is created at the location of the source at time zero. The energy and direction are chosen correlated with the properties of the source. A first-flight contribution to the detector may be computed at this point if a sampled (rather than directly computed) first-flight estimate is desired.

2. *Move Neutron*: The neutron is transported through the atmosphere to the location of the next interaction. This step is sometimes referred to as raytracing. Sample an optical thickness to the next interaction and transform that optical thickness to a geometric distance along a path in the atmosphere which in turn determines the location of the next interaction. This step involves inversion or root-solving of a function that describes the optical thickness of the transport medium.

3. *Next-Event Neutron*: Compute the probability that the interaction (to which the neutron has just arrived) will result in a scattered *pseudo-particle* that will intercept the satellite. If the properties of scatter (properties of the neutron and interaction target) and the properties of the detector allow an intercept, compute the properties of the intercept

(time of flight, launch and arrival direction, launch and arrival energy). The contribution to record at the detector is then adjusted by the probability of scatter into the required direction for intercept, the probability of escaping the atmosphere along that path, and divergence of the pseudo-particle on the flight to the detector.

4. *Interact Neutron*: Returning to the neutron at the point of its next interaction, but before the interaction which generated the pseudo-particle has occurred, choose properties of the interaction correlated with the properties of the neutron, interaction target, and scattering model. Use the selected properties of the interaction to determine the direction and energy of the neutron after the interaction.

5. *Kill Neutron*: When the neuron has moved outside the range of the problem of interest (absorption, leakage, time or energy out of range, or other kill criteria), the history is terminated. If the kill criteria are not met, the history continues by returning to the *Move Neutron* step.

6. *Tally Neutron*: The contribution(s) recorded during the history are processed and added to the totals for the simulation. It is important to distinguish this as a step for each history, and *not for each contribution*. Even if multiple contributions are computed during a history, together they represent a *single* estimate of the expected value.

This description of the procedure includes few, if any, overt features distinguishing it from other general transport problems to which many established and available production codes could be applied. However, when transport calculations for the air-to-space problem are performed using a production code, such as MCNP, the result is degraded to some extent by the special features of the air-to-space problem that are not modeled, or only partially modeled, in such a code. The degradation is a result of the underlying

transport assumptions made in the development of any such code based on the specific problem set for which the code was designed. In the case of most production codes, the problem of interest is reactor design, criticality analysis, or shielding. The scale of these problems is typically measured in meters and fractions of seconds, and a set of *traditional* neutron transport assumptions are applied.

Traditional Neutron Transport Assumptions

In *Computational Methods of Neutron Transport* (Lewis & Miller, 1993, pp. 3-4), the authors state: "*The following assumptions are made in the derivation of the neutron transport equation*:

1. *Particles may be considered as points. …*
2. *Particles travel in straight lines between collisions. …*
3. *Particle-particle interactions may be neglected. …*
4. *Collisions may be considered instantaneous. …*
5. *The material properties are assumed to be isotropic. …*
6. *The properties of nuclei and the compositions of materials under consideration are assumed to be known and time-independent unless explicitly stated otherwise. …*
7. *Only the expected or mean value of the particle density distribution is considered. …*"

Additional assumptions are made to simplify most codes:

8. The source, scattering medium, and point at which the flux is to be estimated are stationary in the same reference frame.

9. The composition, density, and temperature are uniform within regions that define the problem.
10. Radioactive decay of neutrons is not significant in the scale of time relevant to the problem.

Assumptions 2, 8, 9, and 10 are not valid for the air-to-space transport problem studied here. The others do apply.

Distance and Time Scales

The single feature that most differentiates the air-to-space neutron transport problem from conventional problems is the magnitude of the distance and time scales considered, and their range of variation within the phase space of the problem.

The minimum energy for a neutron at the surface of the earth to reach a detector at geosynchronous altitude, 35,786 kilometers (km), is approximately 0.56 electronvolts (eV). With this energy, and assuming constant velocity (no gravity), the time of flight to a point directly overhead at geosynchronous altitude is nearly an hour. Accounting for gravity, the neutron trades kinetic energy for altitude throughout its flight, and the time of flight is actually more than four and a half hours. For a 20 MeV neutron, the time of flight to reach the same point is approximately 0.57 seconds, and neglecting gravity introduces an error in this time of flight of only 0.000007%.

At sea-level, the mean free path of a neutron ranges from tens to hundreds of meters depending on neutron kinetic energy. At higher altitude, 86 km for

example, the mean free path is longer by six orders of magnitude due to the lower density of the transport medium. Other transport problems may include variation in mean free path on this scale (e.g. a shielding problem with a shield and air) but those problems are generally easily partitioned into regions where variation in the mean free path is small in each region (e.g. the shield and the air). In the case of the atmosphere, the variation in mean free path is continuous (with density and composition of the atmosphere) through the full thickness of the atmosphere. Partitioning the scattering medium into regions of constant composition and density introduces computational overhead, discretization error, and artifacts into result of the transport calculation.

The scale of the air-to-space problem ranges from meters to tens of thousands of kilometers and fractions of a second to hours. Also, the problem is not easily partitioned into geometric regions over which the scale may be considered constant. As a result, the validity of some of the assumptions traditionally applied in transport calculations becomes questionable.

Relative Motion

The components of the air-to-space problem (source, atmosphere, satellite) all move independently of one another and, given the distance and time scales considered in the air-to-space problem, this motion may not be negligible. A neutron source can move at speeds on the order of 10 km/s. The atmosphere rotates with the surface of the earth (velocity is dependent on altitude and

6

latitude). The satellite has velocity depending on the properties of its orbit (approximately 3 km/s for satellites in geosynchronous orbits, and higher for lower orbits). Additionally, particles in the scattering medium are subject to random thermal motion and motion due to winds.

Line of Sight and Flight Path

A key element of any estimator for flux-at-a-point (the air-to-space problem is a flux-at-a-point problem) is the determination of whether the flight path of the neutron from a given point in the problem space to the point of interest (in the case of the air-to-space problem: a satellite in orbit) is unobstructed by dense materials (i.e., the earth itself). If gravity is omitted from the computational method, the flight path is simply a straight line, i.e., the line of sight. Since the geometric construction of this particular problem is relatively simple (earth, atmosphere, vacuum, no other obstructions), this is trivial to implement. With gravity, the computations are much more complicated.

The impact on the problem is both quantitative and qualitative: With gravity, the satellite need not be above the horizon as viewed from the point of emission. Thus, an obstructed line of sight does not necessarily imply an obstructed flight path. Further, the neutron emission direction to achieve a rendezvous with a satellite need not even be remotely in the direction of the satellite. In fact, if emission energy, direction, and time of flight are unconstrained, then a flight path to the satellite is always available between *any*

two points above the earth with the consideration of gravity. This may seem obvious, but the important distinction is that a model neglecting gravity does not find a flight path when the earth obstructs a straight-line path between the source and the detector.

Research Goals

The primary goal of this research is to *identify*, *characterize*, and *quantify* influences of the special features of the air-to-space neutron transport problem to provide information on features that should be included in a Monte Carlo simulation to enhance fidelity for yet-to-be-specified applications. A secondary goal is to *demonstrate* the influence of these special features in the context of a Monte Carlo code. For this purpose, a code that includes these features was written and tested. As a research code for this work, it provides only the capabilities needed for the research.

II. Special Features of the Air-to-Space Problem

To facilitate investigation of the influence of the special features of the air-to-space neutron transport problem, the special features of the problem are described as a list of mechanisms that may quantitatively and qualitatively influence the transport calculation. The mechanisms are grouped into categories: Relative motions, gravity, fidelity of the atmosphere model, and radioactive decay.

Relative Motions

The source, scattering medium, and point at which the flux is to be estimated are not stationary relative to one another, thus violating assumption 8. These relative motions influence several aspects of the air-to-space neutron transport problem:

1. *The Rendezvous Problem*: The detector and emission point move in the ECI frame, changing the procedure by which conditions and properties of a rendezvous between a scattered neutron and a detector are found.

2. *Divergence Factor*: Ratio of intensity at the detector to intensity at emission of a neutron due to divergence on the flight to the detector. Without gravity and with no relative motions, this is the $1/r^2$ divergence that usually applies. However, this factor is influenced by motion of the emission point and motion of the detector (and by gravity).

3. *Optical Thickness Through the Atmosphere*: The earth (including the atmosphere) rotates in the earth-centered inertial (ECI) reference frame. This changes the optical thickness traversed by a neutron in the atmosphere as the atmosphere moves relative to the geometric path during the time of flight.

4. *Motion of the Scattering Medium*: Particles in the scattering medium undergo random thermal motion in addition to bulk motion from rotation of the atmosphere and major wind patterns influencing interaction cross sections, which is usually accommodated by Doppler broadening the cross sections. It also influences the kinematics of each neutron interaction, which is rarely modeled in transport codes but is of interest here.

5. *Motion of the Source*: The source has a velocity in the ECI frame influencing the distribution in direction and energy of emitted neutrons.

Gravity

Gravity causes neutrons to travel on orbital trajectories, violating assumption 2: *Particles travel in straight lines between collisions.* Over the long distances and times of flight involved in the air-to-space neutron transport problem, this may not be negligible. This influences three aspects of the transport problem:

6. *The Rendezvous Problem*: Evaluation of conditions necessary for a neutron to make a flight to the detector and the determination of the parameters describing such a trajectory.

7. *Divergence Factor*: Ratio of intensity at the detector to intensity at emission of a neutron due to divergence on the flight to the detector.

8. *Optical Thickness Through the Atmosphere*: Integration of air density along an orbital trajectory instead of a straight line.

Fidelity of Implementation of the Atmosphere Model

Temperature, density, and composition of the transport medium (the atmosphere) vary continuously with altitude violating assumption 9. The method by which integrals along trajectories through the atmosphere defined by a chosen model are performed influences the results in the air-to-space neutron transport problem. Three considerations are:

9. *Continuous versus Discrete Representation*: Previous implementations divide the problem into regions (such as concentric spherical annuli), in each of which the properties of the transport medium are approximated as uniform. That is to say, a piecewise-constant computational model has been used. This considerably simplifies the transport computation in a single region at the cost of increasing the number of boundary crossing calculations performed during the raytracing procedure. Using a few regions with continuous variation in each makes the layers more difficult to model, but minimizes the cost of raytracing. Here, the layers in the U.S. Standard Atmosphere 1976 are used for this purpose. Thus, discretization of the atmosphere influences the computed optical thicknesses through the atmosphere.

10. *High Altitude Atmosphere*: The atmosphere above some altitude is neglected (changed to vacuum) in the implementation of any atmosphere model. The choice of this altitude influences the computed optical thicknesses through the atmosphere and the spatial distribution of scatters simulated by the Monte Carlo code.

11. *Atmospheric Constituents*: The atmosphere is predominantly composed of Nitrogen-14 and Oxygen-16. Rare constituents (Argon, Nitrogen-15, Oxygen-17, Oxygen-18, etc.) influence the properties of the scattering medium and scatter kinetics. Which constituents to include is another aspect of the fidelity of implementation of an atmosphere model.

Radioactive Decay

Free neutrons are not stable elementary particles. They decay radioactively with a half-life of around ten minutes:

12. *Radioactive Decay of Free Neutrons*: In ordinary nuclear radiation transport applications, neutron lifetimes are on the scale of milliseconds to seconds, so that radioactive decay of neutrons is negligible. (The probability of decay in 100 milliseconds with a 10 minute half-life is approximately 1 in ten thousand.) Radioactive decay is not negligible on the time scale of the air-to space problem. Applying it as a post processing effect introduces errors and increases variance in binned data.

Approach

The approach to the research is to analyze each selected special feature sufficiently that the physics can be modeled in a Fortran code. Then such a code is developed. Both the code and solutions to particular parts of the problem (performed in Mathematica (Wolfram Research, 2017)) is used to investigate

each feature in order to characterize its influence. Each feature will be considered separately and, where additional utility or insight is gained, by combining them.

Fidelity of Optical Thickness Calculations in a Layered Atmosphere

The underlying assumptions made in the development of most production codes preclude their direct use for investigation of the influence of the special features in the air-to-space problem. In particular, the treatment of the atmosphere model is of importance: Discretizing the atmosphere into many layers of constant density introduces overhead to the raytracing process and the integrals necessary to determine optical thickness along a path suffer from systematic errors.

Computational overhead is introduced to the raytracing procedure by the added complication of layers to the problem geometry. The initially trivial geometry of the air-to-space problem consists of two points (source and satellite) and two concentric spheres (earth and atmosphere). Straight-line (no gravity) and orbital trajectories (with gravity) are employed so that the location of a neutron and the geometric description of paths through this geometry is readily determined (with some care to obtain numerically well-conditioned formulae) and efficiently computed. Adding hundreds, thousands, or many more concentric spheres (the constant density layered atmosphere) to the geometry incurs the cost of computing the location of the intersection of each neutron trajectory with each layer boundary. Apart from the obviously large amount of arithmetic

incurred, care must also be taken to avoid systematic accumulation of error and appropriately treat numerically problematic portions of the geometry. This becomes more difficult as more layers are packed into the atmosphere representation.

Issues of overhead and numerical conditioning aside, the layered constant density representation of the atmosphere also impacts the evaluation of the path-length integrals. Performing the integral along a path through layers of constant density effectively implies a composite low-order quadrature with a fixed number of quadrature points per unit change in altitude along the path. If the atmospheric density in a given layer is approximated as the density at the geometric middle of the layer, the implied quadrature rule is the composite midpoint rule.

For vertical paths, it is possible to create a many-layered piecewise-constant-density representation of the atmosphere that provides an adequate approximation (six digits) to path length with approximately 3,500 layers between zero and 86 km altitude, and to some this may be a tractable number. The problem arises with the consideration of horizontal, nearly horizontal, or truly any non-vertical path: The number of layers between zero and 86 km required for a six-digit approximation to path length on a path that includes the point where it is horizontal is close to two million layers with a thickness of about 50 cm each.

Because cross-sections from the Evaluated Nuclear Data File (ENDF) (IAEA, 2017) are tabulated to 4 digits, I chose a precision goal of 6 digits for air integrals. Reducing this to 4 digits would decrease the number of layers from 2 million to 200,000: Even this would dominate the cost of an entire Monte Carlo simulation.

Source-Detector Orientations

The influences of the special features of the air-to-space problem are best illustrated in certain orientations of the source and detector at the instant of neutron emission. The location of a geostationary satellite in its orbit, with respect to a point fixed in ECI coordinates on or above the earth specified by the difference in right ascension, $\Delta\alpha$, between the two. When $\Delta\alpha = 0$, the satellite is above the equator due north or south of the fixed point and both are on the same side of the earth. As the satellite moves east along its orbit, $\Delta\alpha$ increases. Figure 2 shows various values of $\Delta\alpha$ that were selected to illustrate the influences of the special features explored in this document. A value of $\Delta\alpha$, along with a source latitude, fully defines the orientation of the source and detector (as long as the detector is restricted to a circular equatorial orbit, as it is in this research) at the instant of neutron emission.
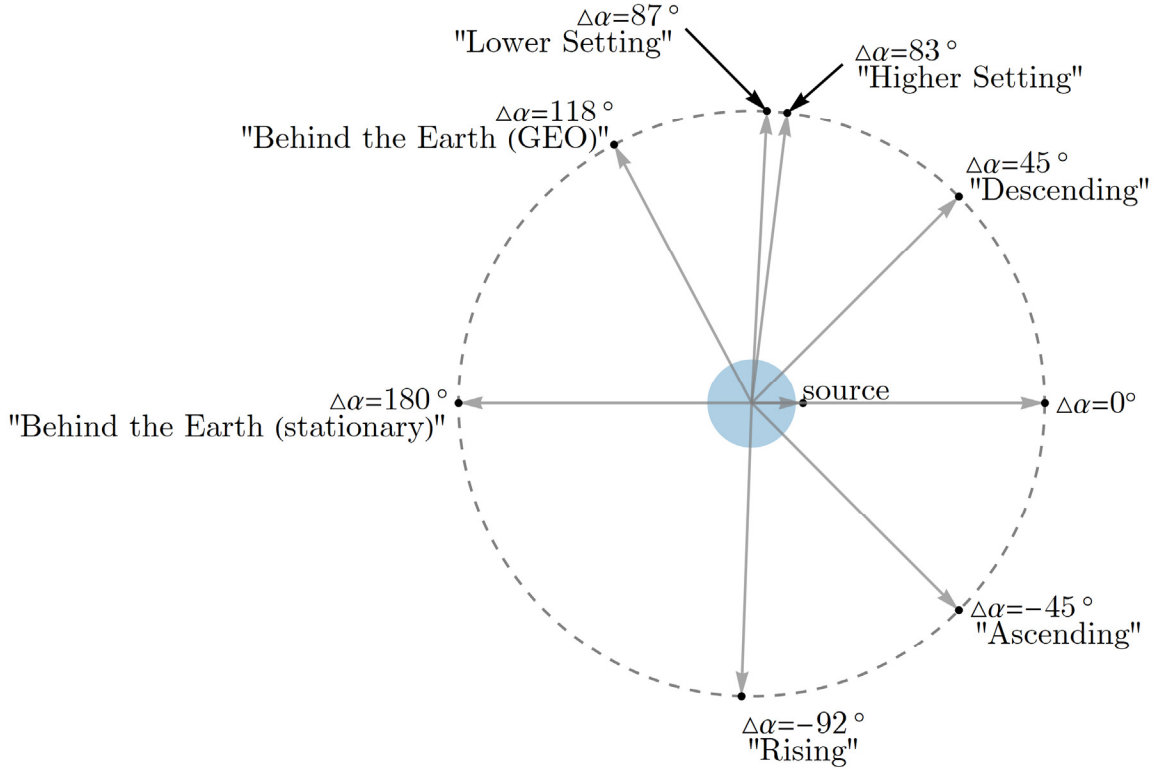
Figure 2: Source-detector orientations for example problems:
Problem names and their difference in right ascension, $\Delta\alpha$,
at the moment of neutron emission.

The locations of the source and detector at the instant of emission shown in Figure 2 were selected for their convenience, importance, or to illustrate interesting features of the problem and research findings. Beginning with $\Delta\alpha = 0$, the satellite is above the equator due north or south of the source point (fixed in ECI) and both are on the same side of the earth. This orientation ($\Delta\alpha = 0$), at the time of emission, represents the point of closest approach between the source and detector.

Next, $\Delta\alpha = -45°$ and $\Delta\alpha = +45°$ are referred to as the *ascending* and *descending* geometries. The *ascending* geometry ($\Delta\alpha = -45°$) positions the

detector such that it is in view of the source to the west from the point of view of the source at the instant of emission. In the ECI frame, this detector then ascends in the sky (hence the term *ascending*) as viewed from the ECI location of the source during the time scale of the problem. At the instant of neutron emission in a transport calculation beginning in the *ascending* geometry, the range between the source and detector is closing and direct trajectories (with and without gravity) to the detector arrive with a velocity component opposite that of the direction of detector motion. The *descending* geometry ($\Delta\alpha = +45°$) positions the detector such that it is in view of the source to the east from the point of view of the source at the instant of emission. In the ECI frame, this detector then descends in the sky (hence the term *descending*) as viewed from the ECI-fixed location of the source during the time scale of the problem. At the instant of neutron emission in a transport calculation beginning in the *descending* geometry, the range between the source and detector is opening and direct trajectories (with and without gravity) to the detector arrive with a velocity component in the same direction as the motion of the detector.

Geometries were also selected to demonstrate cases where the line of sight and flight path may change from unobstructed to obstructed (and vice versa) during the time scale of the simulation. First, $\Delta\alpha = -92°$ is referred to as the *rising* case. At the instant of neutron emission, the detector is not visible from the point of view of the source, but during the time scale of the problem, the detector may rise (in the ECI frame) into view of the ECI source location. Next,

$\Delta\alpha = 83°$ and $\Delta\alpha = 87°$ represent the *high setting* and *low setting* orientations respectively. In both the *high* and *low setting* cases, the detector is in view from the point of view of the source at the time of emission, but then sets out of view (in the ECI frame) during the time scale of the problem. The *high setting* case is the general case to demonstrate the change in obstruction state of the line of sight and flight path, and the *low setting* case demonstrates a feature of the transport seen only with consideration of gravity: the loss and subsequent reacquisition of an unobstructed flight path to the detector during the range of times of flight for neutrons reaching the detector.

The final orientations, $\Delta\alpha = 118°$ and $\Delta\alpha = 180°$, are collectively referred to as *behind the earth.* These orientations are used demonstrate another feature of the transport problem only seen with the inclusion of gravity: The availability of flight paths to a detector on the opposite side of the earth from the source.

The HATS-n Code

Achieving good precision in the path-length integrals at an acceptable cost necessitates the development of a specialized code that treats the atmosphere continuously within each of a few layers for the air-to-space class of problems. A research code, High-Altitude Transport to Space for Neutrons (HATS-n), was developed as part of this research effort as a tool for demonstrating the effects of the special features influencing the transport problem. Code development required organizing the simulation into modules that incorporated the physics for

each feature and required developing well-conditioned formulas for each one. This was the major time investment in the research. Nevertheless, the code, while of value as a starting point for future production codes for this application, is not intended to include all the features that a production code would require.

Initially, HATS-n was a branch of the High-Altitude Space Transport Estimator for Neutrons (HASTEN) code project which is a research platform for various flux-at-a-point estimators in the context of the air-to-space transport problem (Mathews, 2013-2017). The creation of the HATS-n branch implemented changes in three areas: First, removal of advanced and experimental estimators leaving only the original next-event flux-at-a-point estimator described in (Kalos, 1963). Second, addition of modules and routines to account for the special features of the problem that are the subject of this research. And finally, revision of code implementation to target execution on massively parallel architectures (specifically the Intel® Xeon Phi™ x100 series Many-Integrated-Core coprocessor family). The addition of special features to the code and targeting for massively parallel architecture constitute major revisions to the original HASTEN code: As of this writing, HATS-n has less than 20% code in common with the original HASTEN project. An overview of the HATS-n code is given in *Appendix A. Overview of the HATS-n Code.*

Output from HATS-n is in the form of formatted text files containing the bin-by-bin listings of the intercepted neutron current density, J, per bin per unit detector area per source neutron $[(n_d \, / \, \text{bin}) \, / \, (\text{km}^2 \cdot n_s)]$, as well as variance

estimates (in the form of standard error, σ_{std}). Bin-by-bin estimates and standard errors are listed for time-energy bins, time bins (integrated in energy), energy bins (integrated in time), nadir cosine -azimuth bins, nadir cosine bins (integrated in azimuth), azimuth bins (integrated in nadir cosine), and total intercepted neutron current density seen by the detector. Example plots of time-energy data from three HATS-n runs are shown in Figure 3. The two plots at the top of Figure 3 show the bin-by-bin current density estimates integrated in energy and time, respectively. Total scattered current density estimates are plotted using the darker hue while the first-flight current density is plotted using the lighter hue. When only a single HATS-n estimate is plotted, as in Figure 4, the relative standard error, σ_{std} / J where J is the intercepted neutron current density for which σ_{std} was computed, is plotted in gray with its scale on the right side of each plot in which it appears.

The lower left plot in Figure 3 shows the position in time and energy of arriving current density contributions as seen by the detector. The lower right plot shows the segment of a geostationary orbit over which the current density contributions (from the total estimate, direct and scattered) are spread. Neither the magnitude of intercepted neutron current density in any time-energy bin nor their variance are shown in the lower two (time-energy position and orbit segment) plots. The source point is shown by the small black dot on the gray arrow at the edge of the earth and the longer gray arrow points to the location of the detector at the instant of neutron emission. In this example, the satellite is at

$\Delta\alpha = 0°$ relative to the source point at the instant the neutrons are emitted. Although the plot is two dimensional, it is, in effect, a cross-section of the earth cut through the equatorial plane and seen from above the north pole. Thus, the satellite moves eastward (counterclockwise). Neutrons arrive from within a few tenths of a second up to some hours later, arriving at points along the orbit further east for later arrivals.
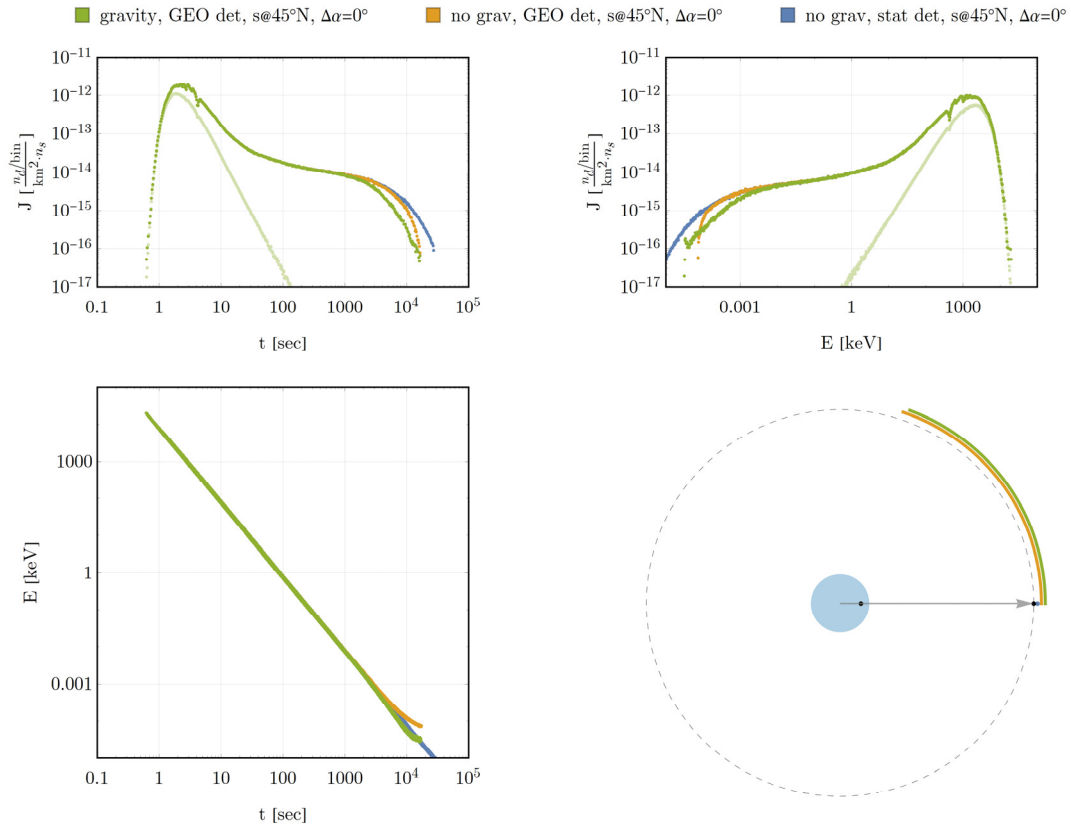
Figure 3: Example HATS-n time-energy plots of intercepted neutron current density from a Watt-fission-235 source at 50 km and 45°N to stationary and geostationary detectors without gravity and geostationary detector with gravity.

21
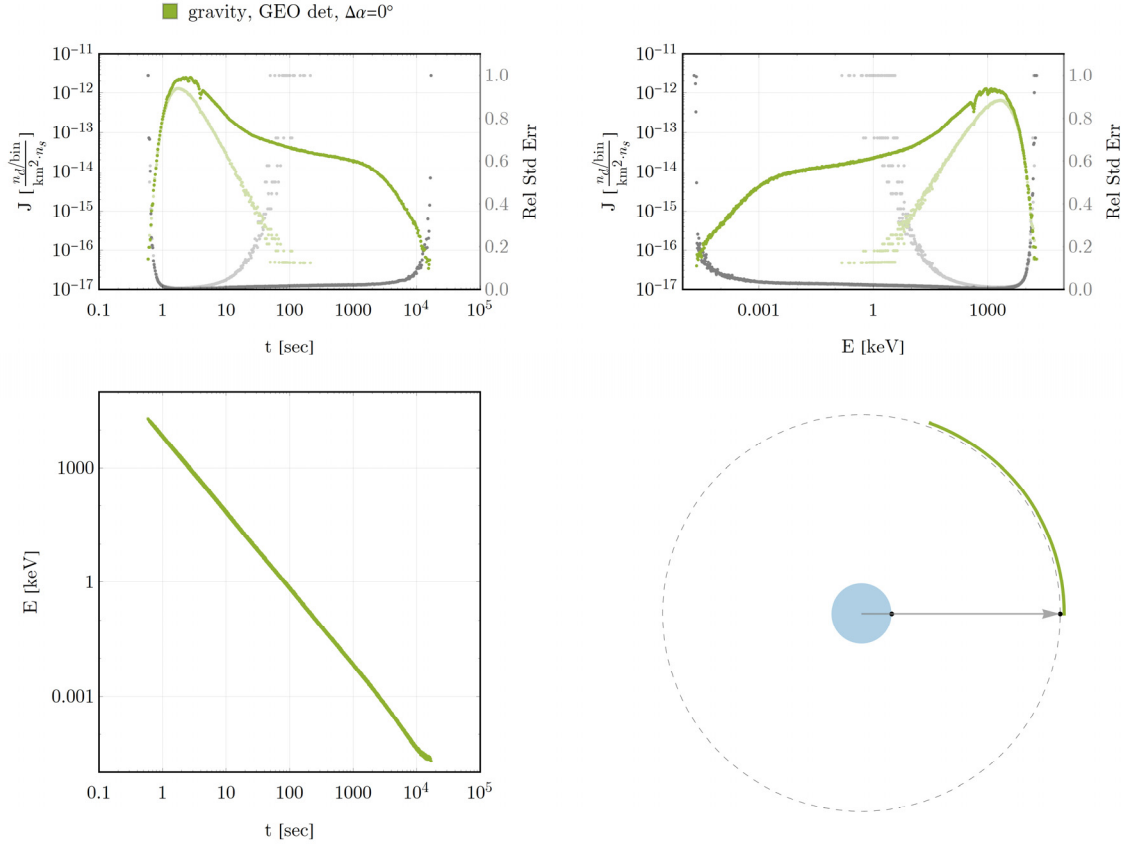
Figure 4: Example HATS-n time-energy plots of intercepted neutron current density from an equatorial Watt-fission-235 source at 50 km stationary and geostationary detectors without gravity and geostationary detector with gravity

Example plots of the nadir-azimuth data from a HATS-n run are shown in Figure 5. The two plots at the top of Figure 5 show the bin-by-bin neutron current density estimates integrated in azimuth and nadir cosine with first-flight intercepted neutron current density and relative standard error plotted as before. The polar plot shows the nadir and azimuth of arriving contributions as seen by the detector. The plot is oriented such that the displayed radial axis (black horizontal axis) points in the forward direction (direction of detector motion) and zero degrees on the radial axis (the center of the figure) points downward toward

the center of the earth. The magnitude of intercepted neutron current density in any nadir-azimuth bin and variance are not shown in this plot. The blue ring (crossing the radial axis near 10 degrees) on the nadir-azimuth plot approximates the field of view which the earth occupies as seen from geostationary altitude.
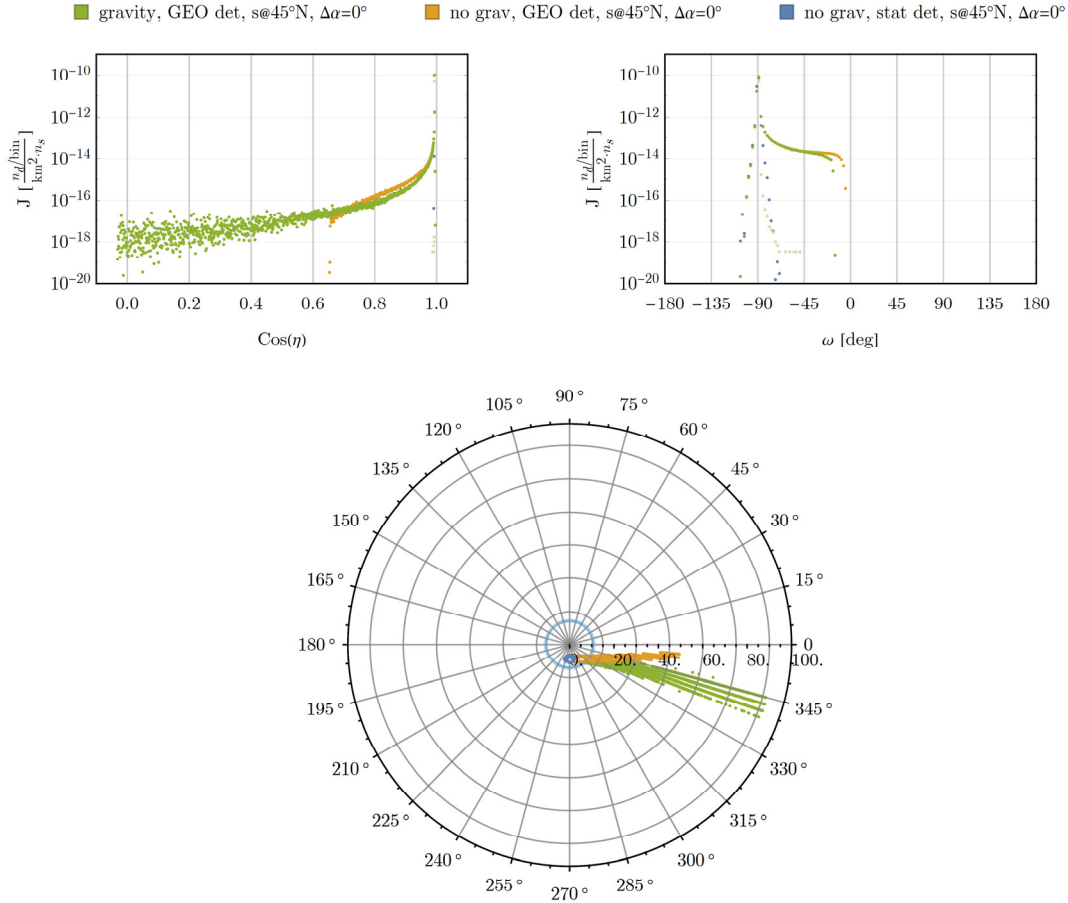
Figure 5: Example HATS-n nadir-azimuth plots of intercepted neutron current density from a Watt-fission-235 source at 50 km and 45°N to overhead stationary and geostationary detectors without gravity and geostationary detector with gravity.

Continuua of First-Flight Problems

When viewing the output from HATS-n, the direct influence of any feature of the transport model on the transport calculations is obscured or merged with the other features of the transport problem. This is by design, and is the great strength of Monte Carlo methods for solving complex physical problems, but the side-effect is that the intermediate states at any point during the simulation are not saved. These intermediate states are where the mechanisms of influence act directly on the transport calculation. In particular, the parameters associated with any given neutron flight to the satellite are of interest for this research. Instead of attempting to unfold the result of a HATS-n run to isolate special features of the problem, some features may be investigated by restricting consideration to the set of first-flight trajectories that join an emission point with a detector absent other aspects of the transport problem. For these first-flight problems, a neutron emerges from a stationary point and makes a direct flight to the detector. The emergence point may be the neutron source or a collision in the atmosphere. The first-flight problem is then solved for a continuum of emission energies over which properties of the neutron flight can be compared. The comparison may be plotted with either emission energy or time of flight to intercept as the dependent variable: Emission energy as the dependent variable is useful for observing variation at high energies and low times of flight, and time of flight as the dependent variable is useful for observing variation at low energies and longer times of flight.

In comparing two quantities, a norm of relative difference is needed. I chose to use the symmetric relative difference (SRD). The SRD has exchange symmetry: $\left\| x, y \right\|_{srd} = \left\| y, x \right\|_{srd}$, unlike the usual relative differences $\left| x - y \right| / y$ and $\left| x - y \right| / x$. The SRD between two quantities x and y is

$$\left\| x, y \right\|_{srd} = \begin{cases} 0 & x = y = 0 \\[2mm] \dfrac{\left| x - y \right|}{\left(\dfrac{\left| x \right| + \left| y \right|}{2} \right)} & \text{otherwise} . \end{cases} \tag{1}$$

The SRD approaches the relative error, $\left| x - y \right| / x$, for small $\left| x - y \right|$. Unlike the relative error, with which 2 is 100% larger than 1, but 1 is 50% less than 2, which is misleading, the SRD has exchange symmetry: The SRD of 2 and 1 as the same as the SRD of 1 and 2. Furthermore, the SRD is bounded and continuous for all y if $x \neq 0$. As $\left| x - y \right| \to \infty$, the SRD approaches 2. If x and y have opposite signs, or one is zero and the other is not, the SRD is 2.

An example of the arrival energy as a function of time of flight from an emission point at 50 km altitude and 45°N after flight to a geostationary detector with $\Delta \alpha = 0$ at the time of emission, with and without the influence of gravity, is shown in Figure 6. The plot at left shows the comparison with the SRD plotted in gray with its scale on the right. The right portion of the figure shows the orientation of the emission point and satellite at time of emission, with the segment of the satellite orbit covered by the range of emission energies highlighted in the appropriate color. These follow the dashed black ellipse which

is the orbital path of the satellite. The neutron trajectories that intercept the satellite at the earliest and latest times are also shown in this view. They join the emission point to the ends of the orbit segments. A plan view of the satellite orbit, as seen from the north side of the orbit, is shown as the light gray circle. The orbit segments are also drawn on the plan view.
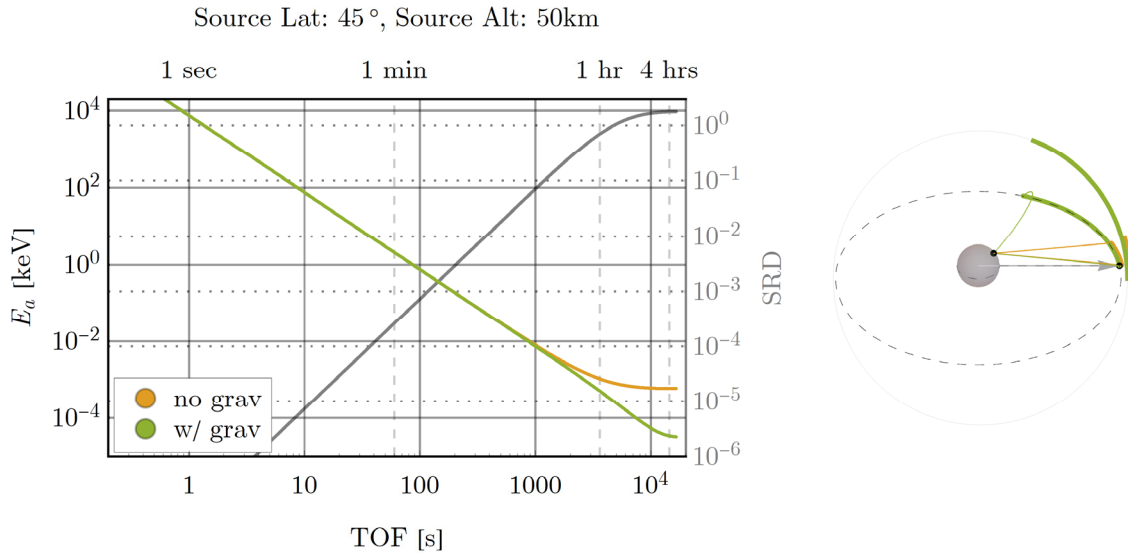
Figure 6: **Example first-flight comparison of arrival energy as a function of time of flight from an emission point at 50 km altitude and 45°N after flight to a geostationary detector with $\Delta\alpha = 0$ at the time of emission, with and without the influence of gravity.**

Scope, Assumptions, and Limitations

In general, the scope of the research is limited to identifying, characterizing, and quantifying the influence of the major special features of the air-to space neutron transport problem. To facilitate concise and effective discussion of these special features, detailed description of the specific algorithms and the practical

26

aspects of their development is excluded from this document. The algorithms as presented here are part of the general description of the process by which the features of interest were investigated.

It should be noted that the research question here is, fundamentally: Are the effects of gravity, relative motion, atmospheric modeling, and radioactive decay significant enough to be included in Monte Carlo calculations for the air-to-space neutron transport problems. To answer this question, simplified models are sufficient. Presuming the answer to be *yes*, the fidelity of modeling (such as what perturbations to include, i.e., winds, an asymmetric gravitational field, third-body gravity) needed for any particular application is application-dependent and a subject for future work.

Frames of Reference

Several reference frames are required throughout the consideration of the problem including earth-centered inertial, earth-centered earth-fixed, reference frame of the air, center-of-mass of each scattering collision, and reference (rest) frames for the source and satellite or detector. The earth-Centered Inertial (ECI) frame has its origin at the geometric center of the earth with one axis pointing to true north, the next to the First Point of Ares, and the third completing a right-handed system. The ECI frame does not rotate with the earth. Motion of the elements in the system are referenced to the ECI frame unless otherwise noted. The Earth-Centered Earth-Fixed (ECEF) frame also has its origin at the

geometric center of the earth and one axis pointing towards true north, but

unlike the ECI frame, the second axis points towards the prime meridian with

the third axis completing a right-handed system. The ECEF frame rotates with

the rotation of the earth and is denoted with the superscript $ecef$. The reference

frame of the air, used when considering thermal and other motion of the air and

rotation of the atmosphere with the earth, is described using East-North-Up

(ENU). Quantities in the reference frame of the air are indicated with the

superscript af. The center of mass of the collision (CM) frame is used for

describing and computing the scattering behavior of neutrons in the medium.

Basis vectors $\hat{A}\hat{B}\hat{C}$ in the CM frame are referenced to either the incident or

scattered direction depending on the application. Quantities expressed in the CM

frame are denoted with the superscript cm. The directional and energy

distributions of neutron emitted by the source are specified in the rest frame of

the source. This frame is indicated with the superscript sf. The emergence frame

refers to either the CM frame or the source frame as appropriate and is used

when the formulations or procedures may be applied to neutrons emerging from

the source or emerging from a collision. Quantities in the emergence frame are

denoted with the superscript ef. The reference frame of the satellite is described

using the down, orbit normal, forward $\left(\widehat{D}\,\widehat{ON}\,\widehat{F}\right)$ set of basis vectors. The down

vector $\hat{D}$ points from the center of mass of the satellite to the geometric center of

the earth; the orbit normal vector $\widehat{ON}$ points in the direction normal to the

plane containing the orbit of the satellite; and the forward vector $\hat{F}$ completing

this right-handed system: $\hat{F} = \hat{D} \times \widehat{ON}$. (For a circular orbit, such as the geostationary orbit used here, $\hat{F}$ points in the direction of the satellite velocity vector.)

Elements and Geometry of the Air-to-Space Problem

Source

The source is approximated as a point in space and time fixed in the ECI frame and at time equals zero. Neutrons are emitted from the source at the instant of time equals zero. Source motion is captured as an instantaneous velocity at the time of neutron emission. The emission spectrum of neutrons (in the rest frame of the source) for all the results presented in this research is a Watt spectrum approximating the probability density function (pdf) of neutron energies from fission of Uranium-235 (Knief, 2008, p. 45):

$$\chi_{U^{235}}(E_n) = \left(0.452463 \times 10^{-3}\right) e^{-0.001036 E_n} \operatorname{Sinh}\left(0.0478539\sqrt{E_n}\right) \qquad (2)$$

where the neutron energy E_n has units kiloelectronvolts (keV). The cumulative distribution function (CDF) is

$$F_\chi(E_n) =$$
$$\left(\frac{\operatorname{erf}\left(0.743375 + 0.032187\sqrt{E_n}\right) - \operatorname{erf}\left(0.743375 - 0.032187\sqrt{E_n}\right)}{2}\right) \qquad (3)$$
$$- 0.43674 e^{-0.001036 E_n} \operatorname{Sinh}\left(0.0478539\sqrt{E_n}\right).$$

The probability and cumulative density functions for this distribution are plotted in Figure 7.
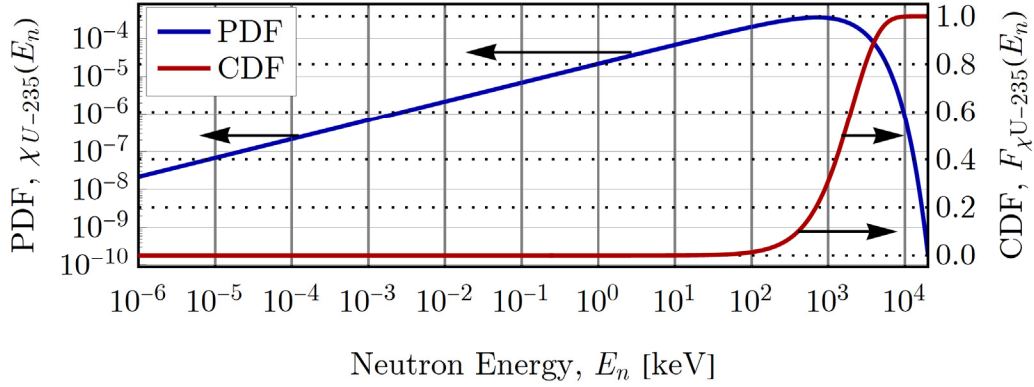
Figure 7: **Probability density and cumulative distribution functions approximating the distribution of neutron energies from fission of Uranium-235.**

Detector

The detector is approximated as a point that may or may not move during the problem. Where necessary, the geometry of the detector is further assumed to be spherical with geometric cross-sectional area of unity. Detector efficiency is not considered (implying a *perfect* detector), but could be added to the calculations if a specific detector response function were to become of interest.

Earth and Atmosphere

The earth is approximated as a spherical perfect absorber with radius $R_{\oplus}$ surrounded by an atmosphere from the surface of the earth to the top of the atmosphere: $R_{\oplus}$ to $R_{\oplus} + Z_{top}^{atm}$. Altitudes above Z_{top}^{atm} are in vacuum. In order to

30

reduce computational run times, a minimum altitude for the atmosphere may also be specified as Z_{bot}^{atm} below which the atmosphere is considered a perfect absorber. The results reported here used Z_{bot}^{atm} equal to 0 km. The atmosphere may be composed of layers in which the properties of the atmosphere are computed by different methods or formulae (for example, the U.S. Standard Atmosphere 1976 has seven layers from the surface of the earth up to 86 km). Each layer is numbered with index b beginning with $b = 1$ for the layer closest to the surface of the earth and increasing with altitude. The altitudes at the bottom and top of a layer are Z_{b-1} and Z_b respectively.

The methods developed here apply to any planet with an atmosphere and an orbiting detector. The earth is the example of interest, and is used in all the examples. However, in this document, the word *earth* is not capitalized because it could be replaced by *planet* or *the example planet.*

Relative Motions

For relative motions, the atmosphere is modeled as though the air is geostationary, i.e., the earth and the atmosphere are modeled as having rigid-body rotation. Thus, the air moves only longitudinally (east to west). Thermal motion of atoms and molecules of the air is determined by the temperature of the medium as specified in the selected atmosphere model. Localized atmospheric motion, e.g. wind and weather, is not considered, although well characterized large wind patterns such as the Jet Stream are mentioned for scale.

The detector is modeled either as stationary in the ECI frame (moving in a straight line in the emergence frame) or as geostationary (a particular circular orbit in the ECI frame, or stationary in the ECEF frame). It is sufficient for this study to model the source as emitting from a point in space at an instant in time. (Because the solution for such a point source is the Green's function for a source distributed in space and time, nothing is to be gained here by treating a distributed source.) Therefore, the velocity of the source at that instant must be included in the model here, but the trajectory of the source at other times is irrelevant.

Gravity

Neutron motion is either straight at constant speed (without gravity) or along two-body orbital trajectories, i.e., along general or degenerate hyperbolas, parabolas, or ellipses, depending on neutron total energy (with gravity).

Perturbations of the gravitational field due the earth (caused by gravitational attractions of other bodies and the deviation of the earth from a radially-symmetric sphere) are small. However, they accumulate over many revolutions of earth satellites, resulting in slow drifts of their orbital elements. Because neutrons survive only a matter of hours, the effects of these perturbations are quite small, and not included in orbit determination calculations performed in this research.

Atmosphere Model

The U.S. Standard Atmosphere 1976 (NOAA, NASA, USAF, 1976) is the atmosphere model selected for this research. Relevant constants and equations are summarized in *Appendix B. Summary of U.S. Standard Atmosphere 1976.* Higher fidelity and more modern empirical models are available that include much more detail (atmospheric weather, space weather, etc.), but at a higher cost in complexity and computation time. The U.S. Standard Atmosphere 1976, herafter referred to as USSA-76, provides a continuous temperature and density approximation of sufficient complexity to demonstrate the influence of the model and for meeting the research goals. To further preserve generality, it is worth noting that the construction of the USSA-76 model can be adapted and applied to account for other empirical atmospheric data with little effort and changes to the calculations performed here. It is simply a matter of finding a piecewise-linear fit to the temperature profile of the atmosphere to be modeled and applying the corresponding formulae from the USSA-76 model appropriately.

Radioactive Decay

Radioactive decay of free neutrons follows the exponential law of radioactive decay. The mean lifetime for free neutrons is listed in Table 2.

Physical Constants and Units

Relevant units of measure, physical constants and values, and constants for unit conversion are listed in Table 1, Table 2, and Table 3 respectively. Unless otherwise stated, quantities are expressed in units listed in Table 1. Note that the mean lifetime for neutrons, τ_n in Table 2, is not known with great certainty: Values in the literature range from 878 (Serebrov, et al., 2008) seconds to 886 seconds (Yue, et al., 2013). The value used here is the mean of the lifetime from these two references.

Table 1: Units of Measure

Quantity	Unit	
Distance	kilometer	(km)
Time	second	(s)
Energy	kiloelectronvolt	(keV)
Microscopic Cross Section	barn	(b)
Macroscopic Cross Section	1 / kilometer	(km^{-1})

Table 2: Physical Constants

Constant	Symbol	Value
Neutron Mass	m_n	$1.674927471 \times 10^{-27}$ kg
Boltzmann Constant	k	$1.38064852 \times 10^{-23}$ J/K
Mean Lifetime of Free Neutrons (due to radioactive decay)	τ_n	882 s
Mean Radius of the Earth	$R_\oplus$	6371 km
Angular Rotation of the Earth	$\omega_\oplus$	7.292115×10^{-5} rad/s
Standard Gravitational Parameter of Earth	μ	398600.4418 km^3/s^2

Table 3: Constants for Unit Conversions

Conversion Constant	Value
$K_{\mathrm{km/m}}$	10^{-3} km/m
$K_{\mathrm{keV/J}}$	$6.241509126 \times 10^{15}$ keV/J

III. The Rendezvous Problem

To use a next-event estimator, it is necessary to determine the trajectory that will result in a neutron emerging from either the source or a scattering collision subsequently arriving at the detector without colliding along the way. This is the rendezvous problem.

The Challenge

In a code that implicitly puts the source, the scattering medium, and the detector at rest (i.e., in the lab frame), and that moves neutrons in straight lines, this problem is trivial: Set the direction of motion to $\hat{\Omega} = \left(\vec{r}_2 - \vec{r}_1 \right) / \left| \vec{r}_2 - \vec{r}_1 \right|$. The rendezvous then occurs for any neutron speed, and the speed is computed from the direction. (The problem doesn't deserve a name in such codes.)

However, with relative motions and curved neutron paths, the problem is not at all trivial. The rendezvous solution requires a nonlinear search algorithm that accounts for several factors:

1. *The speed of an emitted neutron is independent of its direction in the rest frame of the emission point*: The speed of a scattered neutron is independent of its direction in the CM frame of the collision. Therefore, its speed in the ECI frame and the direction in the ECI frame are coupled variables.

2. *The detector follows an orbital trajectory*: Given the initial location and the parameters of the satellite orbit, finding the location of the

detector after a given time of flight constitutes the orbit propagation, or Kepler's, problem. Algorithms for solving Kepler's problem are available, but the speeds of high-energy neutrons are so much greater than those encountered in astrodynamics applications that some reformulation of the equations is required to ensure acceptable numerical conditioning. There is, in general, computational cost to consider because solutions to Kepler's problem are generally found iteratively.

3. *The neutron follows an orbital trajectory*: Given the initial and final locations and a time of flight, finding the parameters of an orbit joining the two points constitutes the targeting, or Lambert's, problem. Efficient algorithms are available for the Lambert problem, but as with solutions to the Kepler problem numerical conditioning and computational cost must be considered.

4. *The starting location of the neutron (at the source or scatter) and the time of this event are known*: If the time of rendezvous were known, a single solution to Kepler's problem would find the location of the satellite at the rendezvous time. Then the solution to a Lambert problem would find the velocity (in the ECI frame) with which the neutron must leave the starting point to follow the trajectory that would rendezvous with the detector at that location after that time of flight.

5. *The starting speed (in the ECI frame) is unknown*: The starting speed in the ECI frame depends on the starting direction of motion in the ECI frame. If the starting speed were known, it would specify both the starting direction of motion and the kinetic energy of the neutron.

6. *The starting direction of motion (in the ECI frame) is unknown*: The starting direction of motion in the ECI frame depends on the starting speed in the ECI frame. If the starting direction of motion were known, it would specify the starting speed (hence kinetic energy) of the neutron in the ECI frame.

The challenge is to find an efficient and accurate way to find the time of flight, the starting direction, and the starting speed (hence kinetic energy) that are mutually consistent with achieving a neutron rendezvous with the detector.

The required and available emission speeds for a sample rendezvous problem are shown in Figure 8**Error! Reference source not found.**. The required speed is the magnitude of the velocity vector required to achieve rendezvous. The available speed is the speed of the neutron after the scatter in the direction required for rendezvous. The shape of the required speed curve is predictable: Monotonically decreasing from infinity at $\Delta t = 0$ through escape speed at the parabolic flight time, $\Delta t = \Delta t_{parabolic}$, to a global minimum at the minimum velocity transfer, $\Delta t = \Delta t_{minV}$, and then monotonically increasing back to escape speed at $tof = \infty$. The shape of the available speed curve depends on the direction to each rendezvous represented on the required speed curve.

The points at which the required and available speed curves cross are solutions to the rendezvous problem. In this example, Figure 8, there are two roots: One early-time rendezvous where the neutron is on the outbound portion of its trajectory, and one late time rendezvous where the neutron is on the return portion of its trajectory. Given the flight times involved to reach geosynchronous detectors (up to 5 hours), and the high probability of radioactive decay of a neutron on flights longer than this, the algorithm presented below only seeks possible rendezvous on outbound trajectories. Should detectors in closer proximity to the emergence point be considered (i.e. detectors in low- or middle-

earth orbits), or if rendezvous on return trajectories becomes of interest, the algorithm would need to be modified to seek these additional roots.
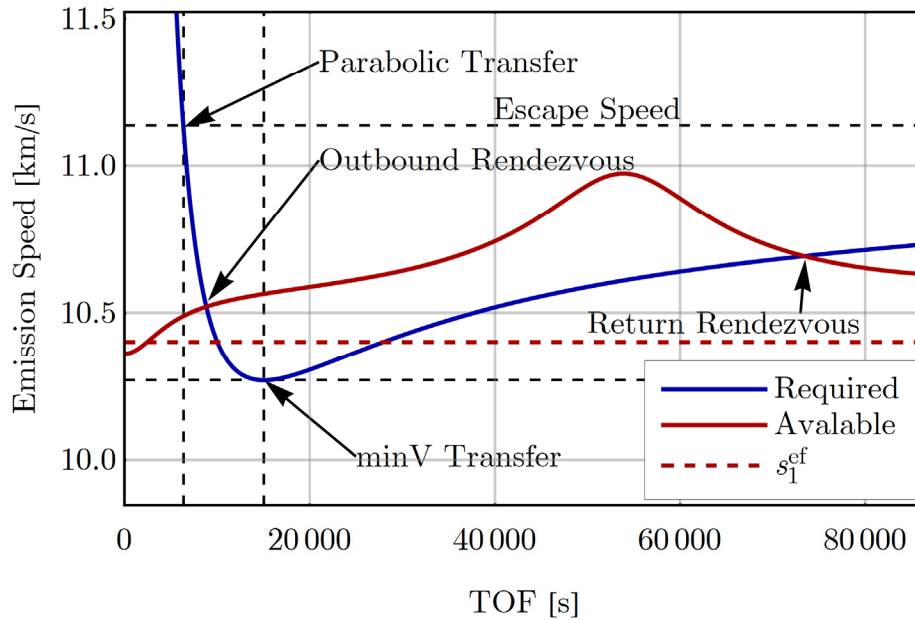
Figure 8: Required and available speed for an example rendezvous problem.

Algorithm for Solving the Rendezvous Problem

An algorithm for the rendezvous problem requires an iterative process that starts with an estimate of one of the coupled variables (time of flight, starting direction, and starting energy or speed), computes the other two yielding a difference between one of the variables as obtained two different ways, and adjusts the estimated variable until this difference is sufficiently small.

Note: If the influence of gravity on the neutron is neglected, the Lambert problem reduces to a trivial trigonometry problem, but the rendezvous problem

still requires this iterative search. Additionally, the check for a clear flight path simplifies to a check for line of sight. With these exceptions, the algorithm is the same in each case.

The algorithm I use is:

Find Neutron Rendezvous

In($\vec{r}_1$, s_1^{ef} , $\vec{r}_{sat}$, $\vec{v}_{sat}$ **) Out(** Δt **)**

1. Establish a lower bound on time of flight: Δt_{min} .

   IF the required speed to achieve rendezvous in the emergence
       frame for this time of flight, $s_1^{ef}(\Delta t_{min})$, exceeds the
       actual speed available in the emergence frame, s_1^{ef} , then
       there is not enough kinetic energy available for the
       neutron to achieve a rendezvous,

       RETURN a NO SOLUTION flag.

   END IF (a solution is possible at a lower speed and a longer
       time of flight)

2. Establish an upper bound on time of flight: Δt_{max} .

   IF the required speed to achieve rendezvous in the emergence
       frame for this time of flight, $s_1^{ef}(\Delta t_{max})$, is less than the
       actual speed available in the emergence frame, s_1^{ef} , then
       there is too much enough kinetic energy available for the
       neutron to achieve a rendezvous,

       RETURN a NO SOLUTION flag.

END IF (a solution is possible at a higher speed and a shorter

    time of flight)

3. Choose a starting value for time of flight $\Delta t_{n=0}$ in the search

   interval $\left(\Delta t_{min}, \Delta t_{max}\right)$.

4. DO

        Find $s_1^{ef}(\Delta t_n)$ and compare it to the actual speed s_1^{ef}.

        Compare Δt_n to Δt_{n-1}.

        IF both speed and time of flight agree within a

           tolerance, a rendezvous has been found,

             EXIT the loop.

        ELSE IF the required speed is the greater,

             SET $\Delta t_{min} = \Delta t_n$.

        ELSE

             SET $\Delta t_{max} = \Delta t_n$.

        END IF

        Choose a new time of flight, Δt_{n+1} between the new,

           tighter bounds $\left(\Delta t_{min}, \Delta t_{max}\right)$.

   END DO

5. Check for a clear flight path to the detector.

   IF, in the ECI frame, $\vec{r}_1 \cdot \vec{v}_1 < 0$ (neutron starts downward) and

      $\vec{r}_2 \cdot \vec{v}_2 > 0$ (neutron meets detector moving upward), then the

flight path of the neutron to the rendezvous may be

obstructed by the earth.

Calculate the radius at perigee, r_p, for the trajectory.

IF r_p is less than the radius of the earth, $R_\oplus$,

RETURN a NO SOLUTION flag.

ELSE (the path is clear)

RETURN the solution.

END IF

ELSE (the path is clear)

RETURN the solution.

END IF

6. From the solution to the rendezvous problem, compute the

properties of the rendezvous.

Details of the Rendezvous Calculations

With the consideration of gravity, a neutron now follows an orbital

trajectory on its flight to rendezvous with a detector also in orbit. The same

procedure as presented for finding the path to intercept a moving target applies

here, with small changes to account for gravity.

Kepler's Problem

Determining the location of an orbiting body at a particular time is referred to as the orbit prediction problem or Kepler's problem. The problem is stated as: Given position $\vec{r}_0$ and velocity $\vec{v}_0$ at time t_0, find position $\vec{r}$ and velocity $\vec{v}$ at time $t_0 + \Delta t$. Techniques for solutions are common in the literature. An algorithm developed by Gooding (Gooding & Odell, 1988) is robust, computationally efficient, and well documented. The FORTRAN77 routines from Gooding (Gooding & Odell, 1988) were revised for implementation in modern Fortran with additional minor changes for this specific application. Most of these changes were made to improve numerical conditioning for the high velocities of energetic neutrons. (Such high velocities are not achievable by space vehicles and thus were not of concern to Gooding and Odell.) A compact notation to denote a solution to Kepler's problem will be useful. The notation used here is

$$(\vec{r}, \vec{v}) = \mathcal{K}(\vec{r}_0, \vec{v}_0, \Delta t), \tag{4}$$

or separately as the *Kepler position* and *Kepler velocity*

$$\begin{aligned}
\vec{r} &= \mathcal{K}_{\vec{r}}(\vec{r}_0, \vec{v}_0, \Delta t) \\
\vec{v} &= \mathcal{K}_{\vec{v}}(\vec{r}_0, \vec{v}_0, \Delta t).
\end{aligned} \tag{5}$$

Lambert's Problem

Determining an orbital trajectory that connects two positions given a time of flight is referred to as the targeting problem or Lambert's problem. The

problem is stated as: Given positions, $\vec{r}_1$ and $\vec{r}_2$, and time of flight Δt, determine the orbit that joins the two points (find velocities $\vec{v}_1$ and $\vec{v}_2$). Techniques for solutions are common in the literature. An algorithm developed by Gooding (1988) (1990) expands on the work of Lancaster (1969) and is robust, computationally efficient, and well documented. The FORTRAN77 routines from Gooding (1990, pp. 160-164) were revised for implementation in modern Fortran with additional minor changes for this specific application (mainly; multi-revolution trajectories need not be considered as solutions for this specific application).

A compact notation for the solution to Lambert's problem will be useful

$$(\vec{v}_1, \vec{v}_2) = \mathcal{L}(\vec{r}_1, \vec{r}_2, \Delta t), \tag{6}$$

or separately for each *Lambert velocity*

$$\begin{aligned} \vec{v}_1 &= \mathcal{L}_1(\vec{r}_1, \vec{r}_2, \Delta t) \\ \vec{v}_2 &= \mathcal{L}_2(\vec{r}_1, \vec{r}_2, \Delta t). \end{aligned} \tag{7}$$

Minimum Time of Flight

Assuming the detector is at a higher altitude than the emission point, the minimum possible time of flight may be bounded by accounting for the maximum possible closing speed between the detector and the emitted neutron:

$$\Delta t_{min} = \frac{\left| \vec{r}_2 - \vec{r}_1 \right|}{s_1^{ef} + \left| \vec{u}_{ef} \right| + \left| \vec{v}_d^{max} \right|}. \tag{8}$$

44

As with any object on and orbital trajectory, the maximum detector velocity is the velocity at perigee. The radius and velocity at perigee, r_p and v_p, are

$$r_p = \frac{p}{1+e} \tag{9}$$

and

$$v_p = \sqrt{2\left(\xi + \frac{\mu}{r_p}\right)} \tag{10}$$

where the orbit's semi-parameter (or semi-latus rectum) p, specific (total, i.e., kinetic and potential) mechanical energy ξ, and eccentricity e are

$$p = \frac{\left|\vec{r} \times \vec{v}\right|^2}{\mu}, \tag{11}$$

$$\xi = \frac{\left|\vec{v}\right|^2}{2} - \frac{\mu}{\left|\vec{r}\right|}, \tag{12}$$

$$e = \sqrt{1 + \frac{2\xi p}{\mu}}. \tag{13}$$

Maximum Time of Flight

The maximum time of flight to the rendezvous is not strictly limited, and a practical limit can be established by recognizing that a free neutron has a high probability of radioactive decay during a sufficiently long time of flight. However,

45

to construct a robust algorithm, the maximum time of flight can be chosen from limiting cases in the set of solutions to the rendezvous problem which includes orbital motion of the neutron. The chord c and semi-parameter s of the triangle defined by sides $\vec{r}_1$ and $\vec{r}_2$ are

$$c = \sqrt{\left|\vec{r}_1\right|^2 + \left|\vec{r}_2\right|^2 - 2\left(\vec{r}_1 \cdot \vec{r}_2\right)} \tag{14}$$

$$s = \frac{\left|\vec{r}_1\right| + \left|\vec{r}_2\right| + c}{2}. \tag{15}$$

These are used for determining time of flight on special orbits joining two points $\vec{r}_1$ and $\vec{r}_2$. If the emission speed and speed of the emission frame are such that neutron has sufficient energy to escape the gravitational pull of the earth regardless of emission direction, i.e.

$$\left(\xi_n^{min} = \frac{\left(s_1^{ef} - \left|\vec{u}_{ef}\right|\right)^2}{2} - \frac{\mu}{\left|\vec{r}_1\right|}\right) \geq 0, \tag{16}$$

then the maximum time of flight is no more than the time of flight on a parabolic trajectory

$$\Delta t_{parabolic} = \frac{2}{3}\sqrt{\frac{s^3}{2\mu}}\left(1 - \left(\frac{s-c}{s}\right)^{3/2}\right). \tag{17}$$

46

If the condition in (16) is not met, then elliptical trajectories must be considered and maximum time of flight to an outbound rendezvous may be bounded by the time of flight on the minimum energy elliptical trajectory

$$\Delta t_{minV} = \frac{1}{2}\sqrt{\frac{s^3}{2\mu}}\left(\pi - \beta_e + \sin\beta_e\right) \tag{18}$$

where

$$\beta_e = 2\arcsin\sqrt{\frac{s-c}{s}}.$$

The bound for maximum time of flight computed from (17) or (18) depends on the location of the rendezvous which in turn depends on the time of flight. Thus, (17) or (18) is applied iteratively to find the bound for maximum time of flight. It is important to note that when elliptical neutron trajectories are considered that Δt_{minV} is not an actual upper bound for the time of flight to rendezvous: It is simply a practical limit for the case of a neutron making a flight to a geostationary detector. This practical limit excludes rendezvous trajectories that travel upward past the orbit of the detector and then fall back down and make a rendezvous on the return portion of the elliptical trajectory. For detectors at geostationary altitudes, this is an acceptable exclusion because the probability of radioactive decay of a free neutron on these long times of flight is high. Should detectors at lower altitudes be considered, where the time of flight on an elliptical

return trajectory is not as long, the procedure would need to be modified to account for these possibilities.

Required Speed for Rendezvous

This algorithm requires a subprogram to calculate the required neutron speed in the emergence frame given the time of flight.

Required Speed for Rendezvous

In($\vec{r}_1$, Δt, $\vec{r}_{sat}$, $\vec{v}_{sat}$ **) Out(** $s_1^{ef}(\Delta t)$ **)**

1. Compute a location for the rendezvous, $\vec{r}_2$, by solving Kepler's problem for the satellite given Δt: $\quad \vec{r}_2 = \mathcal{K}_{\vec{r}}(\vec{r}_{sat}, \vec{v}_{sat}, \Delta t)$

2. Find the emission velocity, $\vec{v}_1$, for a trajectory joining $\vec{r}_1$ and $\vec{r}_2$ with time of flight Δt:

   Accounting for gravity, $\vec{v}_1$ is found by solving Lambert's problem: $\quad \vec{v}_1 = \mathcal{L}_1(\vec{r}_1, \vec{r}_2, \Delta t)$.

   Neglecting gravity, $\vec{v}_1$ is trivially $\vec{v}_1 = \dfrac{\vec{r}_2 - \vec{r}_1}{\Delta t}$.

3. Shift to the emergence frame and compute the speed required for rendezvous: $\quad s_1^{ef} = \left| \vec{v}_1 - \vec{u}_{ef} \right|$.

Checking a Clear Flight Path

Once the direction and speed required to achieve a rendezvous are found, the flight path to that rendezvous must be checked for obstructions to confirm that the rendezvous is possible. For neutron following an orbital trajectory, this

48

is accomplished by first checking if the neutron flies through periapsis (the closest point to the center of the earth) on the flight path to the detector. Periapsis is traversed when

$$\left(\vec{r}_1 \cdot \vec{v}_1\right) < 0 \quad \text{AND} \quad \left(\vec{r}_2 \cdot \vec{v}_2\right) \geq 0. \tag{19}$$

If the condition in (19) is met, then the neutron passes through periapsis on the flight path to the detector. If the radius at periapsis, r_p from (9), is less than the radius of the earth, $R_\oplus$, then the flight path to the detector is obstructed by the earth. Otherwise, if the condition in (19) is not met or $r_p > R_\oplus$, then the flight path is unobstructed and the rendezvous is possible.

If gravity is neglected, the check for flight path simplifies to a check for line of sight along a straight line from the emission point to the location of the rendezvous. The radius of closest approach to the center of the earth, r_{ca}, on the *straight* flight path is:

$$\zeta_1 = \frac{\vec{r}_1 \cdot \vec{v}_1}{\left|\vec{r}_1\right|\left|\vec{v}_1\right|}$$

$$r_{ca} = \begin{cases} \left|\vec{r}_1\right| & \zeta_1 \geq 0 \\ \left|\vec{r}_1\right|\sqrt{1 - \zeta_1^2} & \zeta_1 < 0 \end{cases} \tag{20}$$

If $r_{ca} > R_\oplus$, then the *straight* flight path is unobstructed and the rendezvous is possible.

Neutron Intercept State

Once the orbital trajectory to achieve rendezvous with the detector is found, the remaining properties of the neutron flight and intercept can be computed. The relevant state variables are time of flight Δt, emission zenith cosine ζ_1, emission energy E_1, intercept energy E_a^{df}, intercept nadir cosine η_a^{df}, and intercept azimuth angle ω_a^{df}. Time of flight Δt and emission velocity $\vec{v}_1$ are results of the procedure for finding the rendezvous. The velocity of the neutron at intercept is found by solving Lambert's problem for the known time of flight

$$\vec{v}_2 = \mathcal{L}_2(\vec{r}_1, \vec{r}_2, \Delta t). \tag{21}$$

Alternatively, $\vec{v}_2$ could be computed as a side effect during the iteration to find Δt and $\vec{v}_1$ for the rendezvous. In the case where gravity is neglected $\vec{v}_2$ is trivially $\vec{v}_2 = \vec{v}_1$.

Emission zenith cosine and emission energy are

$$\zeta_1 = \frac{\vec{r}_1 \cdot \vec{v}_1}{\left|\vec{r}_1\right|\left|\vec{v}_1\right|} \tag{22}$$

$$E_1 = \left(\frac{\left|\vec{v}_1\right|}{k_{sp}}\right)^2 \tag{23}$$

where k_{sp} is a conversion constant

$$k_{sp} \equiv K_{\text{km/m}}\sqrt{\frac{2}{K_{keV/J}m_n}}. \tag{24}$$

50

The intercept energy is the energy of the neutron at intercept in the reference frame of the detector

$$E_a^{df} = \left(\frac{\left\| \vec{v}_2^{df} \right\|}{k_{sp}} \right)^2 , \tag{25}$$

the intercept nadir cosine is the cosine of the angle from downward of the direction of arrival of the neutron

$$\eta_a^{df} = -\frac{\vec{r}_2 \cdot \vec{v}_2^{df}}{\left| \vec{r}_2 \right| \left| \vec{v}_2^{df} \right|} , \tag{26}$$

and the intercept azimuth angle is

$$\omega_a^{df} = \mathrm{atan2} \left[\left(\vec{v}_2^{df} \cdot \widehat{ON} \right), \left(\vec{v}_2^{df} \cdot \widehat{F} \right) \right] \tag{27}$$

where $\vec{v}_2^{df}$ is the neutron velocity at intercept in the frame of reference of the detector

$$\vec{v}_2^{df} = \vec{v}_2 - \vec{v}_d(t_e + \Delta t) , \tag{28}$$

$\vec{v}_d(t_e + \Delta t)$ is the velocity of the detector in the ECI frame at the time of intercept, $\mathrm{atan2}$ is the two-argument inverse tangent function that returns its result in the proper quadrant, and $\widehat{ON}$ and $\widehat{F}$ are the orbit normal and forward basis vectors in the detector frame.

Failure of the Bracketing Method and Multiple Roots

Two notes on implementation of the algorithm for finding a neutron rendezvous: First, during the main iteration (step 4 of the algorithm **Find Neutron Rendezvous**), the brackets could move to exclude the root being sought. This occurs when the position of the target (hence the velocity required to reach it) changes rapidly. The failure mode is easily detected by checking the sign of

$$\left(s_1^{ef}(\Delta t_{min}) - s_1^{ef} \right) \left(s_1^{ef}(\Delta t_{max}) - s_1^{ef} \right) \tag{29}$$

Where $s_1^{ef}(\Delta t_{min})$ and $s_1^{ef}(\Delta t_{max})$ are found using the algorithm **Required Speed for Rendezvous**. If the product in (29) is positive, then the factors have the same sign and a root is no longer bracketed. To recover, restart the iteration with revised brackets

$$\left(\Delta t_{min}_{\substack{n=0}}, \Delta t_{min}_{\substack{n=n}} \right) \text{ for } \left(s_1^{ef}(\Delta t_{min}) - s_1^{ef} \right) < 0$$

$$\text{OR} \tag{30}$$

$$\left(\Delta t_{max}_{\substack{n=n}}, \Delta t_{max}_{\substack{n=0}} \right) \text{ for } \left(s_1^{ef}(\Delta t_{max}) - s_1^{ef} \right) > 0.$$

Second, no explicit handling is included in this algorithm for finding multiple roots when they exist. Should multiple roots be of interest, the available and required velocity curves may be partitioned into regions containing one root each. Then the contributions for each rendezvous would be determined.

Contributions resulting from multiple solutions to the rendezvous problem are independent of one another and would be tallied accordingly. Thus, by ignoring multiple roots, we may be underestimating the expected value by a small amount. However, the independent property of contributions from multiple roots is violated if the root has multiplicity. In this case, the same emergence velocity found by the search results in multiple rendezvous with unique times of flight. For roots with multiplicity, the contributions with longer times of flight must include a conditional probability that the neutron did not collide during an earlier rendezvous with the detector. It is also worth mentioning that while it is easy to construct single rendezvous scenarios where these issues arise, such circumstances are rarely encountered in practical transport calculations. The likelihood of multiplicity is essentially equivalent to the likelihood of aligning two objects with sizes measured in meters, separated from the viewer and each other by thousands of kilometers, so precisely that one cannot be seen because the other obstructs the view of it.

IV. The Divergence Factor

The divergence factor accounts density for the spreading apart of neutrons that start with slightly different initial velocities. In the usual problem, without motion of the emitter and detector, the probability that an isotropically-emitted neutron will intercept the detector is simply the cross-sectional area of the detector normal to the radius vector from the emitter to the detector, times $\left(4\pi\right)^{-1}$ (the directional probability density), times $1/r^2$ (here referred to as the *divergence factor*). More generally, neutrons emitted in a small solid angle in the emergence frame, $\Delta\Omega^{ef}$, travel to and enter the detector (if uncollided on route) through its effective cross-sectional area, A_{eff}. The effective area is usually greater than the actual detector area, A_d. Thus, the probability that the neutrons arrive at the detector is the product of the probability that they are emitted with directions in, or scattered into directions in $\Delta\hat{\Omega}^{ef}$ times the probability that they don't collide on route. The divergence factor is

$$F_{divergence} = \left(\frac{\Delta\Omega^{ef}}{A_{eff}}\right)\left(\frac{A_{eff}}{A_d}\right). \tag{31}$$

With this, the probability of detection is

$$P_{\text{detect}} = P(\text{detect}|\text{neutron enters detector})$$
$$\times P(\text{not collide enroute})f^{ef}(\hat{\Omega})F_{divergence}, \tag{32}$$

where $f^{ef}(\hat{\Omega})$ is the probability density function for the angular distribution of emission or scatter in the rest frame of the source or the CM frame of the scatter, respectively, and $\hat{\Omega}$ is the direction of emission in the source frame that sends the neutron to the center of the detector.

In this chapter, the formula for the divergence factor is derived first to account for the relative motions but without gravity. Then the influences of gravity are addressed and an algorithm for this case is presented.

Divergence with Relative Motions but without Gravity

In the absence of gravity, a stationary monoenergetic and isotropic emitter at $\vec{r}_1$ emits neutrons that intercept a stationary spherical detector at $\vec{r}_2$. For a stationary spherical detector $A_{eff} = A_d$ and the divergence factor on a straight trajectory from $\vec{r}_1$ to $\vec{r}_2$ is

$$F_{divergence}^{stationary} = \frac{1}{\left|\vec{r}_2 - \vec{r}_1\right|^2} \quad , \tag{33}$$

which is the familiar $1/r^2$ spherical divergence factor. In the rest frame of the source (the ECI frame for a stationary source), a neutron is emitted in some direction, with speed v independent of the direction of emission. After time of flight Δt, the neutron must lie somewhere on the sphere of radius $v\Delta t$ centered on the source. This sphere is the locus of points where the neutron could be found at this time of flight. This surface is hereinafter referred to as the neutron

locus. At time of flight $v\,\Delta t = \left|\vec{r}_1 - \vec{r}_2\right|$, the detector is on the locus. This yields the divergence factor in equation (33).

Relax the restrictions of a stationary emission point and detector (but still in the absence of gravity): The emitter at $\vec{r}_1$ has velocity $\vec{u}_{ef}$ and emits neutrons with speed s_1^{ef} in the emergence frame at time t_e. After time of flight Δt the neutrons intercept the spherical detector at $\vec{r}_2$ which has velocity $\vec{v}_d$ at the time of intercept. This influences the divergence factor in two ways: First, the center of the neutron locus moves in the ECI frame during the neutron flight to the detector. Second, the motion of the detector at the time of the intercept effectively *smears* the detector through the surface of the neutron locus during intercept increasing the geometric cross-sectional area of the detector A_d to its effective cross-sectional area A_{eff}. Assuming a spherical detector, and stationary neutron locus with negligible curvature at time of intercept, this increase is proportional to the inverse of the absolute value of the cosine of the angle between the incident direction and the direction of detector motion. Thus, the divergence factor becomes

$$F_{divergence}^{motion} = \frac{1}{\left|\vec{r}_2 - \left(\vec{r}_1 + \vec{u}_{ef}\Delta t\right)\right|^2}\frac{1}{|\alpha|} \tag{34}$$

where

$$\alpha = \frac{\left(\vec{v}_d^{\,ef} - \vec{v}_1^{\,ef}\right) \cdot \hat{n}_{locus}}{\left|\vec{v}_d^{\,ef} - \vec{v}_1^{\,ef}\right|}. \tag{35}$$

and $\hat{n}_{locus}$ is a unit vector normal to the locus surface at the time of intercept. In the case of a neutron traveling in a straight line to the intercept (no gravity),

$$\hat{n}_{locus} = \frac{\vec{r}_2 - \left(\vec{r}_1 + \vec{u}_{ef}\Delta t\right)}{\left|\vec{r}_2 - \left(\vec{r}_1 + \vec{u}_{ef}\Delta t\right)\right|} = \frac{\vec{v}_1^{ef}}{\left|\vec{v}_1^{ef}\right|} . \tag{36}$$

As a result of the assumption of a flat stationary neutron locus, as α approaches zero (perpendicular incidence), the effective area of the detector across the neutron locus is overestimated and eventually unbounded as $\alpha \to 0$. This approach may be patched by establishing some practical limit on $\left|\alpha\right|$, amending (34) with

$$\alpha_{patched} = \max\left[\alpha, \frac{1}{10}\right] \tag{37}$$

but this is less than satisfactory.

Retaining the assumption of negligible curvature in the neutron locus near $\vec{r}_2$ at the time of intercept, but recognizing that the locus surface moves with the velocity of the intercepting neutron

$$\vec{v}_2 = s_1^{ef} \frac{\vec{r}_2 - \left(\vec{r}_1 + \vec{u}_{ef}\Delta t\right)}{\left|\vec{r}_2 - \left(\vec{r}_1 + \vec{u}_{ef}\Delta t\right)\right|} + \vec{u}_{ef} , \tag{38}$$

the detector velocity in the frame of reference of the surface of the locus at intercept is $\vec{v}_d^n = \vec{v}_d - \vec{v}_2$. Thus, α in (34) is replaced by

$$\alpha_{patched}^n = \max\left[\left|\frac{\vec{v}_d^n \cdot \hat{n}_{locus}}{\left|\vec{v}_d^n\right|}\right|, \frac{1}{10}\right] \tag{39}$$

which, by adding consideration of the motion of the locus surface, reduces the likelihood of α near zero. It remains necessary for a practical limit to the value of α^n to be established as in (37), but this limit was rarely invoked in computing the results presented here.

Further refinements are possible, but not pursued here, beginning with consideration of the curvature of the locus. The formulation using (34) and (39) are adequate to investigate the influence of relative motions on the divergence factor.

Divergence with Relative Motions and Gravity

With gravity, the motion of the locus is no longer equal to the motion of a neutron in the locus. Consider a plane locus with the neutrons moving in the plane of the locus; the locus does not move but the neutrons do. The detector can arrive at normal incidence to the plane. The faster the neutrons move laterally in the plane, the more of them collide with the detector. In general, the formula for α is

$$\alpha = \left|\hat{n}_{locus} \cdot \hat{v}_{rel}\right|, \tag{40}$$

where $\hat{n}_{locus}$ is a unit vector normal to the plane of the locus at the point (in space and time) at which the center of the detector sphere passes through the locus and $\hat{v}_{rel}$ is the velocity of the detector relative to a neutron in the locus at that same point (in space in time). This is consistent with equation (35) developed without gravity. As long as the locus has negligible curvature over the length of the region of intersection (the diameter of the detector sphere divided by α) compared to the thickness of the detector normal to the surface (the diameter of the detector sphere), the factor of $1/\alpha$ is acceptable.

Also, with gravity, the locus changes shape as the neutrons follow differently-curving paths with differently-changing speeds. Also, paths offset by a small difference in the initial direction and speed do not diverge steadily as do straight lines. For example, two elliptical orbits with the same perigee diverge as they climb to apogee, but converge again as the fall back to the same perigee. This is complicated by the differences in speed so that particles that start the two paths together arrive back at perigee at different times. To deal with all this, a shooting method was developed.

In short, the shooting method perturbs the emission direction of a neutron on a known intercept trajectory, and estimates the ratio $\Delta\Omega^{ef}/A_{eff}$ and adjusts the approximation for A_{eff}/A_d for the change in incident direction and speed from emission to intercept on the orbital rendezvous trajectory. A detailed description follows.

A neutron is emitted at $\vec{r}_1$ in direction $\hat{\Omega}_1^{ef}$ with speed s_1^{ef} from the emission frame which has velocity $\vec{u}_{ef}$. After time Δt, the neutron intercepts a detector at $\vec{r}_2$ that has velocity $\vec{v}_d$ at the time of intercept. The neutron velocity upon intercept with the detector is $\vec{v}_2$. These quantities are obtained as the solution to a preceding rendezvous problem.

In the emission frame, establish the coordinate basis vectors:

$$\hat{R} = \frac{\vec{r}_1}{\left|\vec{r}_1\right|}$$

$$\hat{N} = \frac{\hat{R} \times \hat{\Omega}_1^{ef}}{\left|\hat{R} \times \hat{\Omega}_1^{ef}\right|} \tag{41}$$

$$\hat{T} = \hat{N} \times \hat{\Omega}_1^{ef}$$

Create a set (four is convenient) of emission directions perturbed from the *central* emission direction $\hat{\Omega}_1^{ef}$ by ε in the $\pm\hat{N}$ and $\pm\hat{T}$ directions

$$\hat{\Omega}'^{ef}_{m=1,3} = \frac{\hat{\Omega}_1^{ef} \pm \varepsilon\hat{N}}{\left|\hat{\Omega}_1^{ef} \pm \varepsilon\hat{N}\right|}$$

$$\hat{\Omega}'^{ef}_{m=2,4} = \frac{\hat{\Omega}_1^{ef} \pm \varepsilon\hat{T}}{\left|\hat{\Omega}_1^{ef} \pm \varepsilon\hat{T}\right|} \tag{42}$$

Solve Kepler's problem (propagate the orbit) for each of the four orbital trajectories with emission directions from (42) with time of flight Δt:

$$\vec{r}'_m = \mathcal{K}_r(\vec{r}_n, s_1^{ef}\hat{\Omega}'^{ef}_m + \vec{u}_{ef}, \Delta t). \tag{43}$$

The four $\vec{r}'_m$ from (43), may be used to approximately describe the surface of the neutron locus in the vicinity of $\vec{r}'_2$ at the time of intercept. A normal vector to this approximated locus surface is

$$\hat{n}'_{locus} = \frac{\left(\vec{r}'_1 - \vec{r}'_3\right) \times \left(\vec{r}'_2 - \vec{r}'_4\right)}{\left|\left(\vec{r}'_1 - \vec{r}'_3\right) \times \left(\vec{r}'_2 - \vec{r}'_4\right)\right|}.$$ (44)

The cosine of the incidence angle of the detector motion on the neutron locus at intercept is estimated

$$\alpha'^n_{patched} = \max\left[\frac{\left(\vec{v}_d - \vec{v}_2\right) \cdot \hat{n}'_{locus}}{\left|\vec{v}_d - \vec{v}_2\right|}, \frac{1}{10}\right].$$ (45)

As before, it remains necessary for a practical limit to the value of α'^n to be established as in (37) and (39), but this limit was rarely invoked in computing the results presented here.

The divergence factor is then estimated as

$$F^{gravity}_{divergence} = \frac{\left|\left(\hat{\Omega}'^{ef}_1 - \hat{\Omega}'^{ef}_3\right) \times \left(\hat{\Omega}'^{ef}_2 - \hat{\Omega}'^{ef}_4\right)\right|}{\left|\left(\vec{r}'_1 - \vec{r}'_3\right) \times \left(\vec{r}'_2 - \vec{r}'_4\right)\right|} \frac{1}{\left|\alpha'^n_{patched}\right|}.$$ (46)

V. Optical Thickness along a Trajectory through the Atmosphere

Effective Path Length

The effective path length (EPL), symbol L, is defined as the path length through a medium of uniform density $\overline{\rho}$ having the same optical thickness as the actual path through the actual medium:

$$L = \int_0^{\Delta s} \frac{\rho\left(z_0 + \Delta z(s)\right)}{\overline{\rho}} ds \tag{47}$$

where Δs is the geometric length of path, z_0 is the geometric altitude at the beginning of the path, and $\Delta z(s)$ is the change in geometric altitude as a function of position s along the path. For a straight path,

$$\Delta z(s) = \frac{s^2 + 2r_0\zeta_0 s}{r_0 + \sqrt{r_0^2 + s^2 + 2r_0\zeta_0 s}} \quad , \tag{48}$$

where r_0 is the distance from the center of the earth at the start of the path $(r_0 = R_\oplus + z_0)$ and ζ_0 is the cosine of the zenith angle at the start of the path.

Equation (47) is easily evaluated using numerical quadrature by partitioning the ray into segments that each lie in a single atmospheric layer. The effective path length on any such segment is approximated by Gauss-Legendre quadrature

$$\tilde{L}_b = \frac{\Delta s_b}{2\overline{\rho}} \sum_{i=1}^{n} w_i \rho(Z_{b-1} + \Delta z(s_i)) \tag{49}$$

where Δs_b is the length of the segment, Z_{b-1} is the altitude of the base of the atmospheric layer, and w_i is the Gauss-Legendre weight corresponding to the Gauss-Legendre abscissa a_i used to find s_i by

$$s_i = \frac{\Delta s_b}{2}\left(a_i + 1\right). \tag{50}$$

Computational efficiency can be improved by changing the variable of integration to z:

$$L = \int_{z_0}^{z_0 + \Delta z} \frac{\rho(z)}{\overline{\rho}} \frac{r_0 + z}{\sqrt{r_0^2 \zeta_0^2 + 2r_0 z + z^2}} dz \tag{51}$$

where Δz is the change in altitude from beginning to the end of the path. For convenience, also introduce the constraint that only upward paths ($\zeta_0 \geq 0$ and $\Delta z > 0$) are considered. The formulation for an upward path is well-conditioned. Because the integral is independent of the direction of integration along the path, downward paths become upward paths by swapping the roles of the endpoints. Paths with downward and upward parts are partitioned at the lowest point on the path into two upward paths (from there to each endpoint in turn). As before, the effective path length in any single atmospheric layer is approximated by Gauss-Legendre quadrature

$$\tilde{L}_b = \frac{\Delta Z_b}{2\overline{\rho}} \sum_{i=1}^{n} \frac{w_i \rho(Z_{b-1} + z_i)\left(\left(R_\oplus + Z_{b-1}\right) + \left(Z_{b-1} + z_i\right)\right)}{\sqrt{\left(R_\oplus + Z_{b-1}\right)^2 \zeta_0^2 + 2\left(R_\oplus + Z_{b-1}\right)\left(Z_{b-1} + z_i\right) + \left(Z_{b-1} + z_i\right)^2}} \tag{52}$$

63

where ΔZ_b is the change in altitude on the segment in the layer and each z_i corresponds to a Gauss-Legendre abscissa a_i

$$z_i = \frac{\Delta Z_b}{2}\left(a_i + 1\right). \tag{53}$$

Computational efficiency is enhanced when computing paths through full atmospheric layers because the location of quadrature points in altitude is known ahead of time so the density function $\rho(Z_{b-1} + z_i)$ may be precomputed. Only factors containing ζ_0 need to be evaluated at runtime, so equation (52) may be written as

$$\tilde{L} = \sum_{i=1}^{n} \frac{A_i}{\sqrt{B\zeta_0^2 + C_i}} \quad , \tag{54}$$

where

$$
\begin{aligned}
A_i &= \frac{\Delta Z_b}{2\bar{\rho}}\, w_i \rho(Z_{b-1} + z_i)\left(\left(R_\oplus + Z_{b-1}\right) + \left(Z_{b-1} + z_i\right)\right) \\
B &= \left(R_\oplus + Z_{b-1}\right)^2 \\
C_i &= 2\left(R_\oplus + Z_{b-1}\right)\left(Z_{b-1} + z_i\right) + \left(Z_{b-1} + z_i\right)^2
\end{aligned} \tag{55}
$$

are precomputed and stored for each full atmospheric layer.

Evaluation of equation (51) by Gauss-Legendre quadrature performs poorly for small ζ_0. In this case, Gauss-Legendre quadrature may be used to evaluate equation (47) effectively despite the higher computational cost.

The effective path length as a function of zenith cosine ζ_0 for various starting altitudes to the top of the atmosphere is shown in Figure 9.
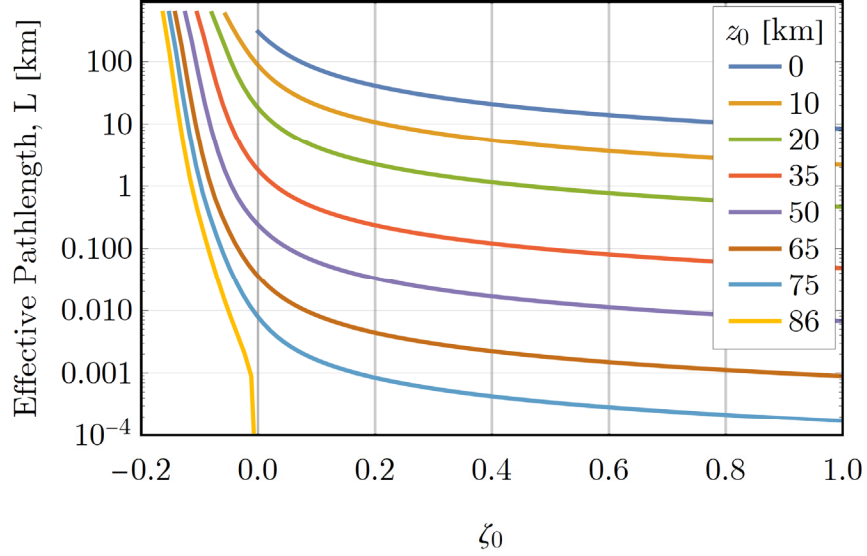
Figure 9: **Effective path length to the top of the atmosphere (86 km) for various starting altitudes.**

Rotation of the earth

The earth, including the atmosphere, rotates eastward in the inertial reference frame. The speed of the air in the inertial frame is a function of altitude z and latitude ϕ:

$$s_{air}(z,\phi) = \omega_\oplus \left(R_\oplus + z\right)\cos\phi . \tag{56}$$

The speed of the atmosphere in the inertial frame as a function of altitude and latitude is plotted in Figure 10. For a sense of scale relative to the speed of neutrons during the transport calculation, neutron speed as a function of kinetic

energy is plotted in Figure 11. A neutron with approximately 0.0013 eV has the same velocity as the maximum rotational speed of the atmosphere (0.5 km/s).
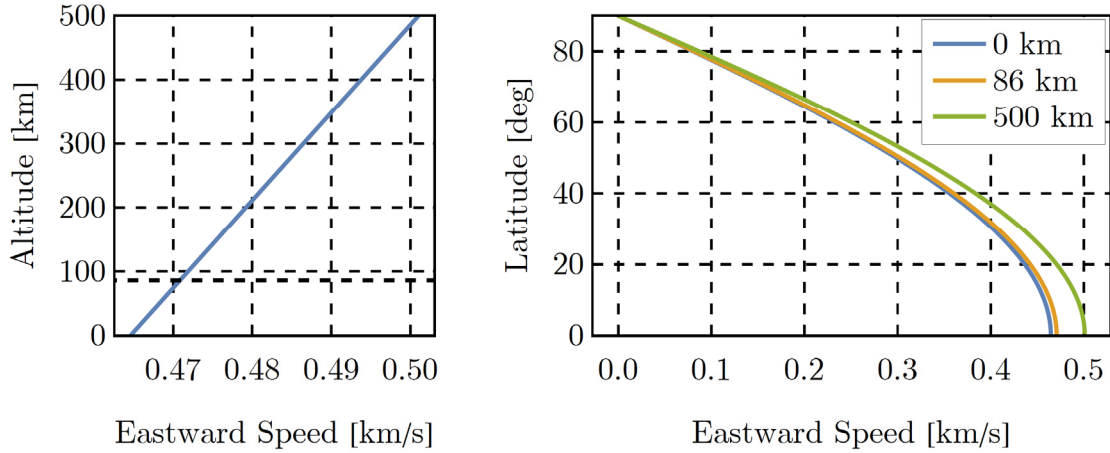
Figure 10: Speed of the rotating atmosphere as a function of altitude and latitude.
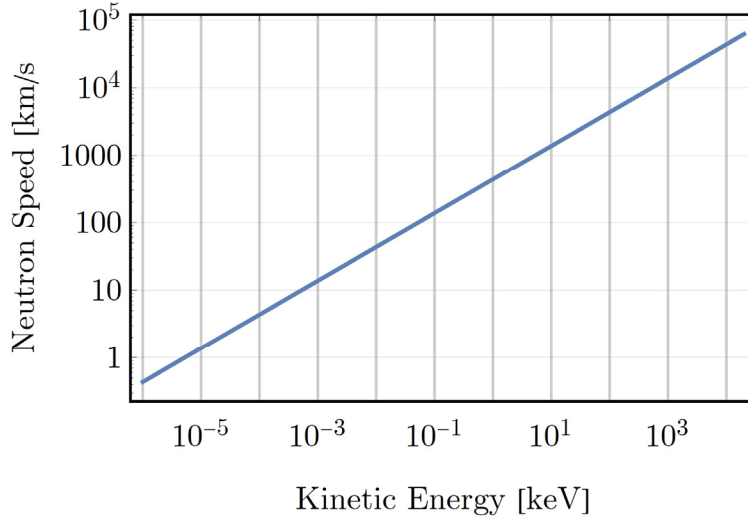
Figure 11: Neutron Speed as a function of kinetic energy.

The rotation of the atmosphere introduces a location-dependent and heading-dependent component to the optical thickness seen by a neutron along a path through the atmosphere as a result of the atmosphere sweeping past the

path during the time the neutron takes to traverse it. The corrected effective path length is

$$L_{rot} = \int_{z_0}^{z_0 + \Delta z} \frac{\rho(z)}{\bar{\rho}} \frac{r_0 + z}{\sqrt{r_0^2 \zeta_0^2 + 2 r_0 z + z^2}} C_{af}(E_n, \zeta_0, \theta_h, \phi, z) dz \qquad (57)$$

where E_n is the kinetic energy of the neutron, θ_h is the heading measured eastward from true north, ϕ is the latitude of the neutron, and C_{af} is a correction factor for the speed of the air along the path

$$\begin{aligned} C_{af}(E_n, \zeta_0, \theta_h, \phi, z) &= \frac{s_n^{af}(E_n, \zeta_0, \theta_h, \phi, z)}{s_n(E_n)} \\ &= 1 - \sqrt{1 - \zeta_0^2} \, \text{Sin}(\theta_h) \frac{s_{air}(z, \phi)}{s_n(E_n)} \end{aligned} \qquad (58)$$

where the speed of a neutron with kinetic energy E_n in the ECI frame is

$$s_n(E_n) = k_{sp} \sqrt{E_n} \qquad (59)$$

with k_{sp} from (24). (This correction is an option in HATS-n, but was not used in obtaining the results presented here.)

Optical Thickness Through the Atmosphere Along Kepler Trajectories

With the consideration of gravity, the neutron travels through the atmosphere along an orbital trajectory. The trajectory is defined by the specific mechanical energy and semi-parameter (equations (11) and (12)). The effective

path length along an upward ($\zeta_0 \geq 0$ and $Z_0 < Z_1$) orbital trajectory through the atmosphere is

$$L_k = \int_{r_0}^{r_0 + \Delta z} \frac{\rho(r - R_\oplus)}{\overline{\rho}} \frac{\sqrt{2r\left(1 + \dfrac{\xi}{\mu}r\right)}}{\sqrt{2r\left(1 + \dfrac{\xi}{\mu}r\right) - p}} dr \tag{60}$$

where ξ is the specific mechanical energy of the orbital trajectory from (12). As with straight paths, only upward paths are considered, and downward or downward and upward paths may be represented as the superposition of one or more upward paths.

The effective path length in any single atmospheric layer is approximated by Gauss-Legendre quadrature

$$\tilde{L}_{k,b} =$$

$$\frac{\Delta Z_b}{2\overline{\rho}} \sum_{i=1}^{n} \frac{w_i \rho(Z_{b-1} + z_i) \sqrt{2\left(R_\oplus + Z_{b-1} + z_i\right)\left[1 + \dfrac{\xi}{\mu}\left(R_\oplus + Z_{b-1} + z_i\right)\right]}}{\sqrt{2\left(R_\oplus + Z_{b-1} + z_i\right)\left[1 + \dfrac{\xi}{\mu}\left(R_\oplus + Z_{b-1} + z_i\right)\right] - p}} \tag{61}$$

where ΔZ_b is the change in altitude on the segment in the layer and each z_i corresponds to a Gauss-Legendre abscissa a_i

$$z_i = \frac{\Delta Z_b}{2}\left(a_i + 1\right) \tag{62}$$

and p is the semi-parameter of the orbital trajectory from (11). As before, computational efficiency is enhanced when computing paths through full atmospheric layers because the distribution of quadrature points in altitude is known ahead of time so the density function $\rho(Z_{b-1} + z_i)$ may be precomputed. Only factors in equation (61) containing ξ and p need to be evaluated at runtime so it may be written as

$$\tilde{L}_{k,b} = \sum_{i=1}^{n} \frac{A_i \sqrt{B_i \left(1 + \xi C_i\right)}}{\sqrt{B_i \left(1 + \xi C_i\right) - p}} \tag{63}$$

where

$$
\begin{aligned}
A_i &= \frac{\Delta Z_b}{2\overline{\rho}} w_i \rho(Z_{b-1} + z_i) \\
B_i &= 2\left(R_{\oplus} + Z_{b-1} + z_i\right) \\
C_i &= \frac{\left(R_{\oplus} + Z_{b-1} + z_i\right)}{\mu}
\end{aligned} \tag{64}
$$

are precomputed and stored for each full atmospheric layer.

As with the effective path length on straight paths, evaluation of (60) by Gauss-Legendre quadrature performs poorly for small ζ_0. In this case, the variable of integration may be changed to true anomaly ν, and with eccentricity e from (13), the effective path length is

$$L_k = p \int_{\nu_0}^{\nu_1} \frac{\rho(z(\nu))}{\overline{\rho}} \frac{\sqrt{1 + e^2 + 2e\cos\nu}}{\left(1 + e\cos\nu\right)^2} d\nu \tag{65}$$

69

where the limits of integration are

$$\nu_0 = \arccos\left(\frac{p - r_0}{e r_0}\right)$$

$$\nu_1 = \arccos\left(\frac{p - \left(r_0 + \Delta z\right)}{e\left(r_0 + \Delta z\right)}\right)$$

(66)

and $z(\nu)$ is obtained using the orbit equation

$$z(\nu) = \frac{p}{1 + e \cos \nu} - r_0.$$

(67)

The effective path length through a single layer is then approximated using Gauss-Legendre quadrature

$$\tilde{L}_{k,b} = \frac{p \Delta \nu_b}{\bar{\rho}} \sum_{i=1}^{n} \frac{w_i \rho(z(\nu_i))\sqrt{1 + e^2 + 2e \cos \nu_i}}{\left(1 + e \cos \nu_i\right)^2}$$

(68)

where $\Delta \nu_b$ is the change in true anomaly on the segment in the layer and each ν_i corresponds to a Gauss-Legendre abscissa a_i

$$\nu_i = \frac{\Delta \nu_b}{2}\left(a_i + 1\right).$$

(69)

Despite poor numerical conditioning (in (66) and (67)), this formulation is adequate for the precision sought when evaluated using double precision and Gauss-Legendre quadrature for small ζ_0. If higher precision is required, and to further enhance computational efficiency, the variable of integration may be changed to $v = \sqrt{1 - \cos \nu_1} - \sqrt{1 - \cos \nu_0}$, but this step is not required here.

70

The Effect of Optical Thickness on the Transport Calculation

The sensitivity of the transport calculation to the effective path length (and the precision achieved in computing it) depends on the kinetic energy of the neutron traversing the path and the cross section of the transport medium. For context, consider the probability of a neutron escaping the atmosphere for various effective path lengths, Figure 12. For short effective path length (e.g. 1 mm), the probability of escape remains large except for the lowest kinetic energies where the atmosphere becomes very optically thick. For long effective path lengths (e.g. 1 km or greater), the probability of escape is low for all energies, and effectively zero below 10 keV. In the mid ranges of effective path length, 0.1 to 0.5 km or so, observe the sensitivity in escape probability to effective path length. In this region of effective path length, the probability of escape for neutrons with kinetic energy below 1 MeV varies rapidly with effective path length.
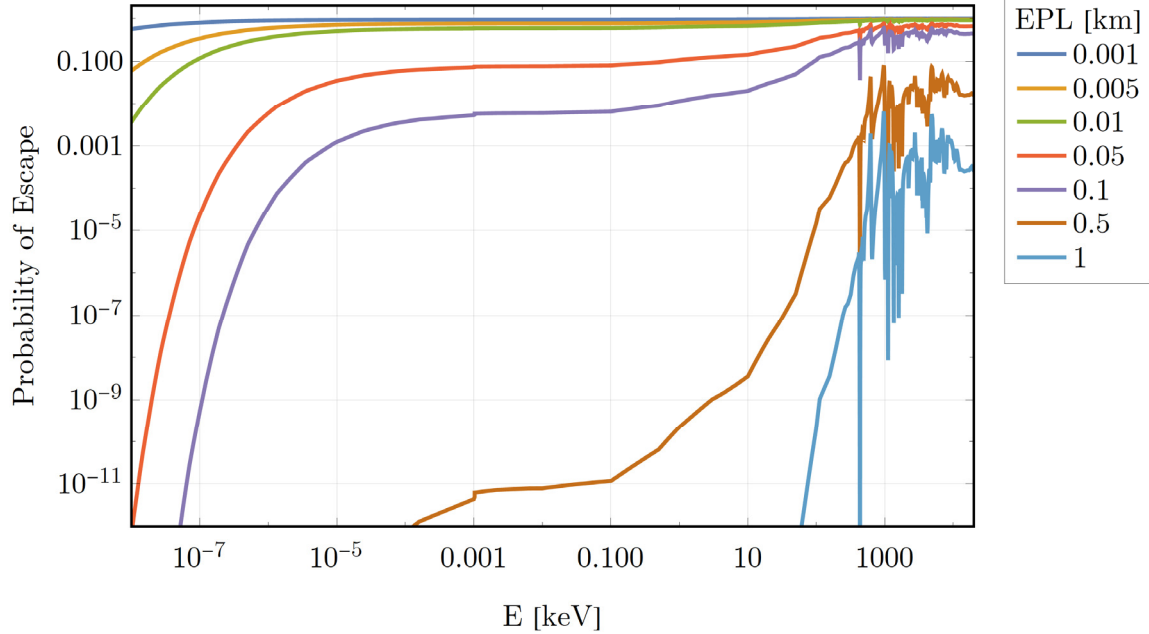
Figure 12: Probability of neutron escape from the atmosphere as a function of kinetic energy for various effective path lengths to escape.

Fidelity of the Atmosphere Model

Continuous vs Discrete Representation

In a traditional approach to the air-to-space transport problem, the density of the atmosphere would be approximated by dividing the atmosphere into concentric shells within which the atmospheric properties vary by a small enough amount that they may be considered constant. For general transport calculations, this speeds the process of determining the material properties at a given location (temperature, density, composition, etc.) at the expense of increased geometric complexity in the problem representation which increases computational overhead in the raytracing procedure. In a system with *sharp* boundaries (e.g. a

72

reactor with fuel, cladding, coolant, etc.), the benefit of this approach is clear because the geometry of the problem contains natural boundaries at which to transition from one region to another. However, in the case of the air-to-space problem, the overhead introduced in the raytracing process is considerable when compared to the cost of continuous evaluation of the atmospheric properties. The validity of the previous statement depends on the selected atmosphere model, but the author believes that a model of considerable complexity would have to be introduced to balance the raytracing overhead.

Aside from the practical code design considerations, the discretization of the atmosphere introduces considerable error in the calculation of effective path length. In a representation of the atmosphere using layers with constant density, the effective path length is computed using an implied composite low-order quadrature with a fixed number of quadrature points per unit altitude. A continuous representation can utilize a higher order quadrature for the effective path-length integrals, as well as adaptive spacing of quadrature points to enhance speed and precision.

High Altitude Atmosphere

When simulating the transport of neutrons from the atmosphere to space, it is convenient, and necessary to the construction of the estimator, to establish some altitude above which the atmosphere is negligible and is considered vacuum. When using the 1976 U.S. Standard Atmosphere (NOAA, NASA,

USAF, 1976), a convenient altitude is 86 km: Below this altitude the atmosphere is turbulently mixed and of constant composition with temperature variation piecewise-linear with altitude which simplifies the empirical model for determining atmospheric density. Above 86 kilometers, the fractional composition of the atmosphere is no longer constant and the temperature variation with altitude takes forms other than linear. As a result, the calculation of atmospheric composition and density given altitude is considerably more complex and costly. The relevant quantities and equations to compute atmospheric composition and density for the 1976 U.S. Standard Atmosphere (USSA-76) are summarized in *Appendix B. Summary of U.S. Standard Atmosphere 1976.*

Addition of an extended (high-altitude) atmosphere model to the transport problem adds two areas for consideration: First, the optical thickness through the high-altitude region must be considered when computing effective path lengths. Second, the geometric extent of the scattering medium is extended changing the geometric distribution of scatters. Further, additional complexity is introduced in computation of cross sections and scatter kinetics as a result of variation in composition and temperature of the atmosphere in the extended scattering region.

Atmospheric Constituents

When choosing and atmospheric representation, an important feature of the model is the number and choice of atmospheric constituents to be included in the

composition of the scattering medium. In particular, the interaction cross sections for the scattering medium may vary greatly depending on the section of atmospheric constituents. Commonly, when describing the atmosphere, only Nitrogen and Oxygen are considered because they make up more than 99% of the atmosphere near the surface of the earth. Unfortunately, this fails to consider the relative cross section of these and other elements, as well as less abundant isotopes, as a function of incident neutron energy.

The atmosphere below 86 kilometers (as described by USSA-76) is considered turbulently mixed with constant fractional composition (NOAA, NASA, USAF, 1976, p. 3). The fractional composition by isotope of the four most common elements in sea-level dry air from this model is listed in Table 4.

Table 4: **Relative fractions by isotope of Nitrogen, Oxygen, Argon, and Carbon of sea-level dry air.**

Isotope	Relative Fraction
^{14}N	7.77717×10^{-1}
^{16}O	2.08973×10^{-1}
^{40}Ar	9.3031×10^{-3}
^{15}N	3.12336×10^{-3}
^{18}O	4.18952×10^{-4}
^{12}C	3.10546×10^{-4}
^{17}O	8.37904×10^{-5}
^{36}Ar	3.11956×10^{-5}
^{38}Ar	5.8842×10^{-6}
^{13}C	3.454×10^{-6}

Additionally, but not considered here, in the case where the high-altitude region of the atmosphere is included, the elements and isotopes of interest may change with altitude. In particular, the fraction of atomic (vs molecular) oxygen and the fractions of helium and hydrogen are not negligible above 86 kilometers in the USSA-76. The influence of helium and hydrogen cross sections and scattering kinetics on the air-to-space class of problems may be of importance due to the difference in scattering kinetics when compared to heavier atmospheric constituents. Nevertheless, the air is quite rarefied at these altitudes, so an investigation of this is not needed here.

VI. Motion of The Scattering Medium

Particles in the scattering medium undergo random thermal motion as well as bulk motion due to rotation of the atmosphere and wind/weather patterns. This influences the apparent cross sections of the scattering medium and changes the kinematics of scattering calculations.

Bulk Velocity in the Scattering Medium

The scattering medium moves in bulk due to rotation of the atmosphere with the earth, and wind or weather patterns. At any altitude and latitude, the velocity due to earth rotation can be computed from (56) and has an approximate maximum of 0.54 kilometers per second at 1000 kilometers above the equator. A major wind pattern, such as the Jetstream, in the atmosphere may also be of interest. Wind velocity of such a pattern could be as large as 0.18 km/s. Inclusion of winds was not attempted here.

Thermal Motion in the Scattering Medium

In addition to bulk motion of the atmosphere, individual atmospheric particles undergo random thermal motion. This influences the interaction cross section of the scattering medium by Doppler broadening, and the scattering

kinetics due to the contribution of kinetic energy of the scattering target nucleus to the total energy in the collision.

The Doppler broadened cross section for a neutron traveling with velocity v through a medium with temperature T is

$$\sigma(v,T) = \frac{\gamma}{v^2\sqrt{\pi}} \left(\sigma^*(v,T) - \sigma^*(-v,T) \right) \tag{70}$$

where $\gamma = \sqrt{M / \left(2k(T - T_0)\right)}$, M is the target mass, k is the Boltzmann constant, T_0 is the reference temperature for which cross section values are tabulated ($T_0 = 0K$ for unbroadened cross sections). The function $\sigma^*(v,T)$ is

$$\sigma^*(v,T) = \int_{v_r^{\min}}^{v_r^{\max}} v_r^2 \sigma_0(v_r) e^{-\left(\gamma\left(v - v_r\right)\right)^2} dv_r \tag{71}$$

where $\sigma_0(v_r)$ is the value of the unbroadened cross section evaluated at velocity v_r, and

$$v_r^{\max} = |v| + \frac{4}{\gamma}$$

$$v_r^{\min} = \begin{cases} 0 & |v| \le \dfrac{4}{\gamma} \\[2mm] \left| |v| - \dfrac{4}{\gamma} \right| & |v| > \dfrac{4}{\gamma} \end{cases} \tag{72}$$

(Romano & Trumbull, 2014).

The changes to scattering kinetics accounting for thermal (and bulk) motion of the scattering target are trivially implemented as a series of vector additions (bulk target velocity, sampled thermal velocity, neutron velocity) in the

calculation of the scatter parameters. This approach remains valid as long as the relative energies are such that the particles (neutron and nucleus) may be treated as points in the emission frame without the influence of any other mechanisms. As this assumption breaks down (i.e. low energy, hence slower, incident neutrons), a more complex scatter model is needed. This is beyond the scope of this research.

VII. Motion of the Source

If the neutron source has a velocity $\vec{v}_s$ in the ECI frame, then the distributions in direction and energy of emitted neutrons are in the frame of reference of the source, or the emergence frame. To convert the direction and energy (E_n^{ef} and $\hat{\Omega}_n^{ef}$) of an emitted neutron to the ECI frame (E_n and $\hat{\Omega}_n$):

$$\vec{v}_n = \vec{v}_n^{ef} + \vec{v}_s = k_{sp}\sqrt{E_n^{ef}}\,\hat{\Omega}_n^{ef} + \vec{v}_s$$

$$\hat{\Omega}_n = \frac{\vec{v}_n}{\left|\vec{v}_n\right|} \tag{73}$$

$$E_n = \left(\frac{\left|\vec{v}_n\right|}{k_{sp}}\right)^2.$$

The maximum likely source velocity is near 10 kilometers per second (Morris & Benson, 1963). For a sense of scale, this is similar to the velocity required to achieve geostationary altitude.

VIII. Radioactive Decay

Free neutrons have a mean lifetime τ_n between approximately 878 (Serebrov, et al., 2008) and 886 (Yue, et al., 2013) seconds (about 15 minutes). The value I used is 882 seconds. The probability that a neutron emitted from the source at time zero has not decayed before arriving at a detector after emerging from an interaction at time t_e and time of flight Δt is

$$P_n^{no\,decay} = e^{-\lambda_n\left(t_e + \Delta t\right)}, \tag{74}$$

where $\lambda_n = 1\,/\,\tau_n$ is the decay constant for free neutrons and τ_n is the mean lifetime of free neutrons listed in Table 2.

Time of flight from a point in the atmosphere to a geostationary detector ranges from less than one second to approximately 19,000 seconds for a minimum velocity orbital transfer. The actual maximum time of flight is larger than this, but the minimum velocity transfer is a suitable practical limit for this discussion. Assuming that the time spent between scatters in the atmosphere is small compared to the time of flight Δt, and evaluating (74) for contributions with the minimum and maximum times of flight reveals that the intensity of a contribution for the shortest time of flight is decreased by less than 0.07% while at the longest time of flight the intensity is reduced by twelve orders of magnitude.

The adjustment for radioactive decay may be applied to the time history of contributions as a post processing step, and thus the computational cost is irrelevant. However, it should be noted that this introduces errors in binned data that can be significant depending on the resolution of the grid to which it is applied and also the variance of the estimate to which it is applied. Additionally, if binned data does not include a dimension in time (e.g. nadir-azimuth direction bins data collected by HATS-n), then it is not possible to apply a correction to the magnitude of contributions during post processing. This could be mitigated by adding time as a dimension in which to bin contributions in nadir and azimuth as they are tallied, and if the time-direction distribution is of interest, then this approach could be used. A better approach is to apply the adjustment in (74) to each contribution as it is tallied during the simulation. This avoids the error due to applying the correction to the data after binning and also corrects tallies that may not have time data retained during the simulation. The computational cost is trivial, an exponential each time a contribution is computed, so this should be the preferred approach.

Decay was not included in the results presented in this dissertation so that the scales could be read. Note that the values of current density are in units of expected neutrons per (time of energy) bin per km^2 of actual detector cross-sectional area per source neutron (without neutron decay). Thus, in addition to the parameters investigated here, the probability of detection of the source by an actual system would depend on the detector size and efficiency, presumably as

82

functions of nadir cosine and azimuth, and upon the total number of neutrons emitted by the source. Therefore, detection limits can be applied to the plots only by a user with an application that specifies these details, or one who postulates these details in conducting design studies for a new system.

IX. Influence of Special Features of the Air-to-Space Problem

The influence of the special features of the problem vary greatly with the conditions of the transport problem posed. It is not possible to globally describe these effects. The examples presented here are restricted to detectors in geostationary orbits (stationary in the ECEF frame) and stationary detectors (meaning stationary in the ECI frame) at geostationary altitude. The locations of the source and detector at the instant of emission that are presented were selected for their convenience, importance, or to illustrate interesting features of the problem and research findings.

Before discussing the influences of relative motions and of gravity separately, a point about omitting them both is in order: A Monte Carlo code that has not been modified to include gravity and relative motion will simulate the motion of neutrons to the detector at energies so low that gravity would prevent them from climbing to the rendezvous point. The output of such a code is, of course, misleading. In order to demonstrate this shortcoming, the HATS-n code mimics this behavior when gravity is turned off. Thus, the results shown in the no-gravity curves of many plots include these unphysical results.

Relative Motions (without Gravity)

The Rendezvous Problem (without Gravity)

Motion of the detector during the rendezvous problem introduces changes in the time-energy and direction distributions as seen by the detector. This is initially illustrated with an example of a neutron source with the detector directly overhead at time of emission (source on the equator and $\Delta\alpha = 0$). Detector motion adds the possibility that availability of line of sight to the detector may change during the time scale of the problem, or even during the time of flight to the detector. That is to say, the earth may block the trajectory of neutrons with energies in some range, but not for neutrons of other energies. This cannot happen if detector motion is not included in a code. Without gravity, two cases arise. First, the *rising* detector: the detector is below the horizon at the time of emission and comes into sight during the time of flight. Second, the *setting* detector: the detector is in view at the time of emission and drops below the horizon during the time of flight..

Overhead Detector (without Gravity)

Initially consider the flight of a neutron, neglecting gravity, from a stationary equatorial emission point at 50 km altitude to a detector in geostationary orbit directly overhead ($\Delta\alpha = 0°$) at the time of emission. Allow the emission energy of the neutron cover the range of 20 MeV down to the

minimum energy to reach geostationary altitude in the presence of gravity: This depends on the starting altitude, ranging from approximately 0.56 eV from the surface of the earth to 0.47 eV from 1,000 km altitude. The range of times of flight over this energy domain is plotted in Figure 13 for an emission point at 50 km above the surface of the earth. The difference in times of flight is not visible between the fixed and moving detector cases on this scale (the orange curve overlays the blue one). Therefore, the SRD between them is plotted in gray. It exceeds one percent at the lowest energies.

Figure 13: Emission energy as a function of time of flight from an equatorial source at 50 km to a detector at $\Delta\alpha = 0°$ at time of emission with and without detector motion.

The arrival energy of neutrons as seen by the detector is plotted in Figure 14 as a function of emission energy and Figure 15 as a function of time of flight. In this case (stationary versus geostationary detector, without gravity), the

change in arrival energy varies exclusively due to motion of the detector at intercept. Because the neutron is always moving almost entirely upward (radially) in this case, and the satellite has no radial velocity, the energy of the neutron in the detector's rest frame at arrival is higher in the case of the moving detector. The difference is greatest, approaching 10%, at longer times of flight where neutron kinetic energy is lower and thus the satellite kinetic energy contributes a larger fraction to the total arrival energy. Figure 16 takes just the portion of Figure 15 at long times of flight to show the effect more clearly: The relative difference in arrival energy increases for longer times of flight.

Figure 14: Arrival energy as a function of emission energy from an equatorial source at 50 km to a detector at $\Delta\alpha = 0°$ at time of emission with (orange) and without (blue) detector motion.
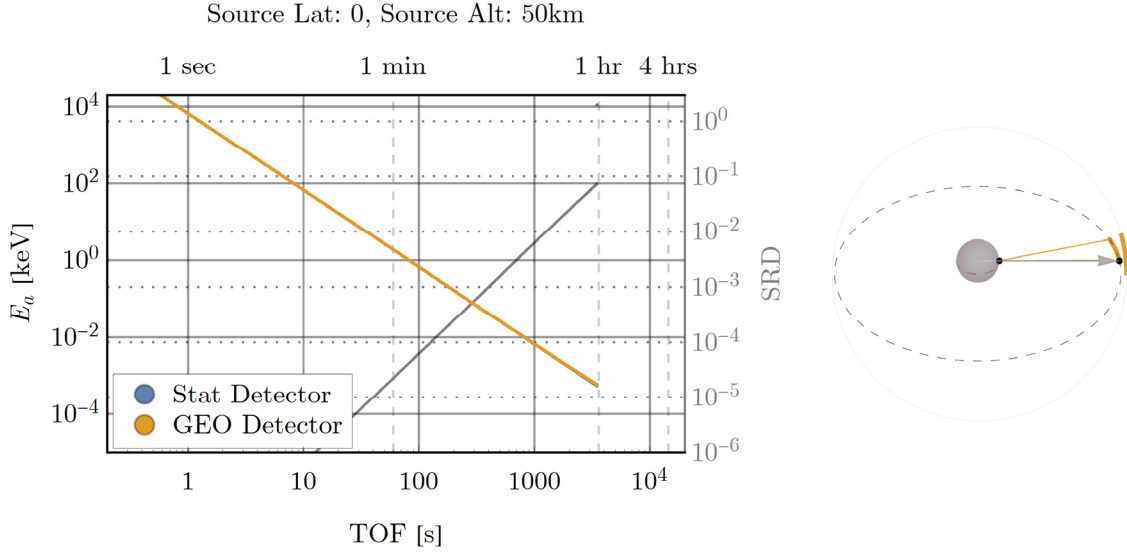
Figure 15: Arrival energy as a function of time of flight from an equatorial source at 50 km to a detector at $\Delta\alpha = 0°$ at time of emission with (orange) and without (blue) detector motion.
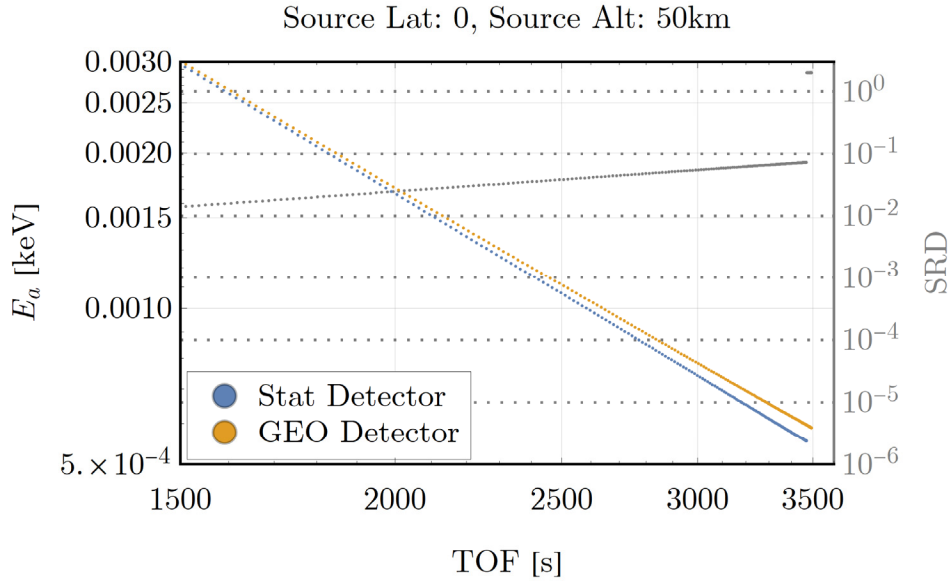
Figure 16: Detail view at long times of flight of arrival energy as a function of time of flight from an equatorial source at 50 km to a detector at $\Delta\alpha = 0°$ at time of emission with (orange) and without (blue) detector motion.

This effect is also visible in the time-energy output from HATS-n. Figure 17 shows the expectation value, in intercepted neutron current density per source neutron, as seen by overhead stationary and geostationary detectors from an equatorial neutron source at 50 km altitude. The time-energy position view (lower left) shows a pronounced bend to the right at low energy and late time. The beginning of this bend is the difference in arrival energy from the previous discussion and Figure 16. The extended pronounced hook at the end of the geosynchronous time-energy position plot would be visible in the first-flight analysis if longer times of flight and lower emission energies were considered, but these lower energies are not sufficient for a neutron to reach geosynchronous altitude. This is further illustrated by comparing the orbital segments reached by the first-flight and HATS-n outputs (right side of Figure 15 and lower right plot in Figure 17): The HATS-n output includes intercepts covering a much longer segment of the orbit despite these intercepts being physically impossible.

89
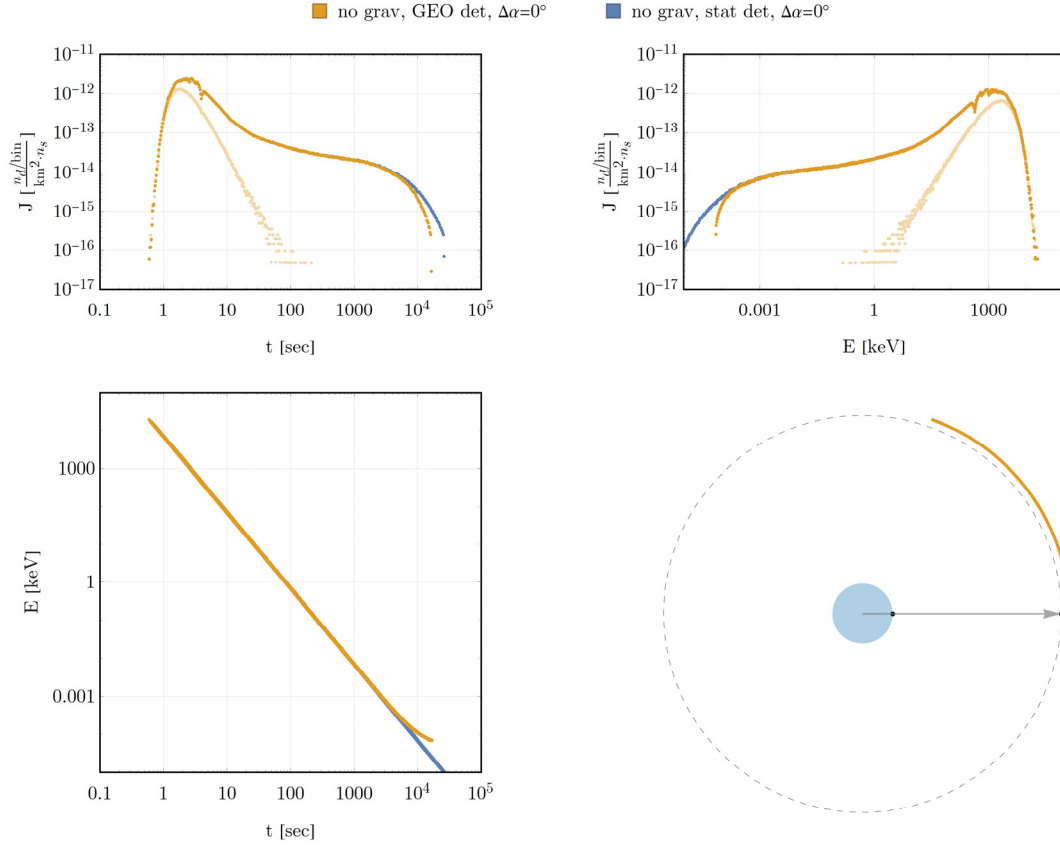
Figure 17: Intercepted neutron current density as a function of time-energy computed by HATS-n for an equatorial Watt-fission-235 neutron source at 50 km as seen by stationary and geostationary detectors at $\Delta\alpha = 0°$ at time of emission.

Arrival nadir cosine for this detector orientation is shown in Figure 18. For long times of flight the difference in nadir cosine is approximately 3%. This is confirmed in the nadir-azimuth output from HATS-n, shown in Figure 19. Note that for the equatorial source location, the first-flight contributions should not (and are not) distributed in azimuth angle. However, the scattered contributions come from interactions geometrically separate from the source (hence non-equatorial) and thus spread the contributions in azimuth. On this scale, the

90

scattered contributions largely obscure the view of the direct contributions in the nadir-azimuth plots.

The decrease in nadir cosine from the first-flight analysis can be seen in the HATS-n plot of nadir cosine in cosine values from approximately 0.97 to 1. As with the time-energy output from HATS-n, the effect is extended to nadir cosines less than 0.7 by neutron intercepts with less than the minimum energy to reach the satellite. If neutrons with less than the minimum energy to reach the detector are excluded from the estimate, the HATS-n nadir cosine plot would be truncated to match the first flight analysis. Also, the large tail for the geosynchronous detector in the polar nadir-azimuth plot in the lower part of Figure 19 would be trimmed. However, it is worth noting that even by excluding the trajectories without the minimum energy to reach the satellite, the tail on the nadir-azimuth plot still extends outside the view of the earth as seen by the detector. In this case, the contributions with longer times of flight have an apparent nadir angle at arrival up to approximately 14 degrees, while the earth covers nadir angles less than 10 degrees. From the point of view of the detector, these neutrons arrive from a source geometrically separate from the earth. (A detector perfectly collimated to see only the earth would not detect these neutrons.) As the source moves out of the equatorial plane, a greater fraction of nadir-azimuth bins with contributions fall outside the view of the earth as seen by the satellite. Figure 20 shows the nadir-azimuth plots from HATS-n for the

same source at 45ºN. Note the distribution of observed neutrons arriving from directions outside the detector view of the earth.
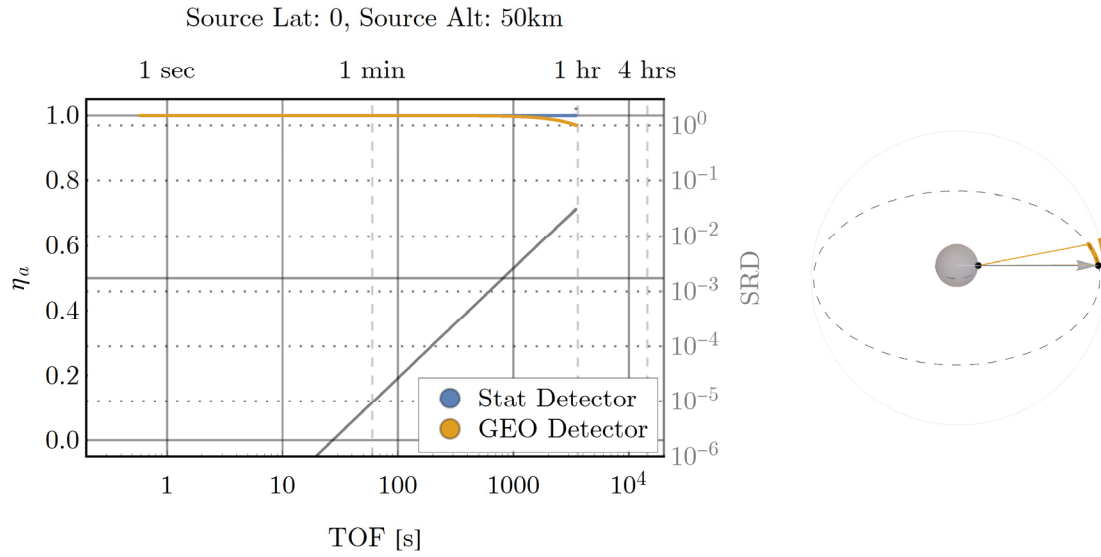
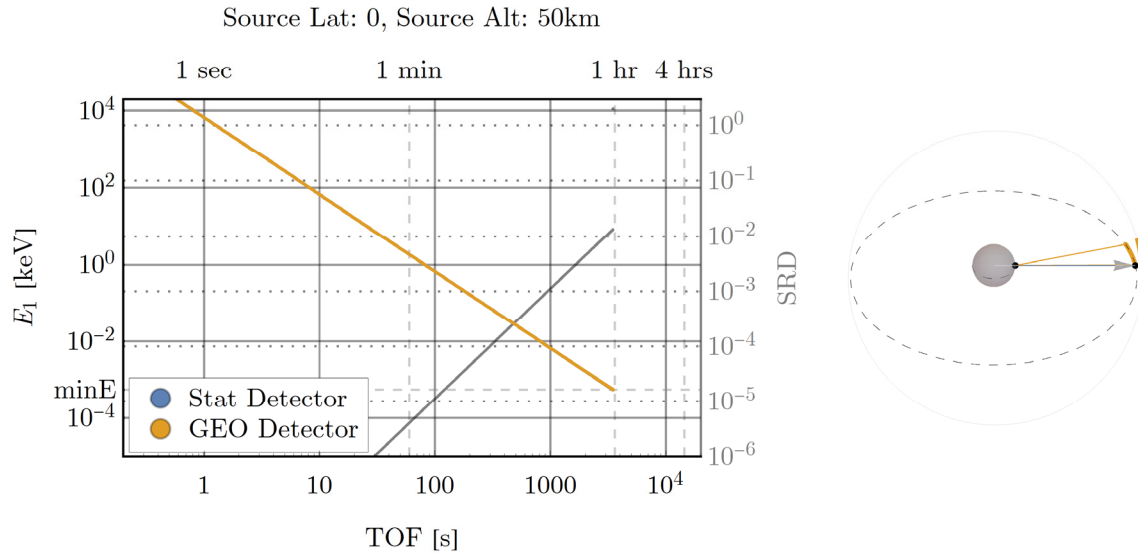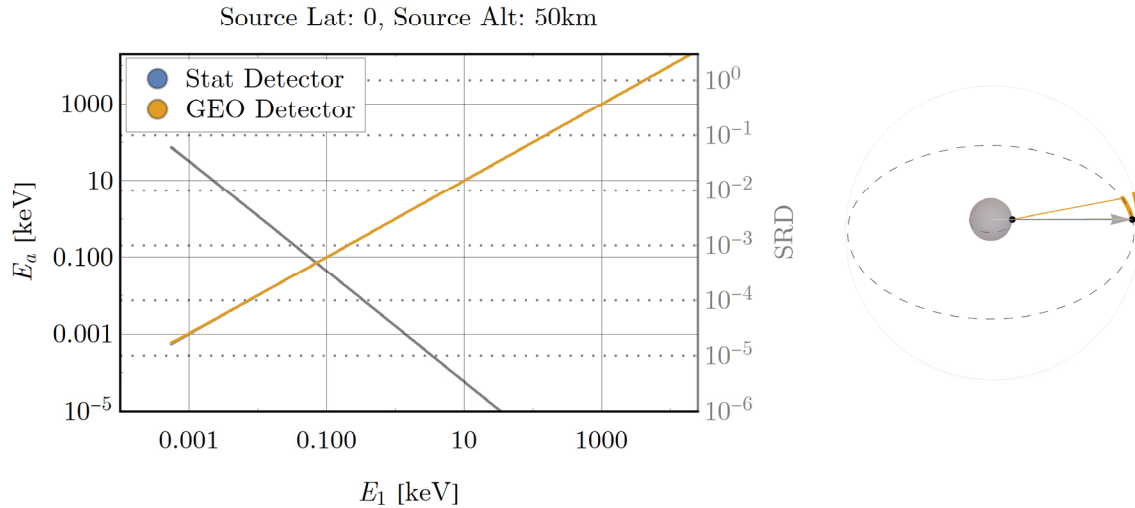**Figure 18: Arrival nadir cosine as a function of time of flight from an equatorial source at 50 km to a detector at $\Delta\alpha = 0°$ at time of emission with and without detector motion.**
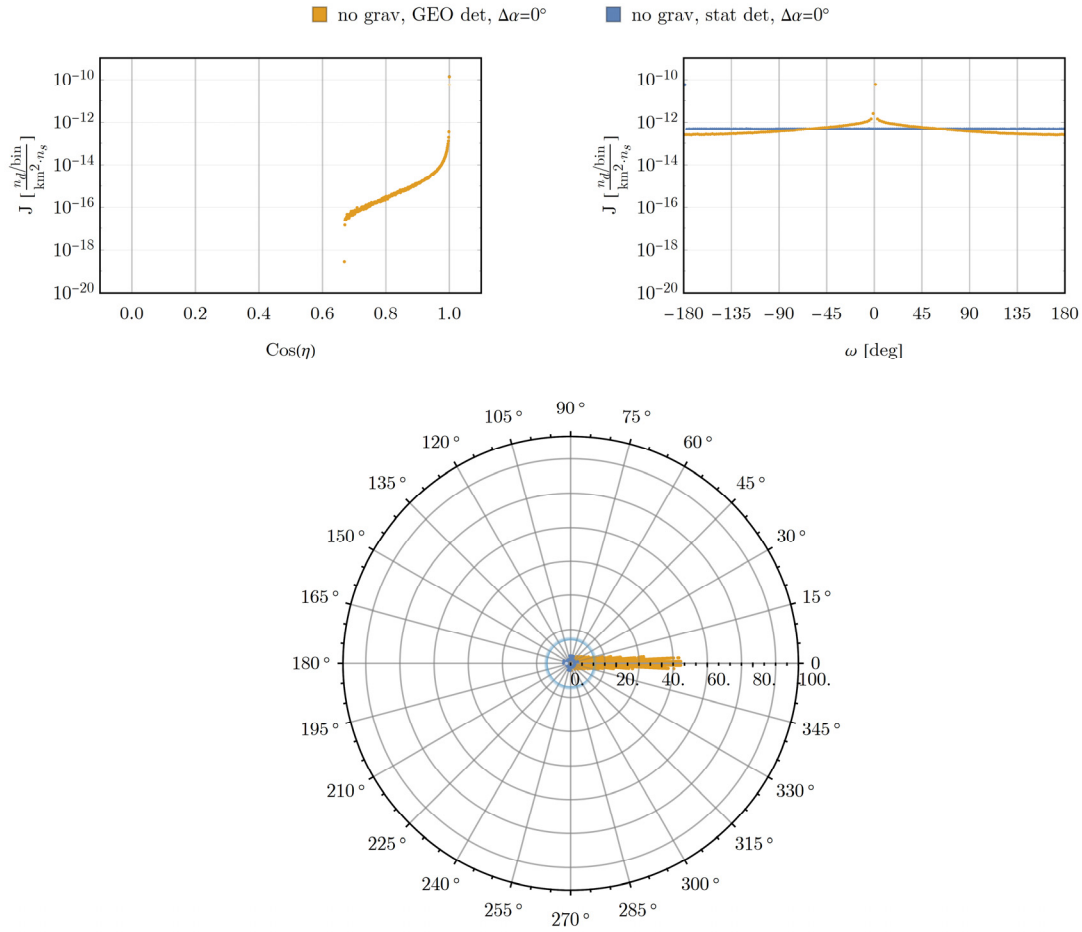
**Figure 19:** **Intercepted neutron current density as a function of nadir-azimuth computed by HATS-n for an equatorial Watt-fission-235 neutron source at 50 km as seen by stationary and geostationary detectors at** $\Delta\alpha = 0°$ **at time of emission.**
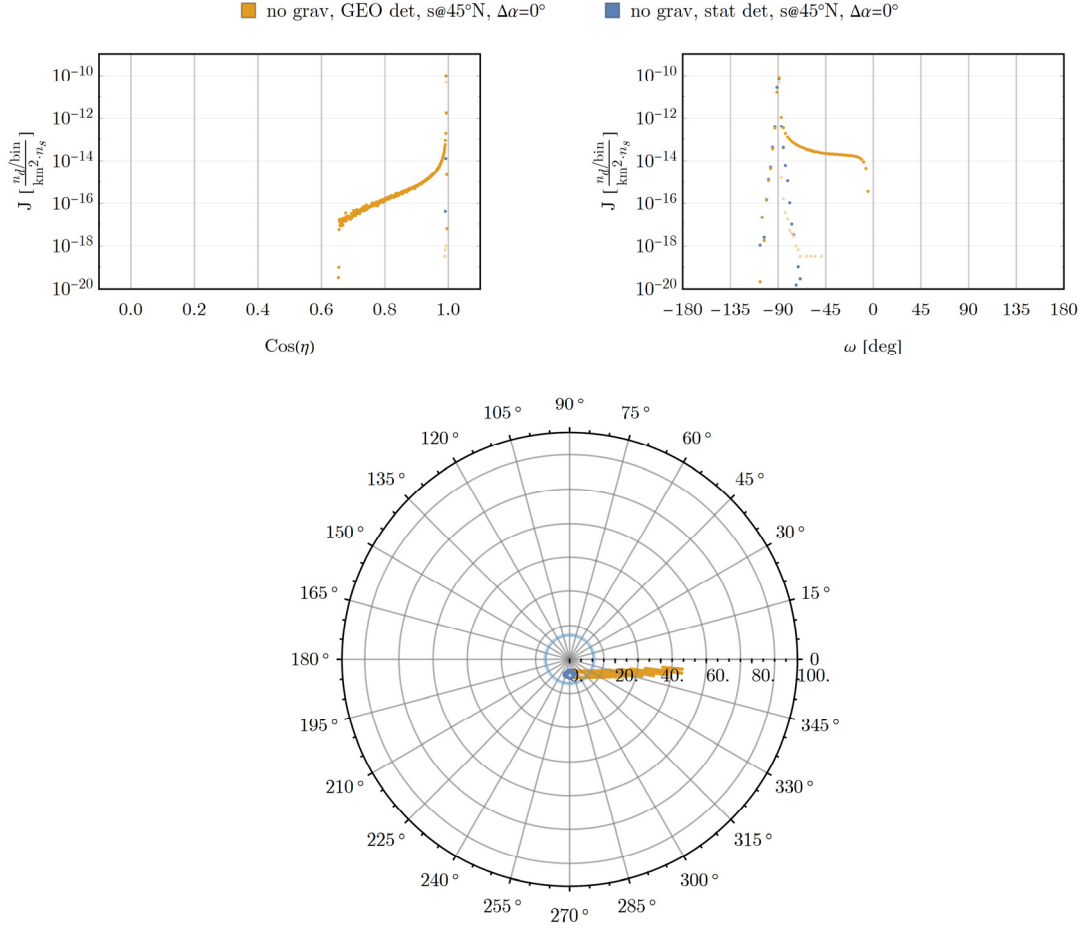
Figure 20: **Intercepted neutron current density as a function of nadir-azimuth computed by HATS-n for a Watt-fission-235 neutron source at 50 km and 45ºN as seen by stationary and geostationary detectors at** $\Delta\alpha = 0°$ **at time of emission.**

Rising Detector (without Gravity)

For the rising detector, with $\Delta\alpha = -92°$, when motion of the detector and gravity are neglected, no rendezvous is possible for first-flight neutrons, regardless of neutron energy, because the stationary detector remains below the horizon for the entire time scale of the problem. The only neutrons that reach the detector are those that undergo a chain of scatters in the atmosphere which brings the neutron to a location where line of sight to the detector becomes available. With

motion of the detector, the detector rises into view (in the ECI frame) during the time of flight as shown in Figure 21. The domain of emission energies reaching the detector and the corresponding range in times of flight are limited. The only intercepts that can occur are ones with sufficiently long times of flight for the detector to come into view during the time of flight.

Figure 21: **Emission energy as a function of time of flight from a source at 50 km and 45ºN to a detector at $\Delta\alpha = -92°$ and rising at time of emission with and without detector motion.**

95

Figure 22: **Arrival energy as a function of time of flight from a source at 50 km and 45ºN to a detector at $\Delta\alpha = -92°$ and rising at time of emission with and without detector motion.**

Figure 23 shows the results from HATS-n for the same rising detector transport problem. As expected from the first-flight analysis, no contributions result from direct flight from the source to a stationary detector. Unfortunately, in the one million histories run to generate the figure, no first-flight contributions were tallied in the case of the geosynchronous detector either. The energy threshold below which the time of flight is long enough for the detector to come into view makes first-flight contributions rare in the context of this problem. Neutrons with energy less than 10 eV can make the intercept, but the probability of sampling such a low neutron energy at the source from the Watt-fission-235 distribution (equations (2) and (3), and Figure 7) in HATS-n is approximately 1.4×10^{-8}. In 10^6 histories, it is unlikely a neutron with low enough energy will be sampled. Fortunately for this discussion, the scattered contributions computed by

96

HATS-n form a large population (approximately 2×10^8) of neutrons scattered down in energy. Approximately 25% of these scattering interactions resulted in next-event contribution tallies at the detector. Recognizing that the scattering interactions generating these contributions occur at relatively close geometric proximity to the source, the first-flight analysis can still be qualitatively compared to the scattered result from HATS-n.

The HATS-n plots of intercepted neutron current density integrated in time and energy (top of Figure 23) match the expected time of flight and arrival energies from the first-flight analysis in Figure 22, although the orbit segments do not agree. As seen in the overhead case, the extension of the orbit segment during which contributions arrive reported by HATS-n is primarily a result of scattered neutrons with less than the minimum energy to reach geostationary altitude. However, in this case, the early time of flight segment on the orbit, which should have no contributions according to the first-flight analysis, is also reported as having contributions by HATS-n. This is due to inclusion of the scattered contributions and the fact that the orbit segments do not include information on the intensity of the intercepted neutron current density being reported. The short times of flight are a result of fast neutrons that were emitted in the direction of the detector such that the detector came into view much earlier than for neutrons emitted at the source. These are rare events, and have correspondingly small contributions (tens to hundreds of orders of magnitude

below the scale of the integrated time and energy HATS-n plots), but they cause the plotting routine to highlight the orbit segment over which they arrive.
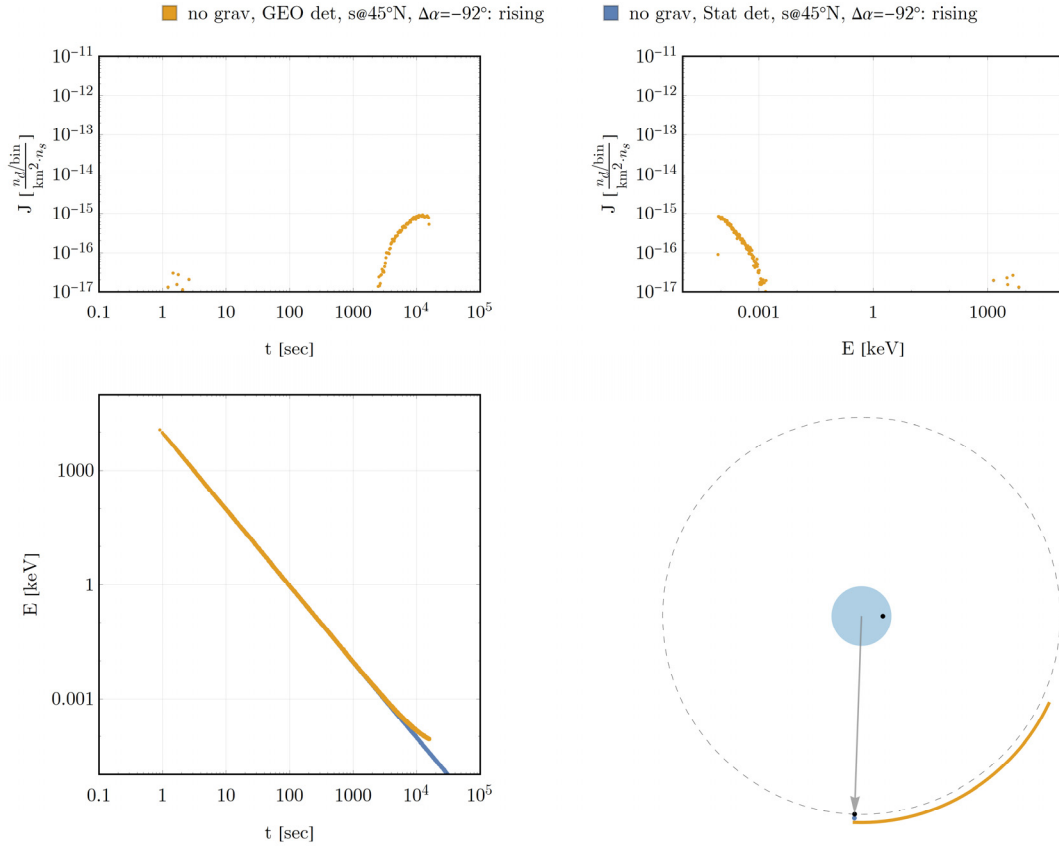
Figure 23: Intercepted neutron current density as a function of time-energy computed by HATS-n for a Watt-fission-235 neutron source at 50 km and 45ºN as seen by stationary and geostationary detectors at $\Delta\alpha = -92°$ and rising at time of emission.

Setting Detector (without Gravity)

The case of a setting detector, $\Delta\alpha = 83°$, is shown in Figure 24. Here, for the full range of emission energies considered, it is possible for the neutron to intercept the satellite when motion of the detector is neglected because the stationary detector never falls out of view. With detector motion, neutrons

emitted with energy below some threshold have a time of flight to the detector during which the detector falls out of view. Neutrons with energy below this threshold cannot intercept the detector.
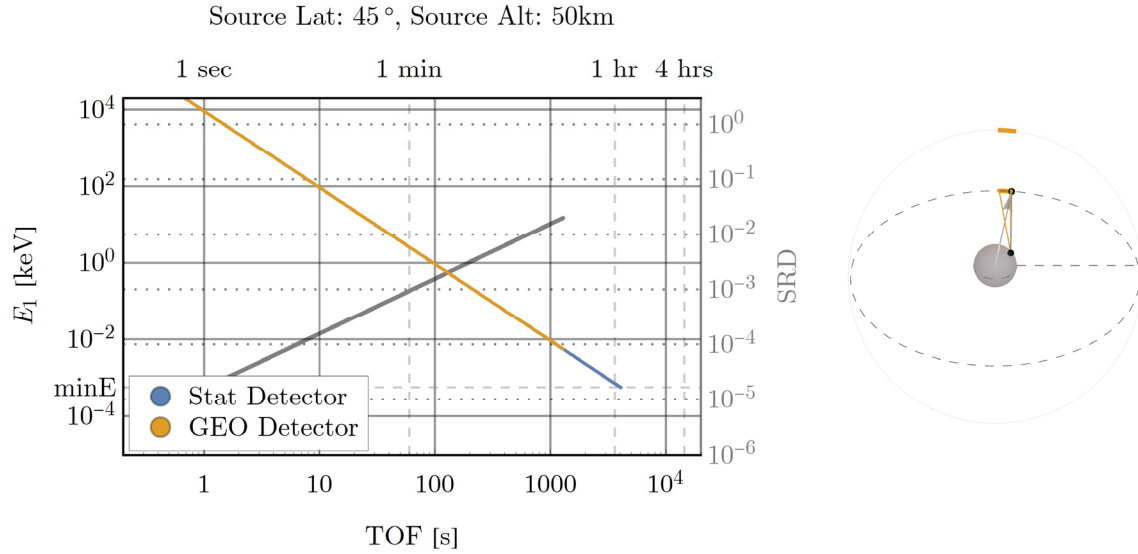

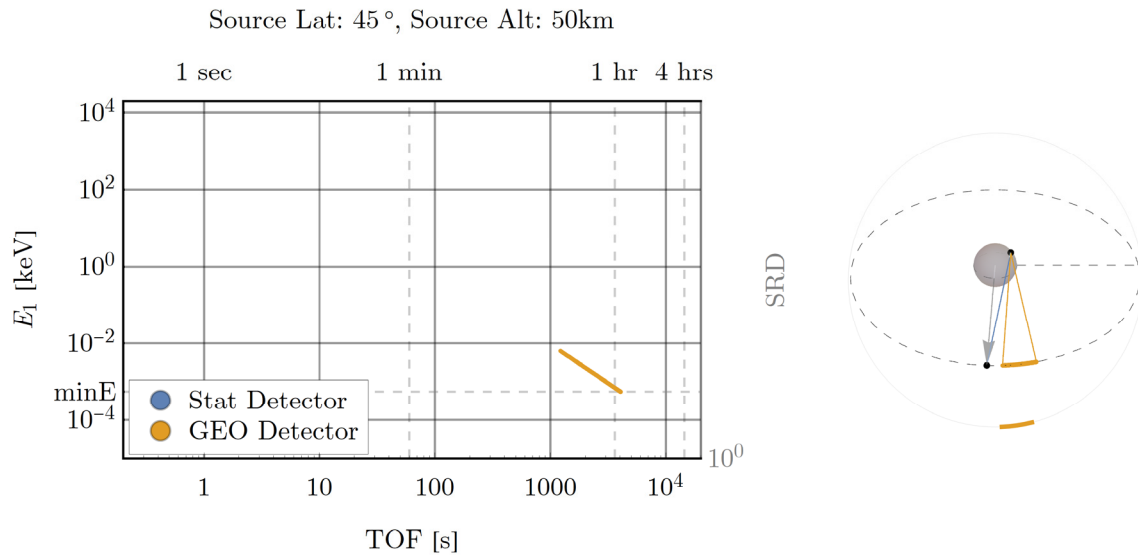**Figure 24: Emission energy as a function of time of flight from a source at 50 km and 45ºN to a detector at $\Delta \alpha = 83°$ and setting at time of emission with and without detector motion.**
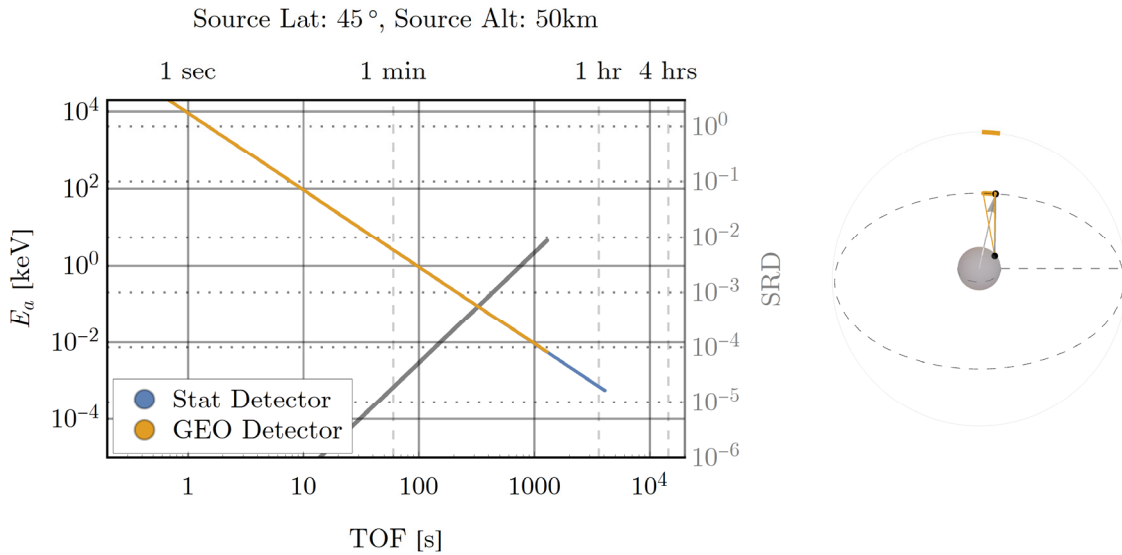
Figure 25: Arrival energy as a function of time of flight from a source at 50 km and 45ºN to a detector at $\Delta \alpha = 83°$ and setting at time of emission with and without detector motion.
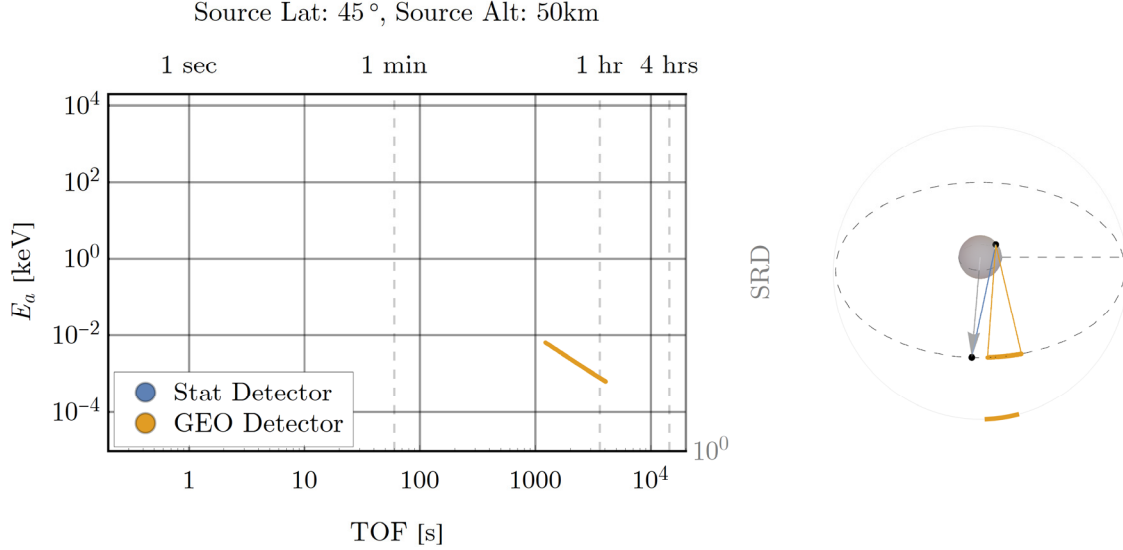
Figure 26 shows the results from HATS-n for the same setting detector transport problem. The HATS-n output does report first flight contributions for both the stationary and geostationary deters as expected from the first-flight analysis, but the intensity of the tallied contributions is very low due to the long optical thickness through the atmosphere to fly directly to the detector. The scattered contribution has much higher intensity due to scatters in locations with a lower optical thickness to the detector. So, as with the rising detector, the scattered contributions from HATS-n will be qualitatively compared to the first-flight analysis.

The HATS-n plots of intercepted neutron current density integrated in time and energy (top of Figure 26) match the expected time of flight and arrival energies from the first-flight analysis in Figure 25, although the orbit segments do not agree. In this case, the long time of flight extension of the orbit segment during which contributions arrive reported by HATS-n is primarily a result of neutrons scattering in the atmosphere along paths that follow the detector over the horizon. These histories retain line of sight to the detector longer than neutrons emitted at the source.
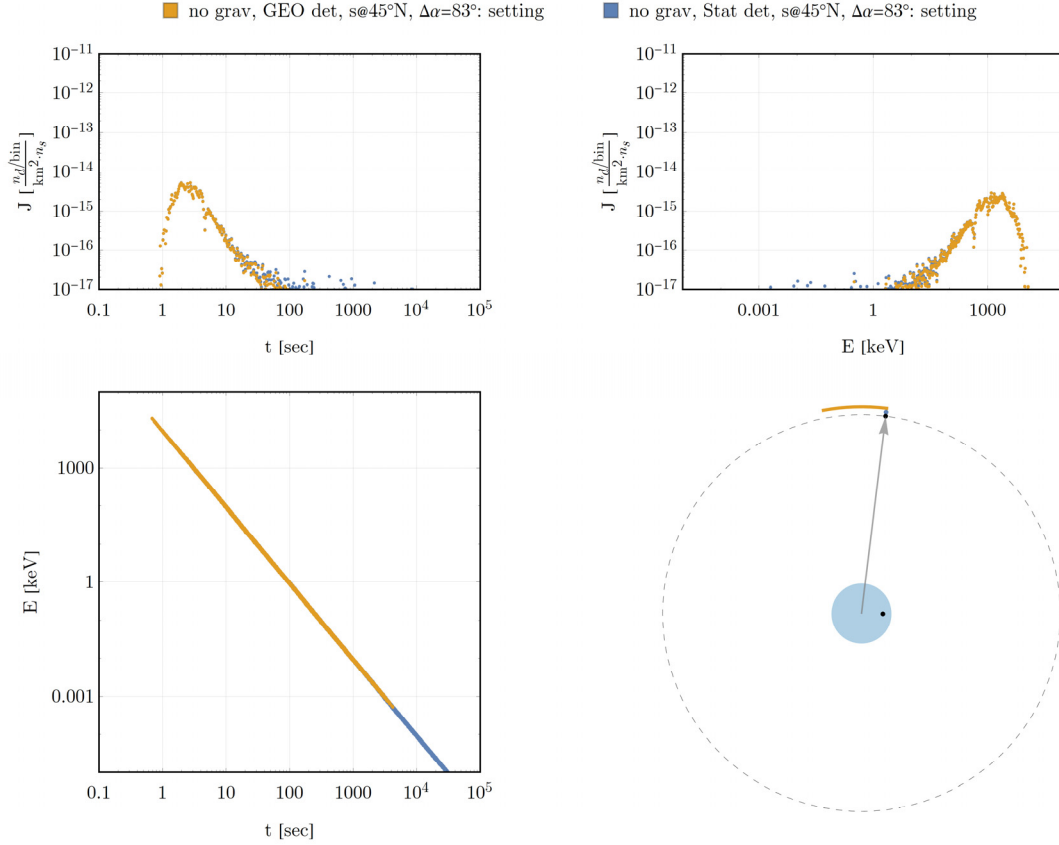
Figure 26: Intercepted neutron current density as a function of time-energy computed by HATS-n for a Watt-fission-235 neutron source at 50 km and 45ºN as seen by stationary and geostationary detectors at $\Delta\alpha = 83°$ and setting at time of emission.

Divergence Factor (without Gravity)

Consider a neutron source at 50 km and 45ºN. At the moment of neutron emission, the detector is in view to the west, for example, with $\Delta\alpha = -45°$. This is the *ascending* detector geometry. The divergence factor for neutrons intercepting an ascending geostationary detector with and without detector motion is shown in Figure 27. In this geometry, the divergence factor with detector motion is globally greater (meaning less divergence and higher intensity of contributions) than the divergence factor without detector motion. This can be

attributed to two features of this geometry: First, recognize that the point of closest approach between the source and the detector occurs at $\Delta\alpha = 0$. In the ascending geometry the source and detector are closing with one another as time of flight increases, decreasing the radius, hence area, of the neutron locus and reducing divergence. Second, for longer times of flight, the kinetic energy, hence magnitude of velocity, of the neutron is smaller relative to the velocity of the detector. As neutrons approach the detector traveling vertically or nearly vertically (as they always do when traveling on a straight trajectory to intercept) the incident direction is always nearly perpendicular. When the velocity of the detector is large compared to the velocity of the neutron, the effective area of the detector becomes large resulting in less divergence.
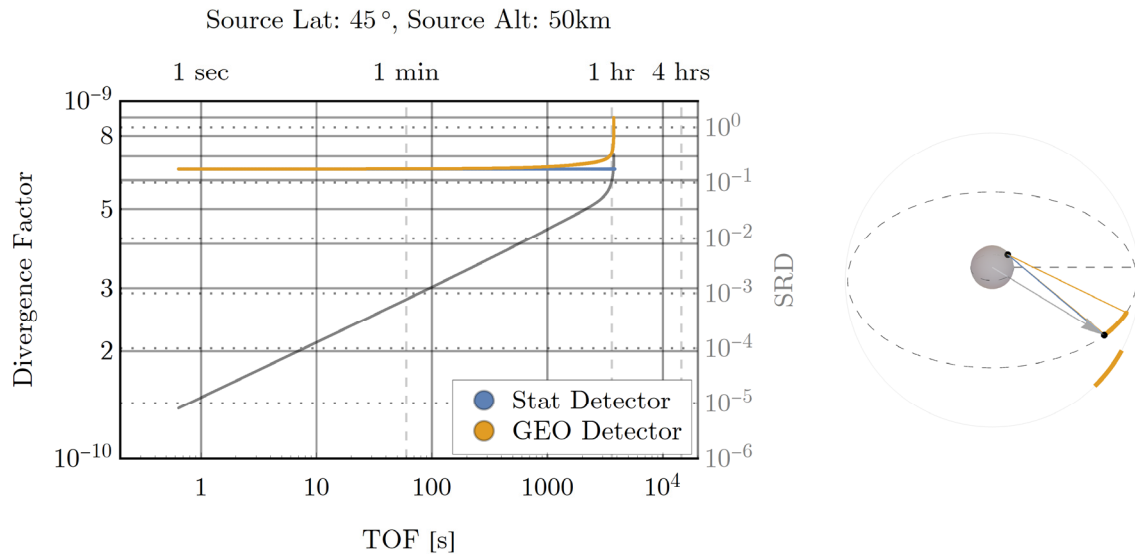
Figure 27: Divergence factor as a function of time of flight from a source at 50 km and 45ºN to an ascending detector with and without detector motion.

The same features of the geometry affect the divergence factor in the case of a *descending* detector geometry in which the detector is visible to the east from the source, with $\Delta\alpha = +45°$, and descending towards the horizon as shown in Figure 28. In this case, the two factors compete. First, the distance between the source and detector is increasing with increasing time of flight resulting in a larger radius, hence lager area, of the neutron locus (tending to increase divergence and decrease the divergence factor). And second, the neutron speed to the rendezvous decreases with increasing time of flight so the relative velocity is rotating toward that of the detector while, geometrically, the normal direction to the locus is rotating toward the direction of motion of the detector. Thus, the effective area of the detector is increasing due to detector motion increases. The dip in the divergence factor at about 2000 seconds occurs because the first factor dominates for flight times less than about 1500 seconds. The dip in the SRD at about 2000 seconds occurs as the divergence factor increases through its value for the stationary detector, which would be the divergence at infinite energy.
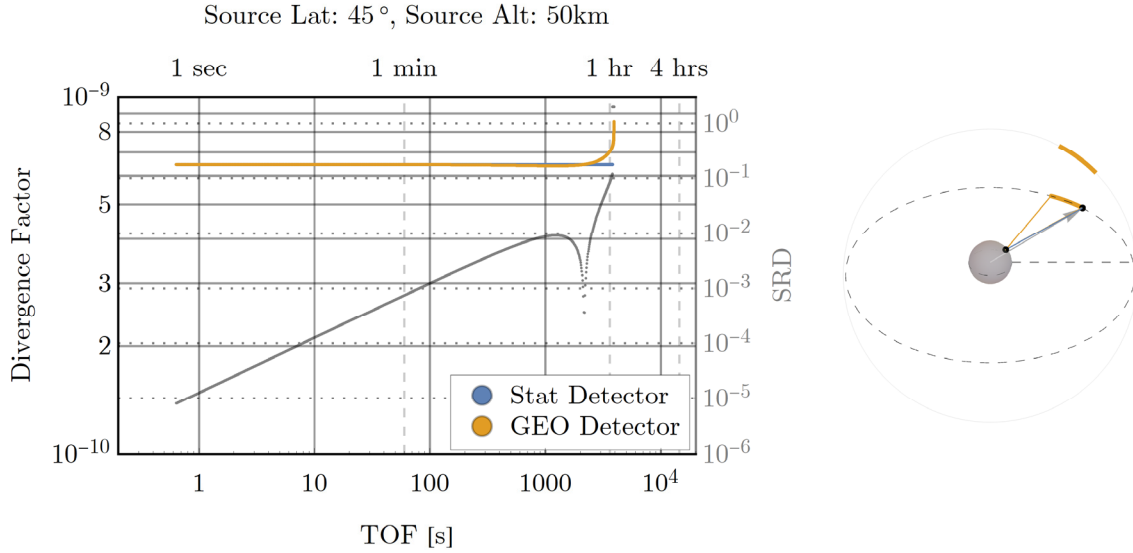
Figure 28: **Divergence factor as a function of time of flight from a source at 50 km and 45ºN to a descending detector with and without detector motion.**

Optical Thickness Through the Atmosphere (without Gravity)

Consider the first-flight neutrons: Without gravity and without relative motions, the speed along the path decreases for longer times of flight, but the path does not move. It is the straight line between the emission point and the detector. The optical thickness changes only due to the change in cross section of the air, which is a function of neutron energy.

Without gravity, relative motion changes the path through the atmosphere (as well as changing the speed along the path). The path to the rendezvous changes in zenith angle and heading in a way that depends on the latitude of the source point.

1. Decreasing the zenith angle, i.e. increasing ζ, decreases the geometric length of the path, tending to decrease the optical thickness.

2. Decreasing the zenith angle changes the relative speed in the air frame of reference in way that depends upon the heading of the path and the speed of the neutron. This changes the rotating-earth correction factor and hence the optical thickness.

3. Changing the heading changes the rotating-earth correction factor in a way that depends on zenith angle and speed, changing the optical thickness.

The optical thickness for scattered neutrons is also subject to these effects, which are dependent upon the location of the scatter. Additionally, for a given energy and satellite location, the optical thickness varies with the scatter location, which also changes the zenith angle and heading.

Effective Path Length to Rendezvous (without Gravity)

The EPL through the atmosphere to a setting geostationary detector ($\Delta \alpha = 83°$) from an emission point at 50 km altitude and 45°N is shown in Figure 29. As time of flight increases, the EPL to intercept increases and reaches a maximum at the last possible intercept after which the detector drops below the horizon and out of line of sight. Compare this to the constant EPL for the stationary detector. The required emission zenith cosine to make this continuum of intercepts is shown in Figure 30. The entire range of intercepts is achieved with downward emission directions, aiming further downward as the detector approaches the horizon. The value of emission zenith cosine for the final (longest)

time of flight corresponds to a path through the atmosphere beginning at the emission point traveling downward to grazing incidence at the surface of the earth and then back upwards through the full thickness of the atmosphere and to the detector.
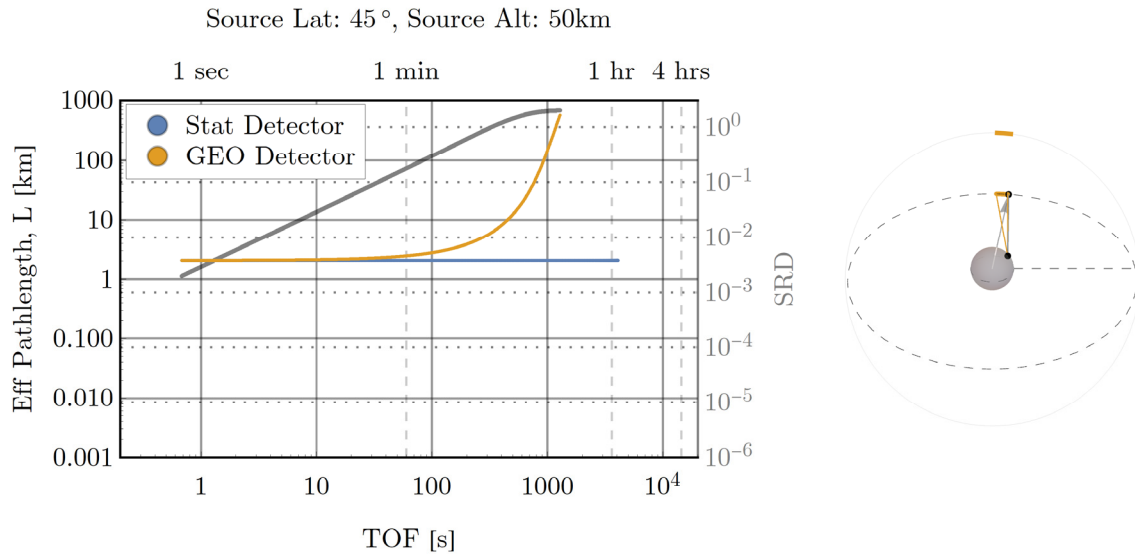
Figure 29: **Effective path length as a function of time of flight from a source at 50 km and 45ºN to a detector at $\Delta\alpha = 83°$ and setting at time of emission with and without detector motion.**
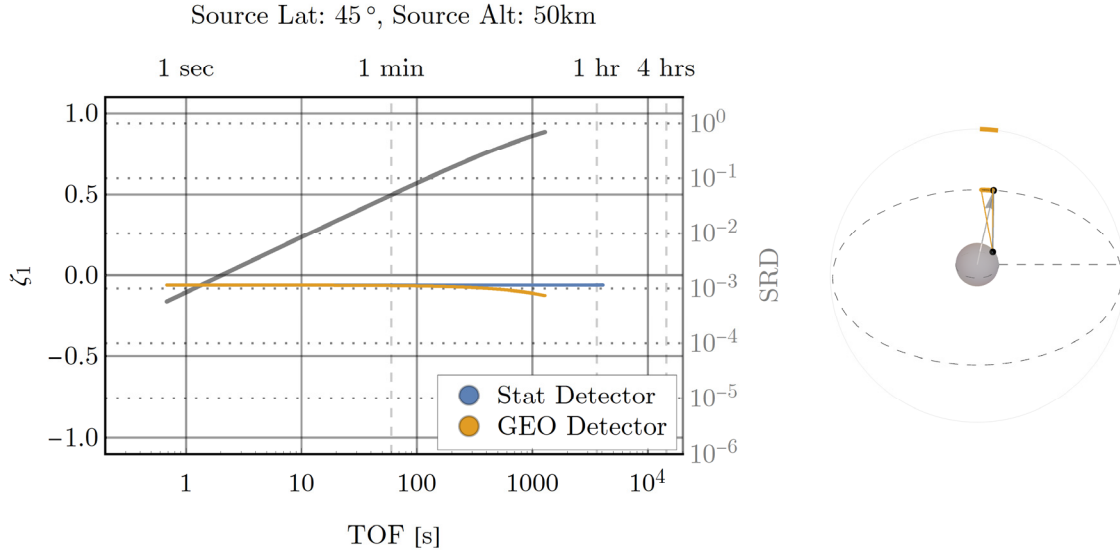
Figure 30: Emission zenith cosine as a function of time of flight from a source at 50 km and 45ºN to a detector at $\Delta\alpha = 83°$ and setting at time of emission with and without detector motion.

Rotation of the Earth

As a neutron traverses a path in the atmosphere, the atmosphere rotates eastward in the ECI frame, but the path of the neutron is stationary in the ECI frame. As the atmosphere sweeps across the path of the neutron, the EPL may be lengthened or shortened depending on the relative magnitude and direction of the neutron and atmosphere velocities. This effect is greatest for horizontal paths traveling due east and due west at the equator. Figure 31 shows the EPL for a horizontal path at 45ºN and at the equator (dashed) traveling east and west through the full thickness of the atmosphere. For neutrons above 10 eV, the influence is small (less than one percent). However, below this energy the motion of the atmosphere can have a profound effect on the effective path length.

107

This is mitigated, somewhat, by the fact that at energies below 10 eV, the total interaction cross section for the atmosphere is proportional to $1/v$ and regardless of the effective path length most paths are optically thick. This feature of the problem causes a systematic asymmetry in the transport. Neutrons emitted westerly direction see a longer EPL than those headed northward or southward,, and thus more attenuation, through the atmosphere due to rotation of the atmosphere. As a result, these neutrons are less likely to escape the atmosphere without colliding and their geometric distance to the next interaction is shorter. On the other hand, neutrons traveling eastward will see a reduced effective path length resulting in a longer geometric distance to the next interaction in the atmosphere. From an overhead viewpoint, like an overhead detector, the shape and distribution of the scattering region in the atmosphere changes. This enhances the asymmetry between ascending and descending geometries.

It is also worth noting that for the lowest energies, the corrected path length in Figure 31 shows negative path lengths for the eastbound equatorial case. While a negative path length is not strictly physical (distance backward is still distance), this indicates the situation in which the atmosphere sweeps past the path of the neutron faster than the neutron traverses the path. The result is still a positive computed path length, but it is left negative for this plot to illustrate the point.

108
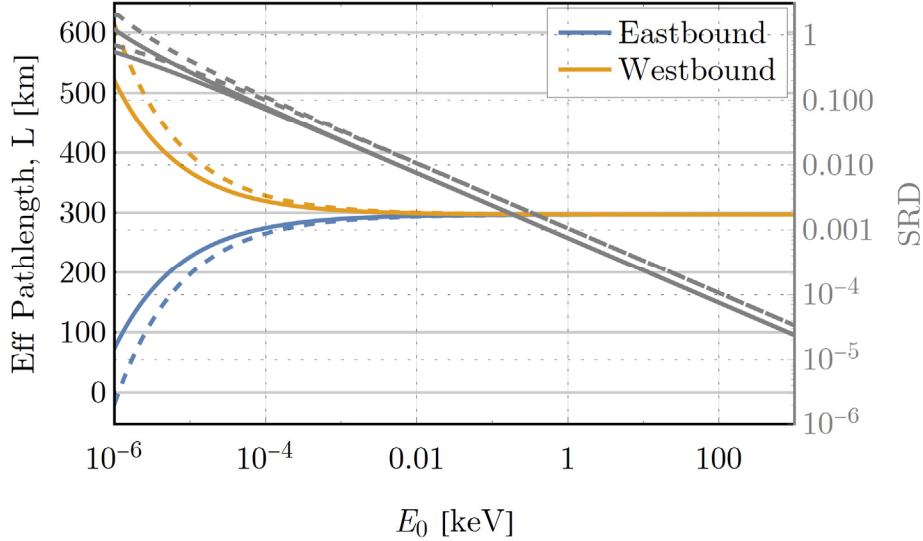
Figure 31: Effective path length including rotation of the atmosphere for east and west horizontal paths at the equator (Dashed) and 45°N (Solid).

Motion of the Scattering Medium

The influence of Doppler-broadened cross sections on the fidelity of the atmosphere model was evaluated by comparing the pointwise total cross section as tabulated in ENDF (unbroadened, 0 K) to cross sections broadened to room temperature (300 K) and the maximum temperature in the USSA-76 atmosphere model (1000 K). Overall, the influence was small for the atmospheric constituents used. For energies above 0.5 eV, the maximum SRD was less than 0.01 (approximately 1%) for the total cross section of the atmosphere broadened for 300 K and 1000 K. Below 0.5 eV, the difference is larger, climbing to a SRD of 1 for the lowest energies (10^{-8} keV). This is mitigated by the fact that over this range the total cross section for the atmosphere is proportional to $1/v$ so the atmosphere is already optically thick. The total cross section increases due to

broadening in this energy range, but the effect is that an optically thick atmosphere simply becomes thicker. Recalling the sensitivity of probability of escape from Figure 12 at this energy, for most effective path lengths, the probability of escape for neutrons with kinetic energy 0.5 eV and below is already fairly low. Additionally, neutrons with kinetic energy less than approximately 0.5 eV (varies depending on emission altitude) are less likely to have the minimum kinetic energy required to achieve geosynchronous altitude to intercept a detector.

Motion of the Source

Including source motion in practical calculations is trivially implemented and has trivial cost. Further discussion of source motion is not necessary, except to point out that the magnitude of the source velocity (up to about 10 km/s) is similar to that of the minimum velocity required to reach Geostationary altitude, approximately 35,786 km. Thus, depending on orientation of the source velocity, the population of neutrons able to intercept an orbital target can be significantly impacted. This is especially significant for first-flight neutrons because of the rapid fall-off of the Watt source distribution at energies this low.

Gravity

In this section, detector motion is included, unless specifically stated otherwise. Results with gravity are compared to results for the same problems without gravity.

Note: I reserve *line of sight* to mean a straight line, as in common usage. With gravity, the line of sight between an emergence point and the detector can be blocked while a neutron of low-enough energy starts at a higher elevation angle that decreases along the trajectory (due to gravity) and can reach the detector without being obstructed by the earth. An unobstructed trajectory (with gravity) is referred to here as a *clear flight path*. Thus, such a neutron that has an obstructed line of sight can have a clear trajectory. This effect, together with the need for a low-enough energy cause behaviors in the results that are qualitatively dramatically different than those predicted by a code that neglects gravity, even if it includes satellite motion. For some initial differences in right ascension and source latitudes, a detector would actually be exposed to neutrons while a transport code that does not include gravity would not be so exposed. The consequences of this could be very significant.

The Rendezvous Problem

Gravity has a large influence on the rendezvous problem. In general, with the inclusion of gravity in the rendezvous problem, the range of successful intercepts given any set of starting conditions is greatly increased. The presence

of gravity also introduces three special cases worth noting: the multi-direction rendezvous case as the detector passes through the antipode, the loss and subsequent reacquisition of a clear trajectory (unobstructed by the earth) as the detector disappears over the horizon, and the case of a source above either pole. In this section, the results for various example satellite locations at the moment of emission are presented. These include examples that demonstrate these behaviors.

Overhead Detector

As when adding relative motions to the rendezvous problem, consider the flight of a neutron from a stationary source on the equator at 50 km altitude to a detector in geostationary orbit directly overhead, $\Delta\alpha = 0°$, at the time of emission. Allow the emission energy of the neutron to cover the range from 20 MeV down to the minimum energy to reach geostationary altitude, or even lower for illustration of differences when gravity is neglected. The properties of these rendezvous are compared to the corresponding rendezvous that ignore the presence of gravity (i.e. those with straight trajectories). The range of time of flight over this energy domain is plotted in Figure 32. In the figure, no-gravity rendezvous that lack sufficient energy to reach the satellite with gravity are distinguished by a lighter shading (tan as opposed to orange).
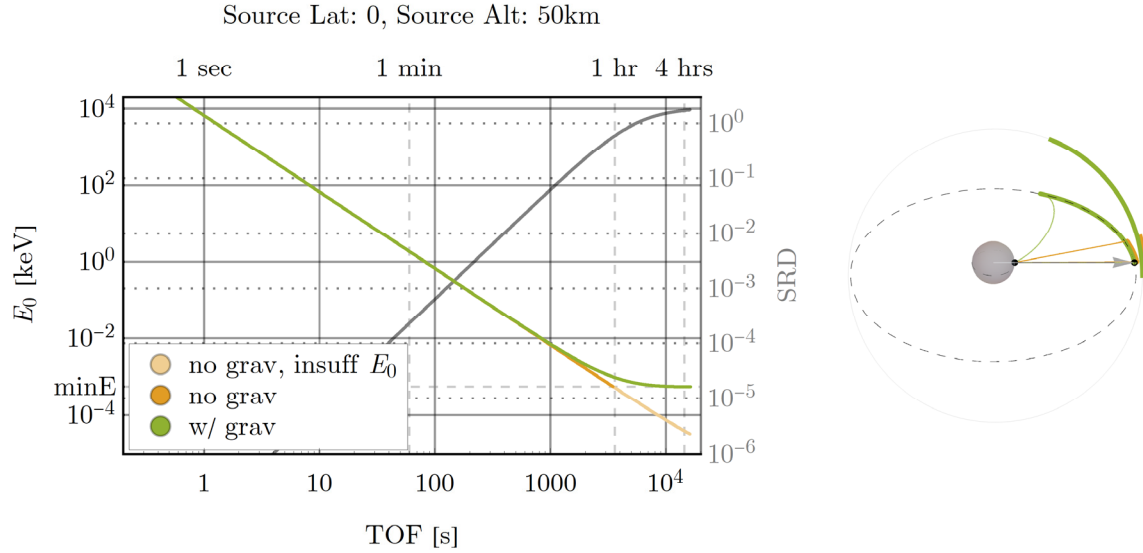
Figure 32: **Emission energy as a function of time of flight from an equatorial source at 50 km to a detector at $\Delta\alpha = 0°$ at time of emission with and without gravity.**

The arrival energy of neutrons as seen by the detector is plotted in Figure 33 as a function of emission energy and Figure 34 as a function of time of flight. In this case (intercepting a geostationary detector with and without gravity), the change in arrival energy varies due to motion of the detector at intercept *and* the change in neutron energy and direction on the flight to the detector. As the time of flight to intercept increases, the arrival energy as seen by the detector decreases significantly more for the gravitational trajectory than for the trajectory neglecting gravity. For the longest times of flight, the difference is nearly an order of magnitude.

Figure 33: Arrival energy as a function of emission energy from an equatorial source at 50 km to a detector at $\Delta\alpha = 0°$ at time of emission with and without gravity.

Figure 34: Arrival energy as a function of time of flight from an equatorial source to a detector at $\Delta\alpha = 0°$ at time of emission with and without gravity.
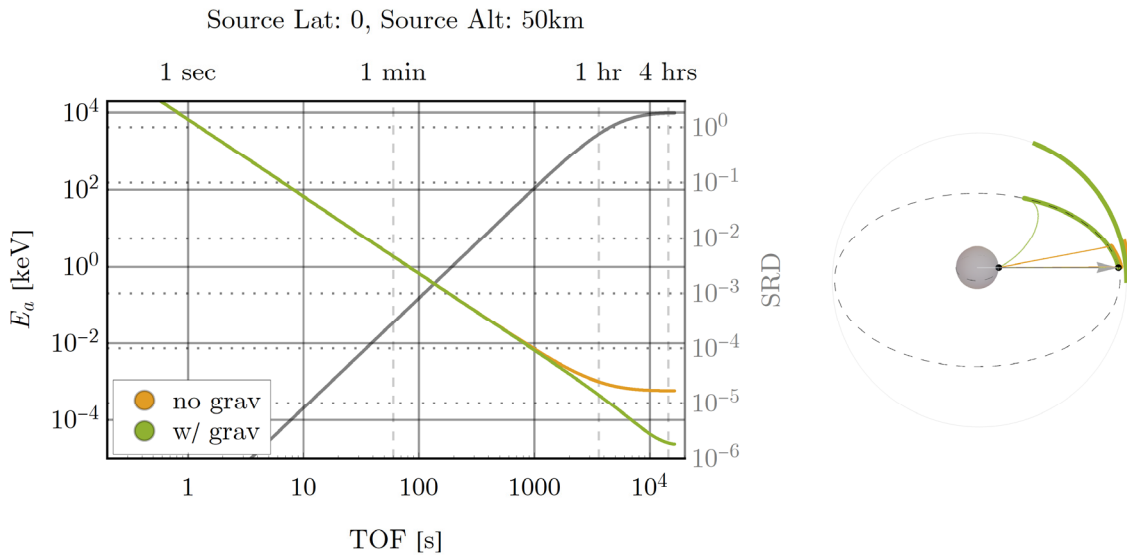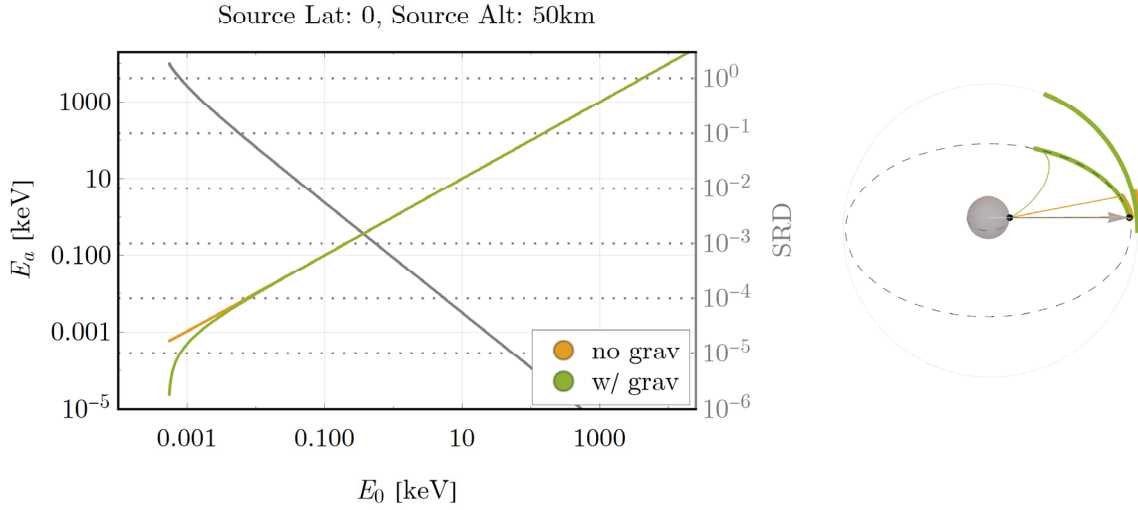
This effect is also visible in the time-energy output from HATS-n. Figure 35 shows the expected intercepted neutron current density as seen by an overhead geostationary detector from an equatorial Watt-fission-235 neutron source at 50

km with and without gravity. With gravity, the time-energy position view
(lower-left) shows a pronounced bend downward and then to the right at low
energy and late time. The time-energy position plot for contributions with and
without gravity matches the shape of the lines in Figure 34 as expected.
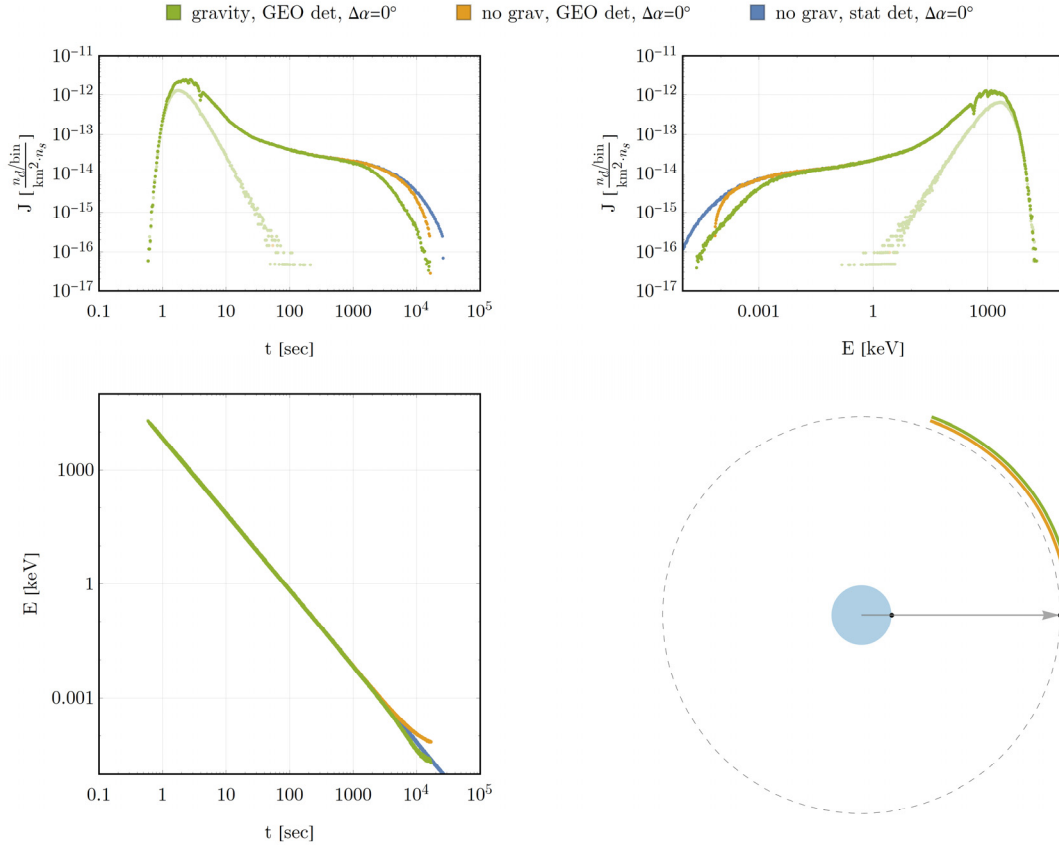
**Figure 35: Intercepted neutron current density as a function of time-energy computed by
HATS-n for an equatorial Watt-fission-235 neutron source at 50 km with and without gravity
as seen by stationary and geostationary detectors at $\Delta\alpha = 0°$ at time of emission.**

Arrival nadir cosine for the overhead case is shown in Figure 36. For long
times of flight, the difference in nadir cosine is grows rapidly. Neglecting gravity
and detector motion, neutrons in any intercept come from downward or nearly

downward directions by construction of the problem. The addition of detector motion, as shown previously, increases the range of nadirs as seen by the detector, but for the time-energy range and source-detector orientations considered, the variation in nadir was relatively small. This changes with the inclusion of gravity. Even neglecting motion of the detector, the direction of neutron motion changes as the neutron makes the flight to the detector. As the neutron climbs on an orbital trajectory, the zenith angle increases; i.e., as altitude increases, the motion of the neutron is less vertical. In fact, for the minimum velocity intercept solution (the longest time of flight considered in this analysis), the neutron arrives at the location of the intercept with *only* a horizontal component to its velocity.
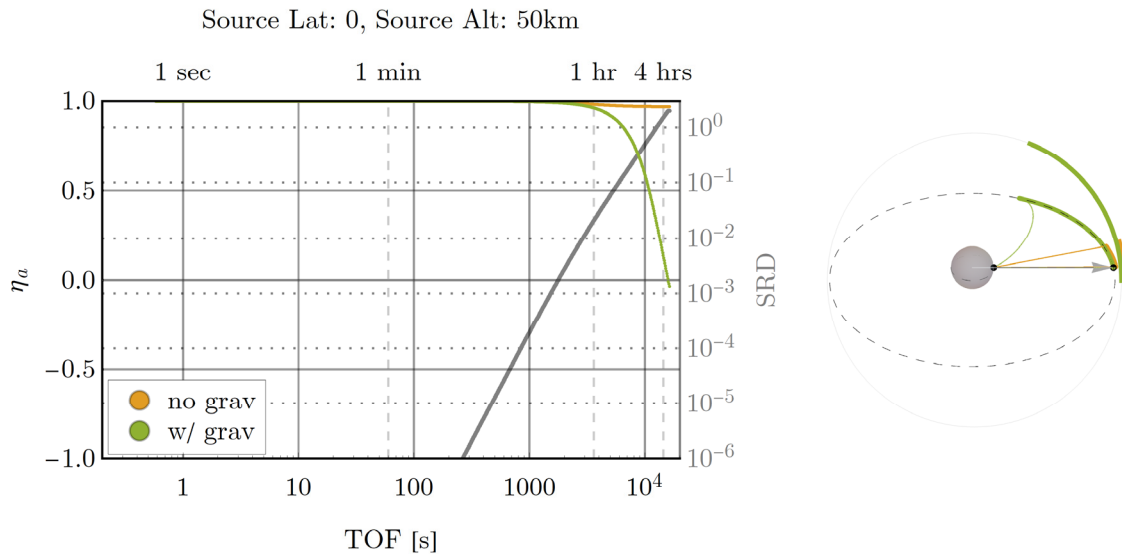
Figure 36: Arrival nadir cosine as a function of time of flight from an equatorial source at 50 km to a detector at $\Delta\alpha = 0°$ at time of emission with and without gravity.

This is confirmed in the nadir-azimuth output from HATS-n, shown in Figure 37. The decrease in nadir cosine from the first-flight analysis can be seen in the HATS-n plot of nadir cosine: Cosine values range from one down to slightly less than zero. The values slightly less than zero are the neutrons arriving with a small negative radial component of velocity. These *inbound* neutrons have their apogee just above the satellite's orbital radius. HATS-n is intended to find the *outbound* rendezvous, but where the inbound and outbound rendezvous are close enough together, the inbound one is sometimes found by the rendezvous solver. The nadir-azimuth plot (lower portion of Figure 37) shows the directions from which contributions arrive as seen by the detector. Gravity greatly extends the range of directions from which neutrons arrive at the detector, including from above (nadirs greater than 90 degrees).

Figure 37: Intercepted neutron current density as a function of nadir-azimuth computed by HATS-n for an equatorial Watt-fission-235 neutron source at 50 km with and without gravity as seen by stationary and geostationary detectors at $\Delta\alpha = 0°$ at time of emission.

As the source moves out of the equatorial plane, these plots change. Figure 38 shows the nadir-azimuth plots from HATS-n for the same source at 45ºN. This is due to the shape of orbital trajectories of neutrons arriving in these direction bins. The orbital trajectory is confined to a plane containing the emission point, the detector, and the center of the earth. With the emission point(s) at or near 45ºN, this confines the direction of the neutron as it reaches the intercept to be

118

south-westerly. Adding the motion of the detector gives the distributions shown

in Figure 38.

Figure 38: Intercepted neutron current density as a function of nadir-azimuth computed by HATS-n for a Watt-fission-235 neutron source at 50 km and 45°N with and without gravity as seen by stationary and geostationary detectors at $\Delta\alpha = 0°$ at time of emission.

Rising Detector

Next, consider a rising detector, with $\Delta\alpha = -92°$, where the detector is

just below the horizon (as viewed from the emission point) at the time of

emission but may come into view during the time of flight. Neglecting gravity,

rendezvous is not possible until the time of flight is such that the detector rises above the horizon. With gravity, the neutron can travel over the horizon to intercept the detector before it rises for the earliest straight-line intercept. In this case, the line-of-sight is obstructed but the flight path is clear. Figure 39 shows the range of times of flight for emission energies to intercept the rising detector. Note the difference in the orbit segments covered on the right side of the figure: The earliest intercepts are available with gravity. These neutrons are emitted with direction and energy such that they fall over the horizon to intercept a detector that has not yet achieved line of sight. These early intercepts correspond to the few dots visible at early time and high energy in the time and energy integrated plots at the top of Figure 41: These are rare contributions from neutrons emitted at high energy in the direction of the source and scatter at a location such that the probability of scatter to the detector and escape probability from the atmosphere is high.

Figure 39: Emission energy as a function of time of flight from a source at 50 km and 45ºN to a detector at $\Delta\alpha = -92°$ and rising at time of emission with and without gravity.

Figure 40: Arrival energy as a function of time of flight from a source at 50 km and 45ºN to a detector at $\Delta\alpha = -92°$ and rising at time of emission with and without gravity.
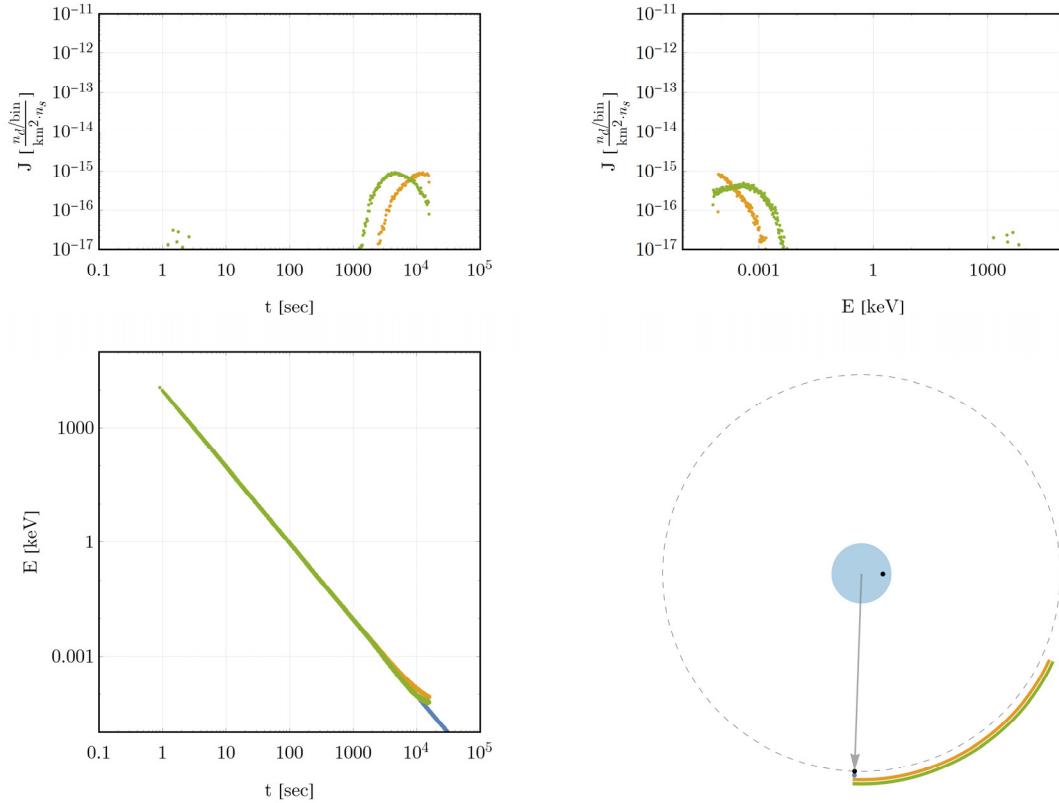
Figure 41: Intercepted neutron current density as a function of time-energy computed by HATS-n for a Watt-fission-235 neutron source at 50 km and 45°N with and without gravity as seen by stationary and geostationary detectors at $\Delta\alpha = -92°$ and rising at time of emission.

Setting Detector

The case of a setting detector, with $\Delta\alpha = 83°$, is shown in Figure 42. Here, for the full range of emission energies considered, it is possible for the neutron to intercept the satellite when gravity is included. Compare this to the range of rendezvous restricted by line of sight when neglecting gravity. Figure 43 shows the arrival energy of neutrons as a function of time of flight. Note that at the longest times of flight the energy of arrival increases slightly: At these times of

122

flight, the kinetic energy of the neutron in the reference frame of the detector is dominated by the motion of the detector and the intercept geometry is such that the apparent energy of arriving neutrons is increased.
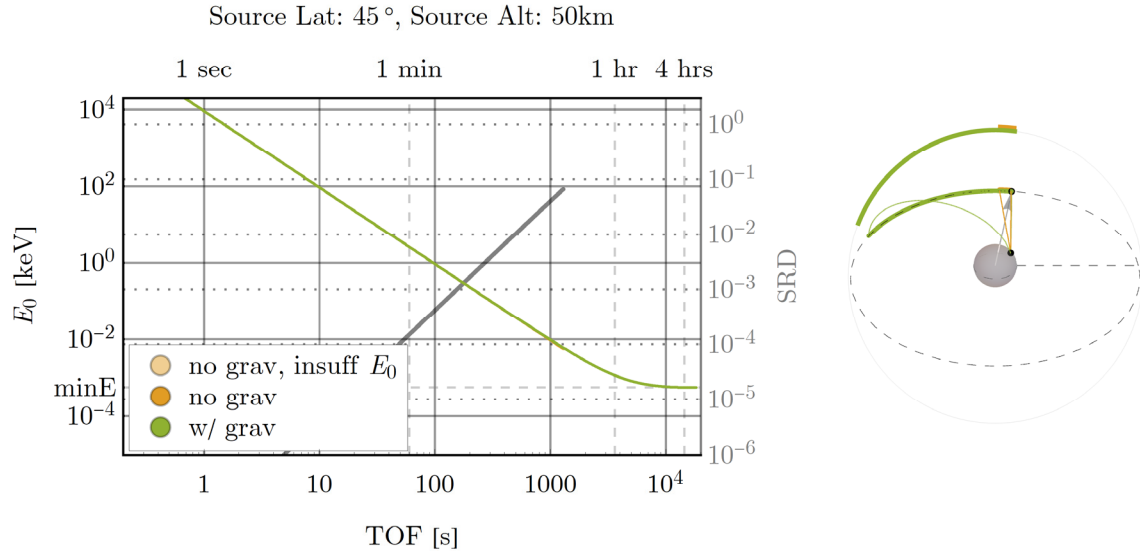
Figure 42: Emission energy as a function of time of flight from a source at 50 km and 45°N to a detector at $\Delta\alpha = 83°$ and setting at time of emission with and without gravity.
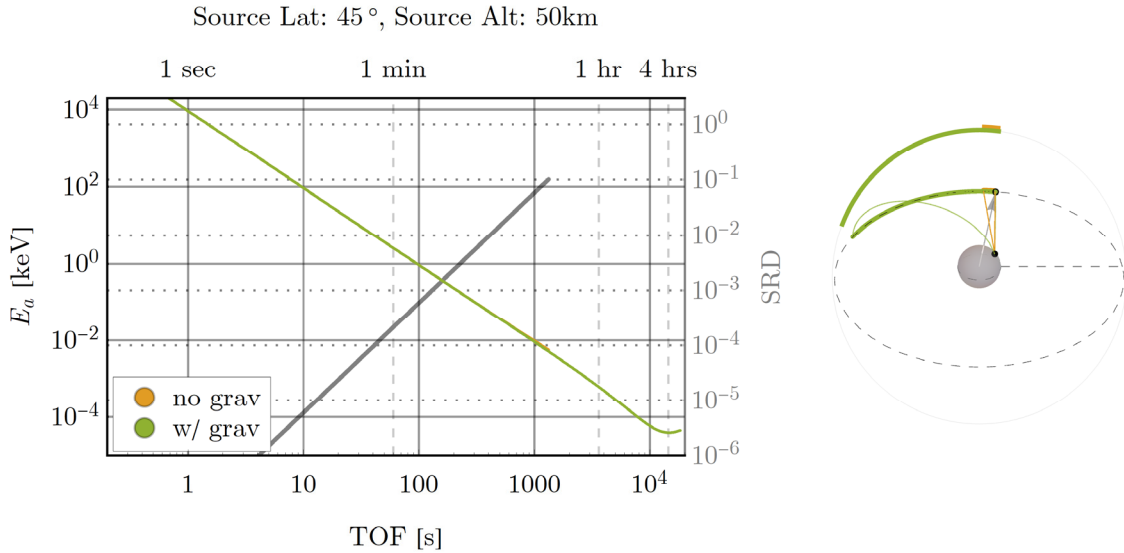
Figure 43: Arrival energy as a function of time of flight from a source at 50 km and 45°N to a detector at $\Delta\alpha = 83°$ and setting at time of emission with and without gravity.

Figure 44 shows the time-energy results from HATS-n for the same transport problem. The HATS-n plots of intercepted neutron current density integrated in time and energy match the expected time of flight and arrival energies from the first-flight analysis in Figure 43 including the small hook at the long time of flight visible in the time-energy position plot. However, note the gap in time-energy contributions near time of flight of 8000 seconds and arrival energy near 0.1 eV. There is an interruption of line of sight to the detector at this point in the spectrum. The interruption in line of sight in this case fell between grid points in the first flight analysis. Further discussion of the gap in line of sight follows in the next section.
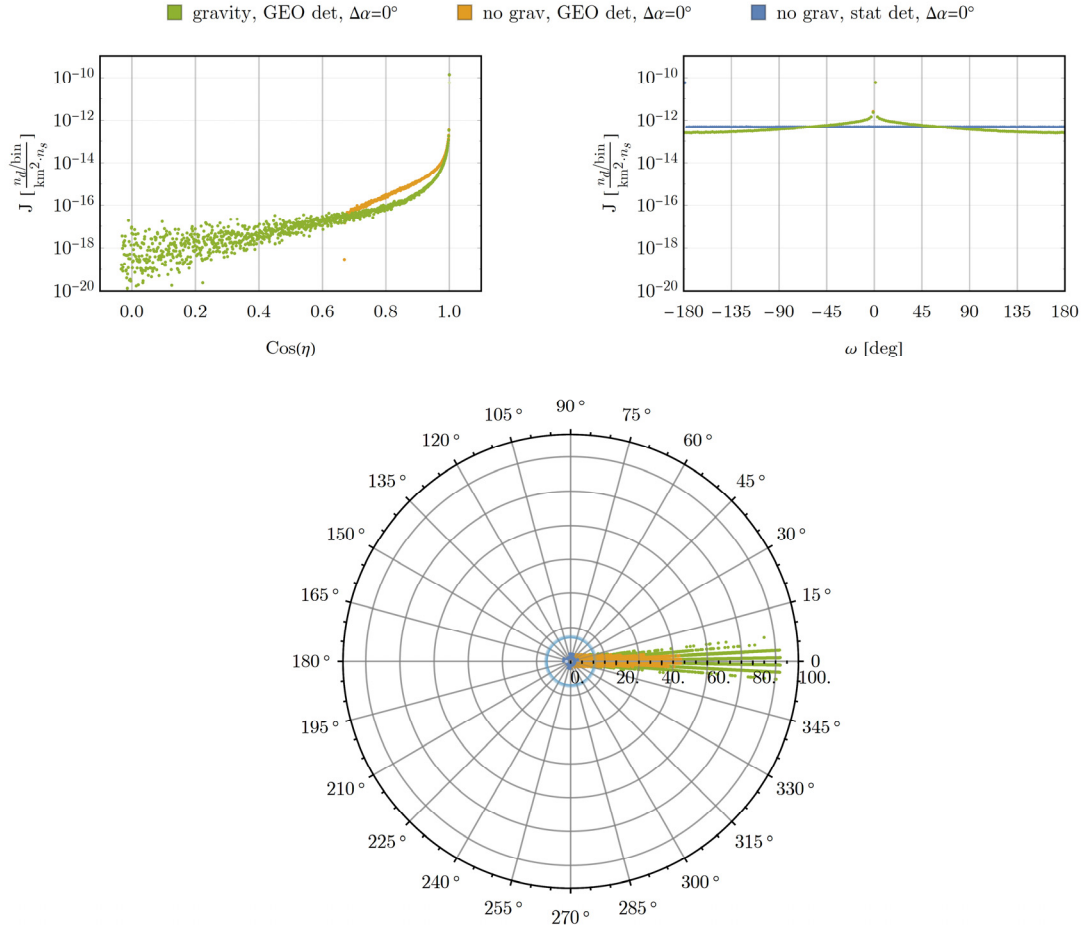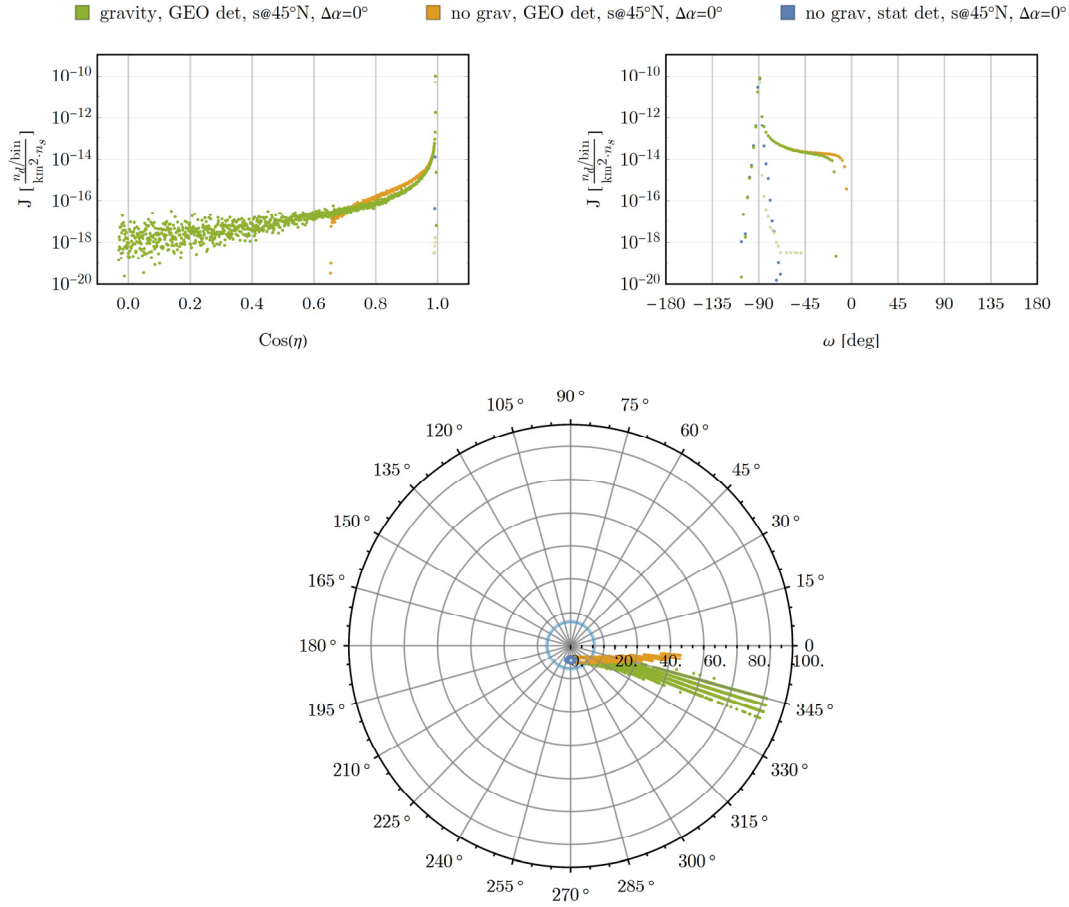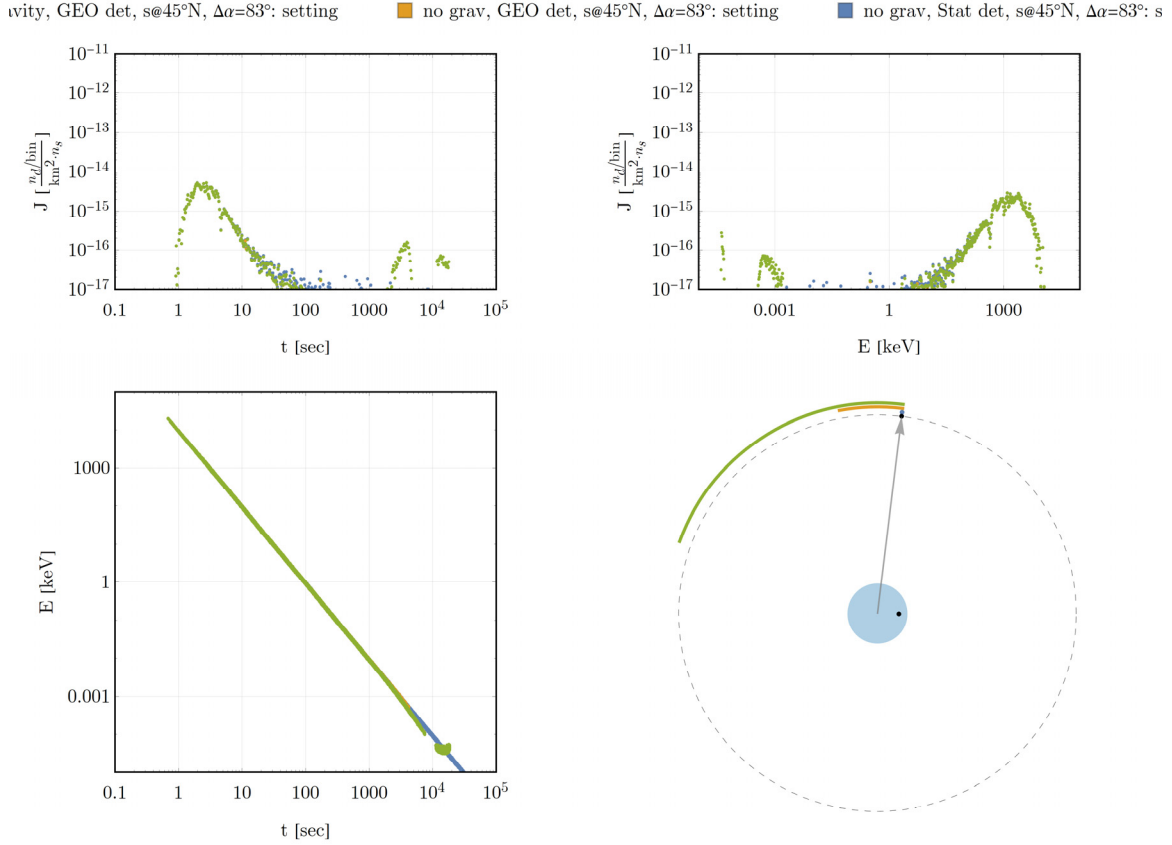
Figure 44: **Intercepted neutron current density as a function of time-energy computed by HATS-n for a Watt-fission-235 neutron source at 50 km and 45°N with and without gravity as seen by stationary and geostationary detectors at** $\Delta\alpha = 83°$ **and setting at time of emission.**

Temporal Interruption of the Clear Trajectory

As observed in the previous output from HATS-n (Figure 44), with gravity, the setting detector geometry can include a gap in the clear trajectory to the detector. Figure 45 and Figure 46 show the emission energy and arrival energy as a function of time of flight for a setting detector geometry, with $\Delta\alpha = 87°$, where clear trajectory to the detector is interrupted by the earth, but reacquired at some later time of flight. Consider the view of a setting detector from the emission point in the ECI frame. The aim-point, or emission direction, to

125

intercept the detector needs to *lead* the detector (by aiming down towards the horizon) in order to compensate for detector motion during the time of flight. However, gravity will cause the neutron to *fall* towards the center of the earth, down towards the horizon, during the flight to the detector. To compensate for gravity, the aim-point to intercept the detector is adjusted by aiming up away from the horizon. For short times of flight, the fall of the neutron on the trajectory is small, so leading the target (aiming lower towards the horizon) dominates the selection of the aim-point. As the aim-point to intercept the detector drops below the horizon, the trajectory becomes obstructed. Then, as the time of flight increases, compensating for neutron fall on the longer time of flight trajectory becomes the dominant input to the aiming process and the aim-point rises back above the horizon. When it is far enough above the horizon, it becomes unobstructed. Thus, there is a time gap in the availability of a clear trajectory to the detector. Understanding this is important, lest such a gap be misinterpreted as a system fault.
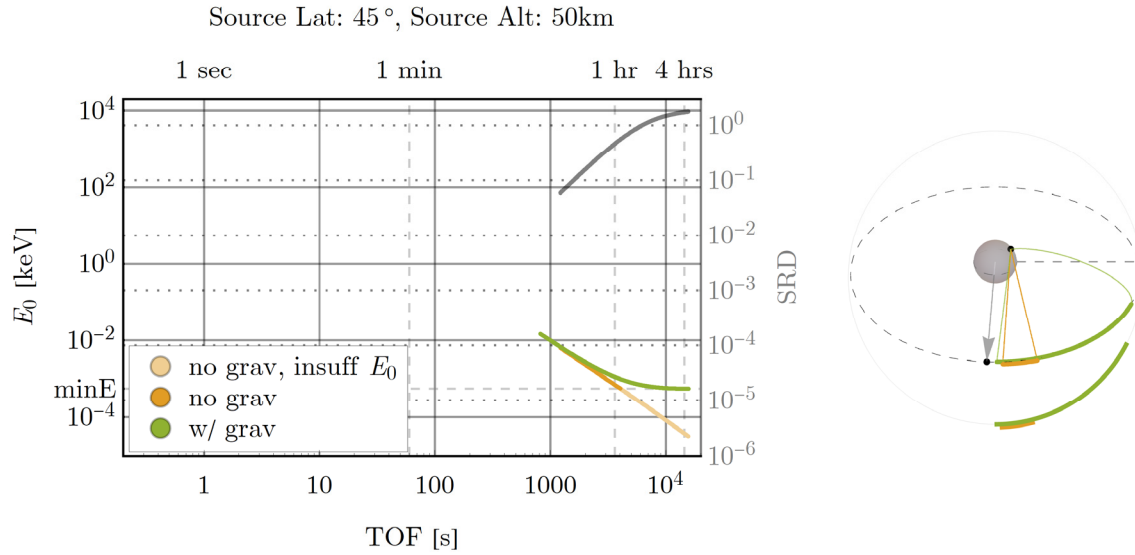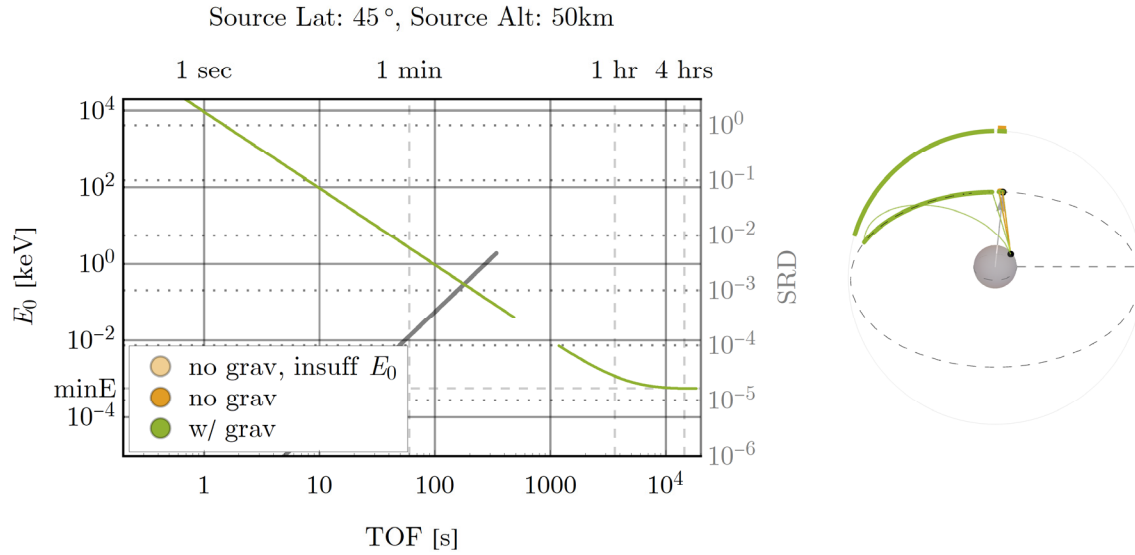
Figure 45: **Emission energy as a function of time of flight from a source at 50 km and 45ºN to a detector at $\Delta\alpha = 87°$ and setting at time of emission with loss and reacquisition of line of sight when including of gravity.**
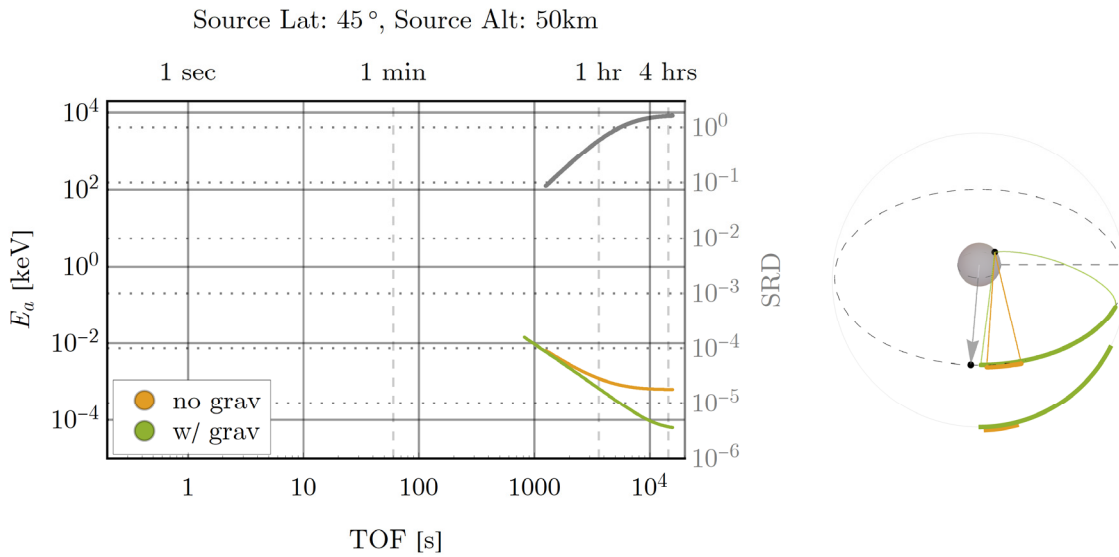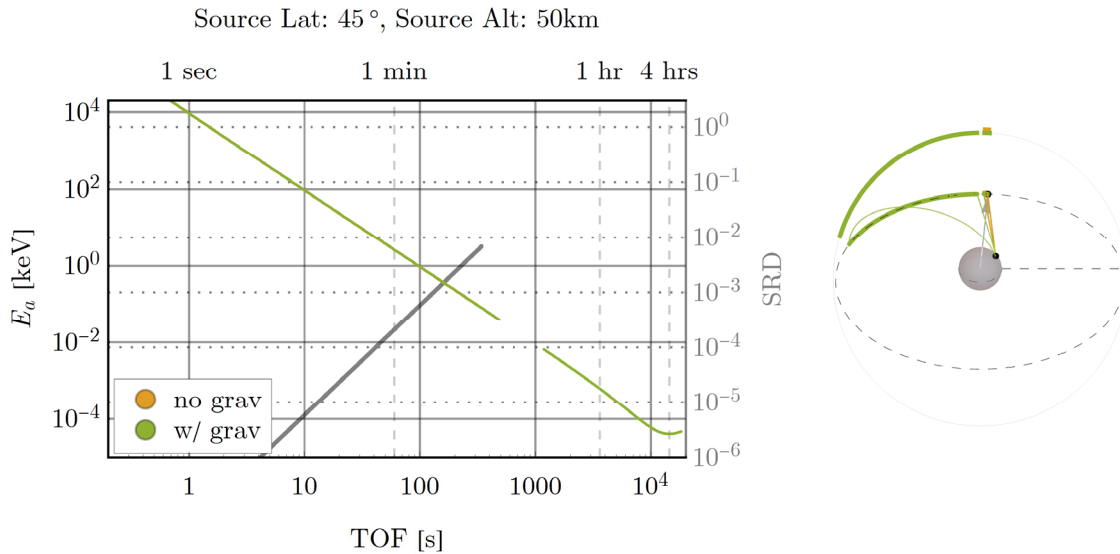

Figure 46: **Arrival energy as a function of time of flight from a source at 50 km and 45ºN to a detector at $\Delta\alpha = 87°$ and setting at time of emission with loss and reacquisition of line of sight when including of gravity.**

127

Detector Behind the Earth

With gravity, neutrons can arrive at the detector in some geometries in which they could not without gravity. There is no more profound difference in predictions using models than the difference between *some* neutrons and *no* neutrons.

One such case is when the detector is on the opposite side of the earth relative to the source. Two examples are presented: Sources at zero and 45°N. In both cases, a geosynchronous detector at $\Delta\alpha = 118°$ at time of emission and passing through $\Delta\alpha = 180°$ during the range of intercept times of flight was simulated, as well as a stationary detector fixed at $\Delta\alpha = 180°$. A stationary detector isn't realistic, but its results may be viewed as free-field estimates. For the equatorial source, the detector passes through the antipode. For the source at 45°N, the detector misses the antipode but does pass through its most distant point from the source.

Figure 47 shows the expected times of flight and arrival energies from the first-flight analysis to a geostationary detector passing through $\Delta\alpha = 180°$ with the source at 45°N during the range of times of flight over which intercepts are available at the detector. The neutrons able to reach the detector in this geometry are following low elevation paths in a northward direction. They then fall across the detector orbit from the northward direction. This geometry was also demonstrated in HATS-n. Figure 48 and Figure 49 show the time-energy and nadir-azimuth estimates as seen by the detector. The counting statistics are poor

for this number of histories, but the expected behavior can be confirmed: The

range and shape of the arrival energy versus time of flight curve from Figure 47

is present in the integrated time and energy plots and the time-energy position

output from HATS-n and the contributions arrive from the expected clusters of

northward directions in Figure 49 for the two detector types of detector motion.

Figure 47: Arrival energy as a function of time of flight from a source at 50 km and 45°N to a detector passing through $\Delta\alpha = 180°$ during rendezvous range.

One questionable difference is visible in the length of orbit segments

between the first flight analysis and the result from HATS-n (right side of Figure

47 and lower right side of Figure 48). The segment reported by the HATS-n run

appears to begin later but end at the same point predicted by the first flight

analysis. One possible explanation for this is aided by observing the emission

zenith as a function of time of flight for this geometry, Figure 50. The early times

of flight (possibly the range of times of flight excluded from the orbit segment) have a negative emission zenith. Neutrons on these trajectories have a long optical thickness to traverse to reach the detector, and given the poor counting statistics achieved in the HATS-n run for this geometry, it is possible that the contributions in those early time bins were too small to be numerically represented and underflowed to zero during the data processing and analysis steps in the code. At the time of this analysis, it remains unclear whether this is the reason for the disagreement between the first flight analysis and output from HATS-n: This has been added to the list of open issues for investigation and debugging in the HATS-n code.

Figure 48: Intercepted neutron current density as a function of time-energy computed by HATS-n for a Watt-fission-235 neutron source at 50 km and 45°N with gravity as seen by stationary and geostationary detectors at or passing through $\Delta\alpha = 180°$ during rendezvous.
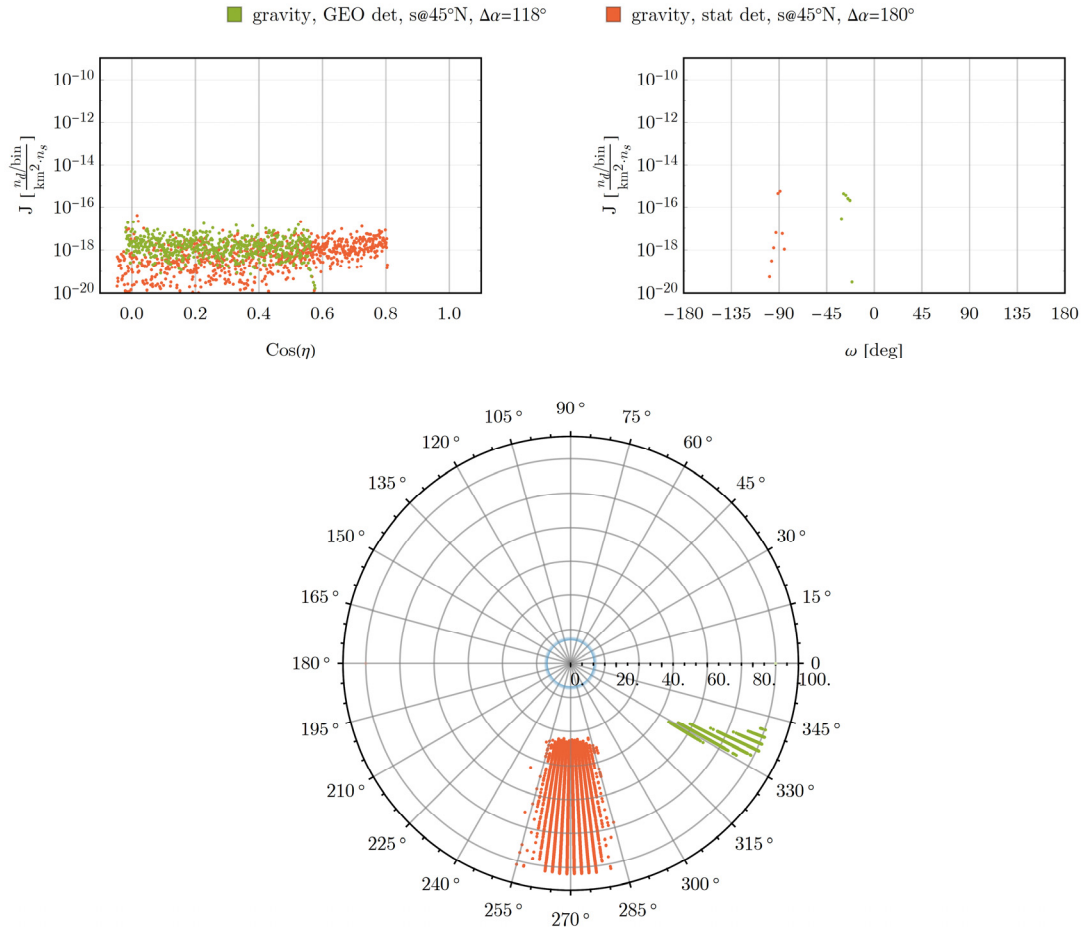
Figure 49: Intercepted neutron current density as a function of nadir-azimuth computed by HATS-n for a Watt-fission-235 neutron source at 50 km and 45°N latitude with gravity as seen by stationary and geostationary detectors at or passing through $\Delta\alpha = 180°$ during rendezvous.
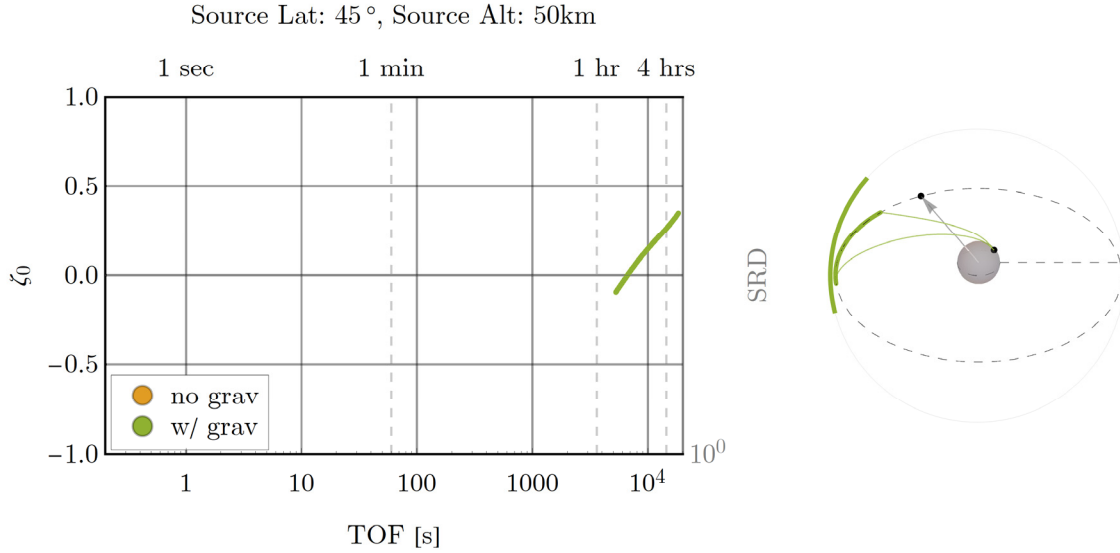
Figure 50: Emission zenith cosine as a function of time of flight from a source at 50 km and 45°N to a detector passing through $\Delta\alpha = 180°$ during rendezvous range.

The second case places the source in the equatorial plane so that the detector passes through the antipode. This confines all intercepting first-flight trajectories to equatorial orbits in the first flight analysis to meet the geostationary detector (except for rendezvous exactly at the antipode). The result, shown in Figure 51, is a discontinuity in the energy at arrival between short and long times of flight. The short times of flight intercept the detector before it passes through the antipode and follow trajectories that approach the detector from behind. As the detector passes through the antipode, the emission direction required for intercept switches to trajectories that approach the detector head-on. The time of flight where this switch occurs is the location of the discontinuity in arrival energy. All these are the outward-bound intercepts, meaning that the radial component of the neutron velocity in the ECI frame is

positive (or zero) computed by HATS-n. There are westbound intercepts that arrive before the discontinuity and eastbound intercepts that arrive after the discontinuity, but these are inbound intercepts and are not often found by the rendezvous solver. If these were included, there would be two arcs that overlap in time of flight but are at different arrival energies. (This capability should be added for a production code, presuming the detector of interest is not collimated in a way that prevents detection of downward-moving neutrons, but it was not required in demonstrating the need to include motion and gravity for this class of problems.)
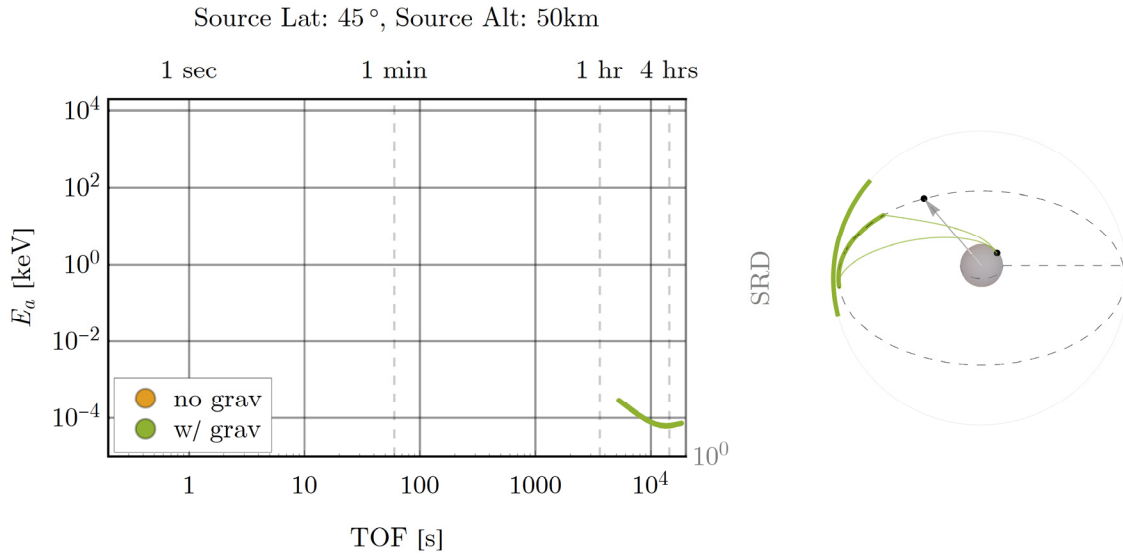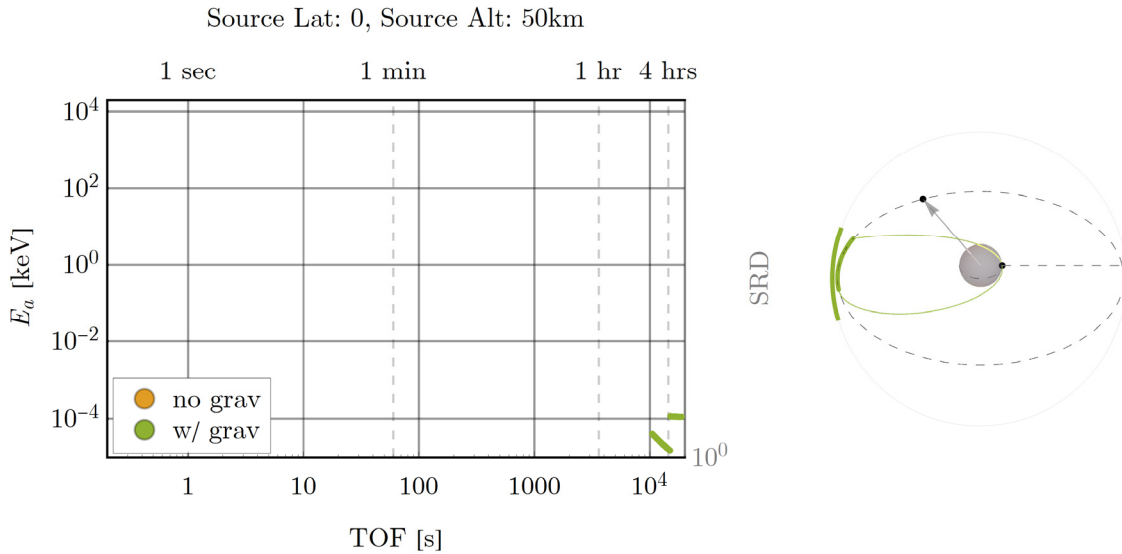

Figure 51: **Arrival energy as a function of time of flight from a source at 50 km and 45ºN to a detector passing through** $\Delta\alpha = 180°$ **during rendezvous range.**

Figure 52 and Figure 53 show the time-energy and nadir-azimuth results from a HATS-n run for the distribution of neutrons from an equatorial source as

seen by a geostationary detector passing through the antipode and a stationary detector at the antipode. As with the non-equatorial source, the counting statistics are poor, but some expected behavior can still be observed. The time-energy position plot in the lower left side corner of Figure 52 shows the discontinuity in the arrival energy and time of flight predicted by the first flight analysis.

The distribution in arrival direction, Figure 53, also shows interesting features. For the stationary detector, the contributions at the detector are arriving from trajectories that had to fly around the earth to reach the detector, so that they arrive with nadirs near horizontal, but are spread uniformly in azimuth. This effect is limited to geometries in which the source, detector, and center of the earth are collinear (equatorial source and detector). The nadir-azimuth plot in Figure 53 also includes the distribution of directions from the equatorial source as seen by a geostationary detector that passes through the antipode. The ring of arrival directions is still visible, as a result of the contributions arriving at the instant at which the detector passes through $\Delta\alpha = 180°$, although it has been distorted by the addition of detector motion. As the detector approaches $\Delta\alpha = 180°$ from $\Delta\alpha = 118°$ the contributions arrive at the detector on predominantly eastbound trajectories, and after the detector passes through $\Delta\alpha = 180°$ the contributions arrive on predominantly westbound trajectories.
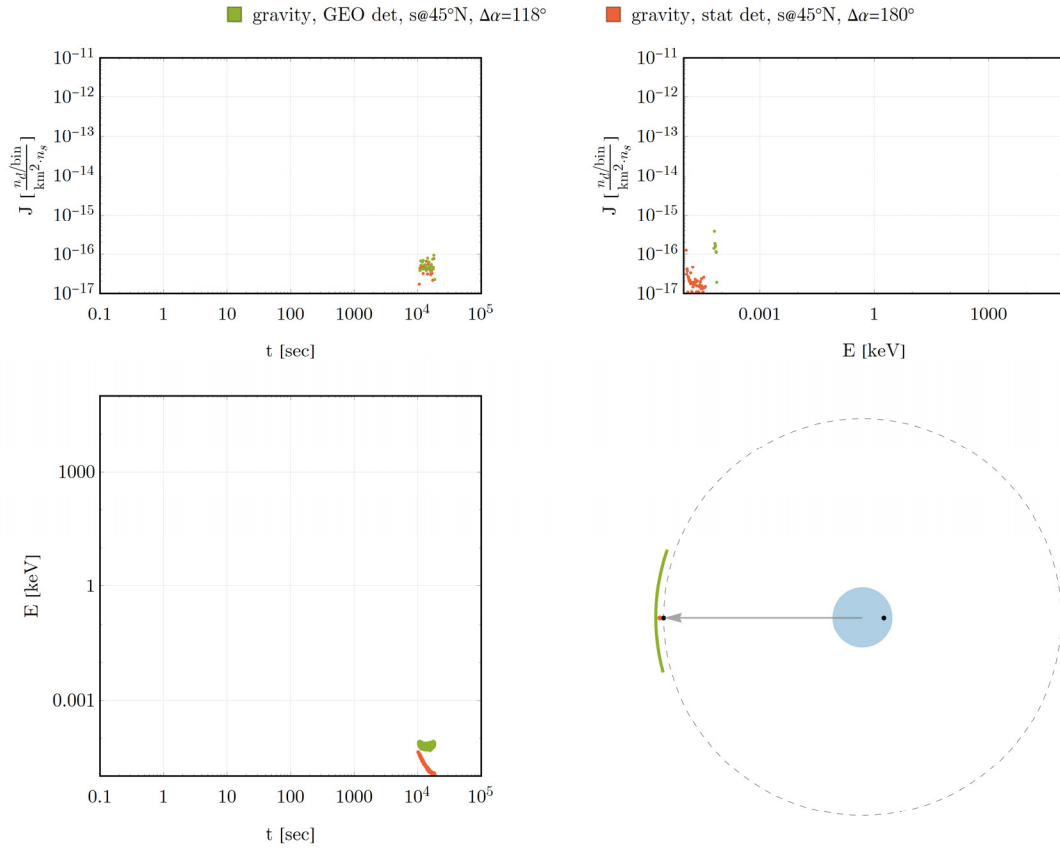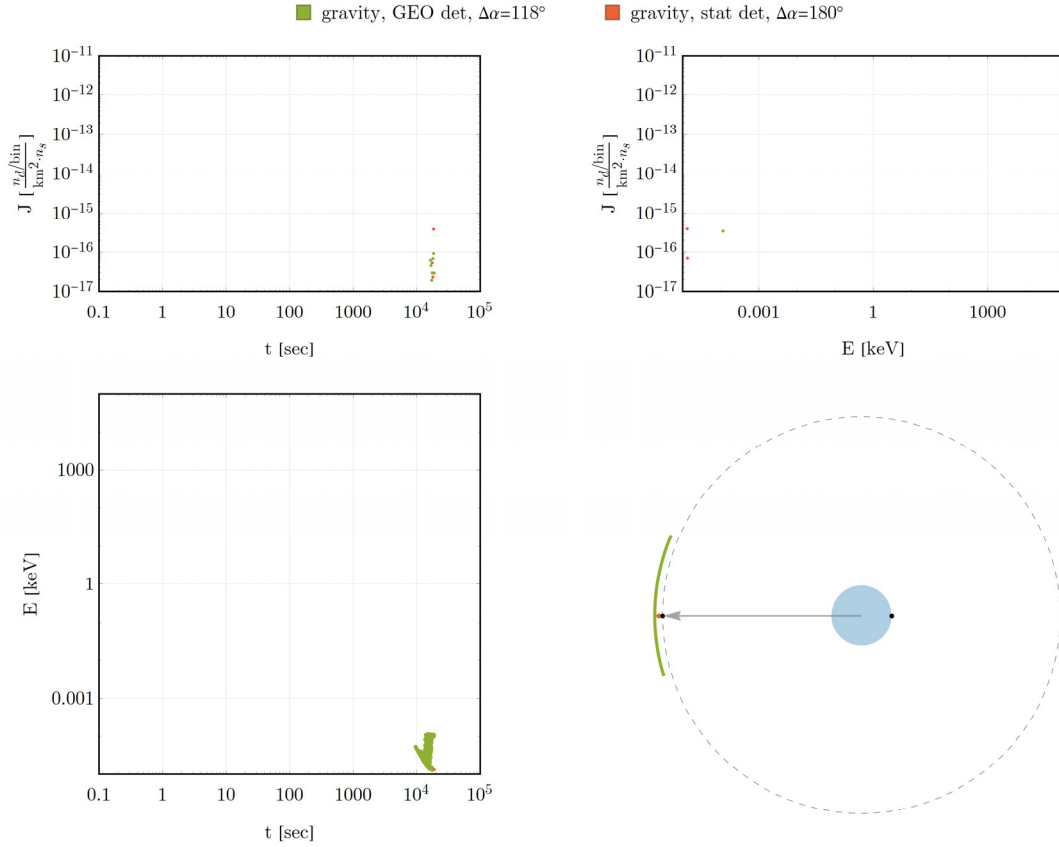
Figure 52: Intercepted neutron current density as a function of time-energy computed by HATS-n for a Watt-fission-235 equatorial neutron source at 50 km with gravity as seen by stationary and geostationary detectors at or passing through $\Delta\alpha = 180°$ during rendezvous.
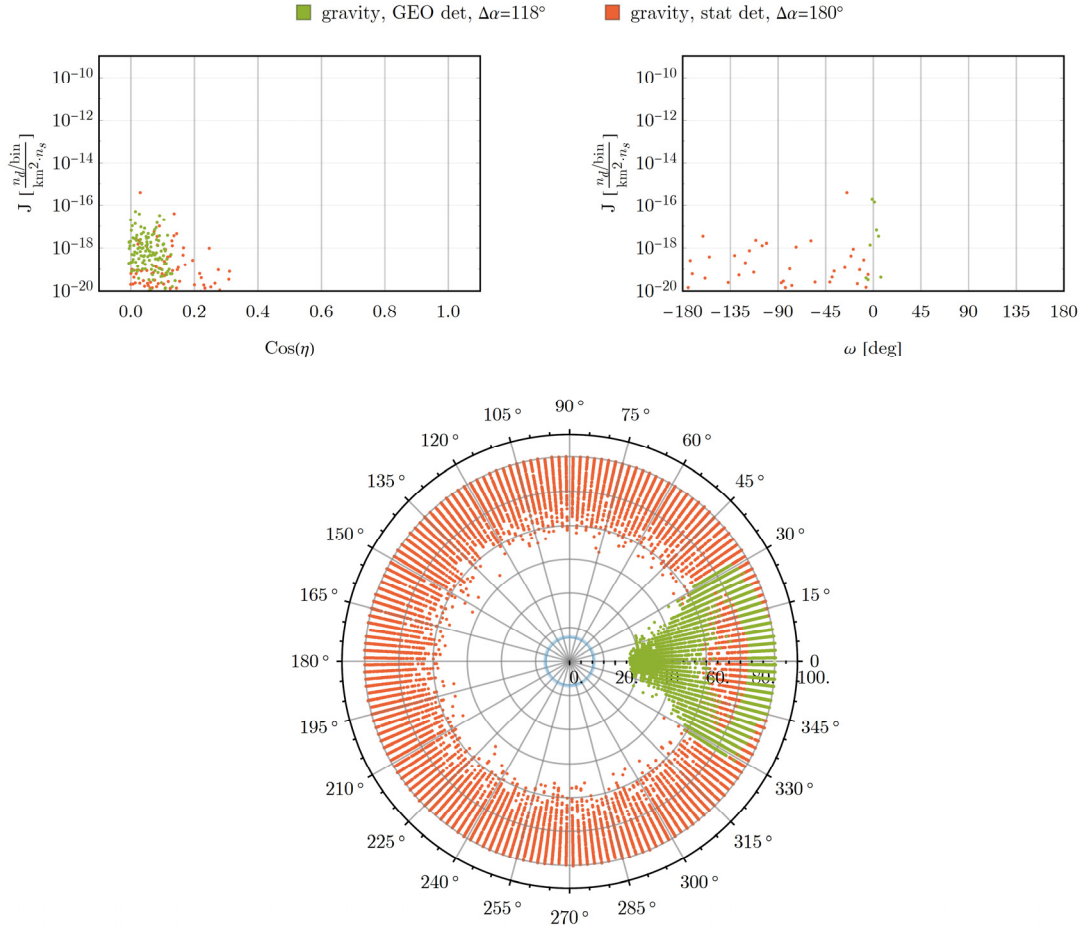
Figure 53: **Intercepted neutron current density as a function of nadir-azimuth computed by HATS-n for a Watt-fission-235 equatorial neutron source at 50 km with gravity as seen by stationary and geostationary detectors at or passing through $\Delta\alpha = 180°$ during rendezvous.**

Polar Source

Another interesting case that arises with gravity is the view of a source located at the pole. Without gravity, sources below approximately 74 km do not have line of sight to a geostationary detector at any point on the detector orbit. Even for sources above this threshold, the magnitude of contributions tallied at the detector is low because of the long initially downward and optically thick path through the atmosphere required for every first-flight trajectory. The

scattered contribution from the vicinity of the source is similarly limited, so that the largest contributions tallied at the detector are from the rare chains of events that scatter the neutron to a location in the atmosphere where line of sight was available to the detector without a long optical path through the atmosphere to reach the detector. Thus, without gravity, a large population of scatters is ignored due to obstructed lines of sight and another population has its importance reduced by artificially long path lengths through the atmosphere.

With gravity, neutrons with the right combination of energy and zenith angle pass through the satellite orbit at various times and at all satellite right ascensions at each time. (Right ascension is indeterminate above the poles, so $\Delta\alpha$ has no meaning in the case.) Thus, a geostationary satellite is exposed to neutrons regardless of its initial location in its orbit. For sources close enough to either pole, this is also the case, but the range of energies and times of flight vary with $\Delta\alpha$ for sources not exactly at the pole.

The time of flight as a function of emission energy and energy at arrival as a function of time of flight for neutrons emitted from a source 50 km over the north pole is shown in Figure 54 and Figure 55 respectively. From this altitude, neutrons will less than approximately 10 eV may follow orbital trajectories to rendezvous with a geostationary detector. Neutrons with energy above this threshold have a required emission zenith too low in elevation to have a clear trajectory to the detector. First-flight neutrons arrive at the detector just under 1000 seconds after time of emission and range in energy from 10 eV down to less

138

than 0.1 eV. For the earliest times of flight, approximately 1000 to 3000 seconds, the emission zenith is actually downward as shown in Figure 56. This is expected, as the highest energy neutrons able to make the rendezvous will approach the straight-line trajectory, but it also means that these neutrons will have a long optical thickness to traverse to intercept the detector and will have a correspondingly smaller contribution to tally. For times of flight greater than 3000 seconds, the emission zenith is positive and increasing with time of flight so that longer times of flight traverse shorter optical thicknesses through the atmosphere on the path to the intercept. This is illustrated in Figure 57: The effective path length decreases by five orders of magnitude from the earliest to the latest times of flight.
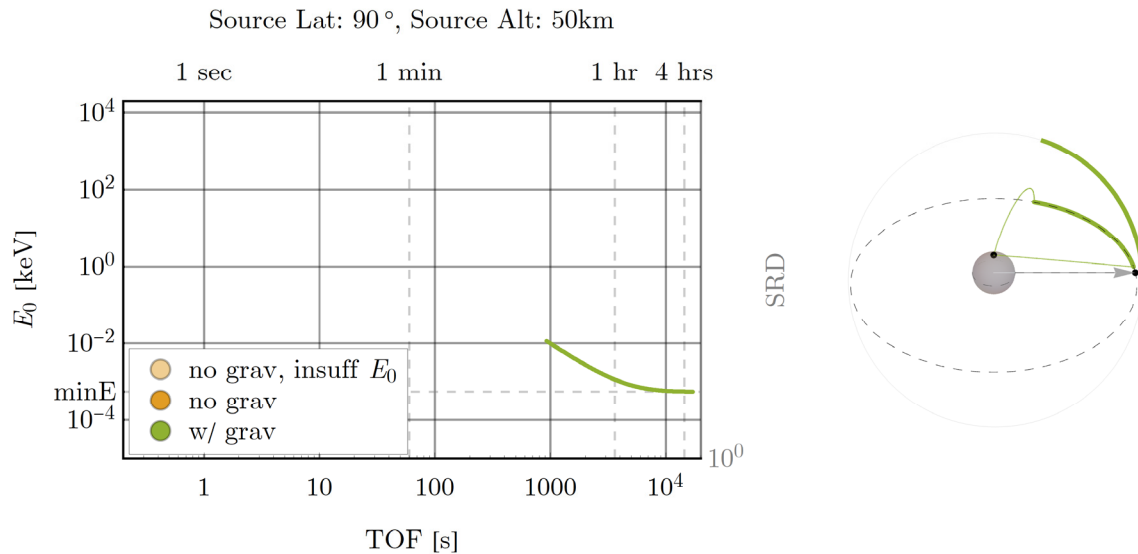
Figure 54: Emission energy as a function of time of flight to a geostationary detector from a source at 50 km altitude at the north pole.
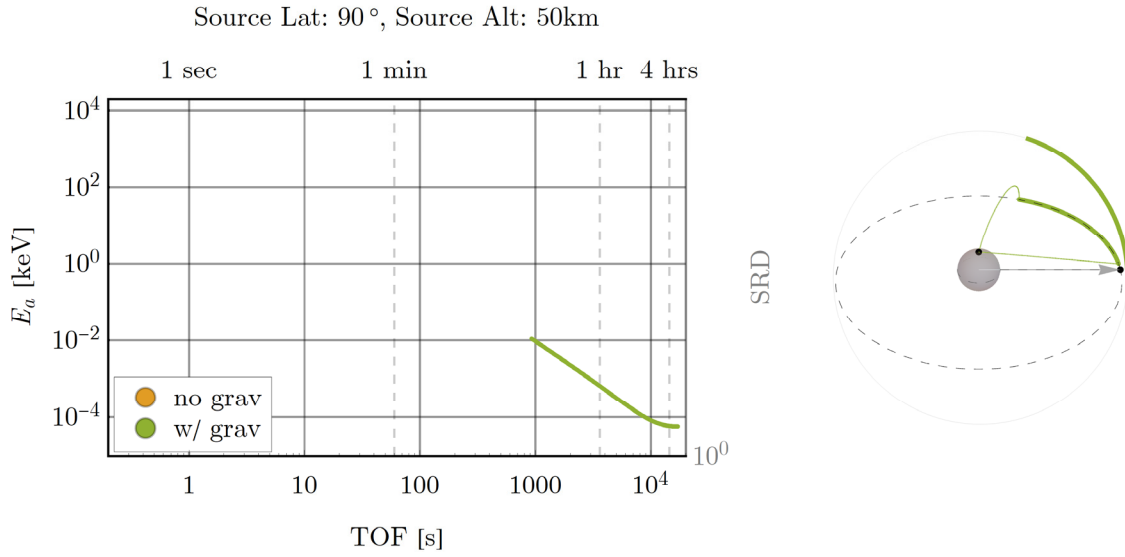
Figure 55: Arrival energy as a function of time of flight to a geostationary detector from a source at 50 km altitude at the north pole.
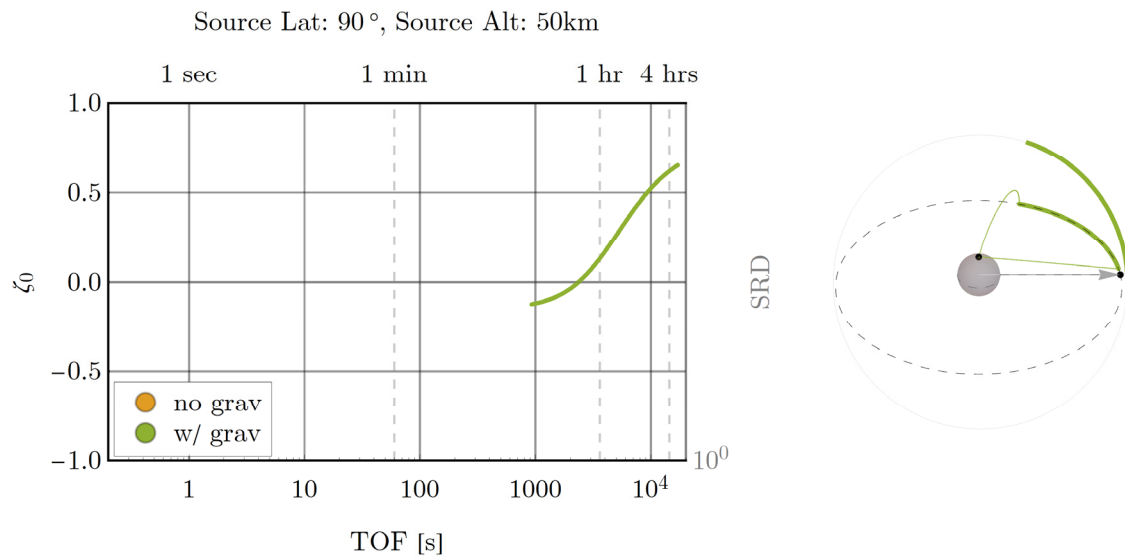
Figure 56: Emission zenith as a function of time of flight to a geostationary detector from a source at 50 km altitude at the north pole.
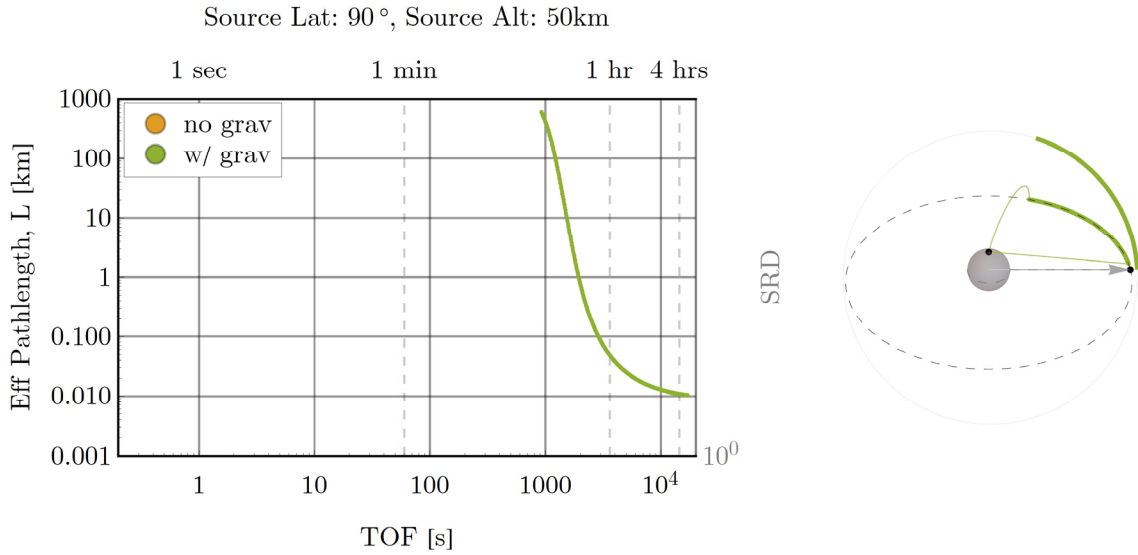
Figure 57: Effective path length as a function of time of flight to a geostationary detector from a source at 50 km altitude at the north pole.

The results of the first-flight analysis are observed in output from the HATS-n code. Figure 58 and Figure 59 show the time-energy and direction distributions of neutrons from a polar source as seen by a geostationary detector estimated by HATS-n. As with earlier examples, the intensity and counting statistics of the direct contribution alone is poor, so the scattered contribution may be qualitatively compared to the first flight analysis since most of the scatters occur in the vicinity of the source. Times of flight after 1000 seconds and arrival energies below 10 eV are observed as predicted, with the lower times of flight (1000 to 3000 seconds) and higher energies (10 eV down to 1 eV) attenuated by the long optical thickness traversed for each contribution. The HATS-n output also shows a low intensity (with very poor counting statistics) distribution of neutrons arriving at the detector with times of flight as low as one

second and energies as high as 2 MeV. These are due to rare chains of events
that result in fast neutrons scattering to a location in the atmosphere where they
have line of sight to the detector in a next-event. In the context of the transport
problem, these events are not particularly rare in this problem: any scatter at an
altitude above 74 km will have line of sight to the detector.
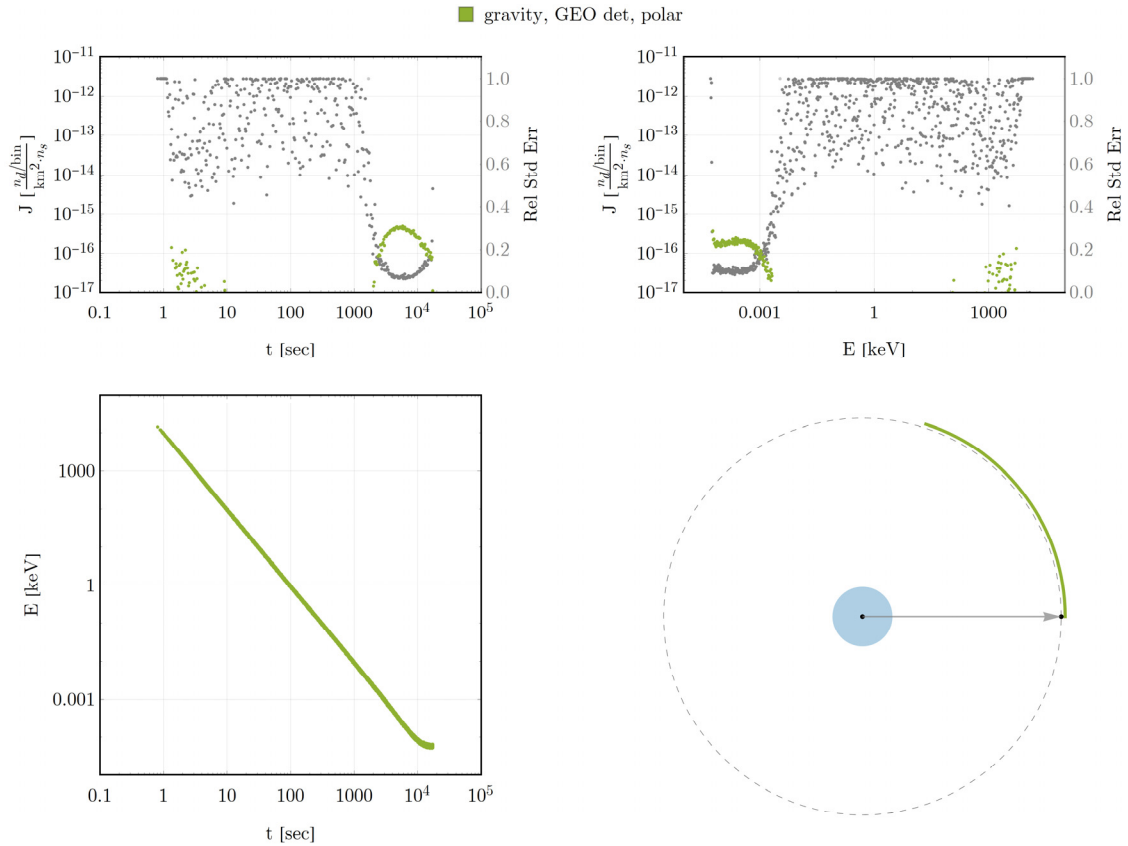
Figure 58: Intercepted neutron current density at a geostationary detector as a function of time-energy computed by HATS-n for a Watt-fission-235 neutron source at 50 km and above the north pole.

The relative standard error (gray dots in Figure 58 and Figure 59) indicate
the variance for the estimated neutron current density in each bin (shown in

green). Relative standard error near 1 indicates large variance (hence poor convergence). In this case, the variance is high over much of the range of time and energy because the envelope of available neutron energies and times of flight at which flights to the detector is limited. As a result, contributions outside this envelope result from rare events with appropriately poor counting statistics (thus the high relative standard error). Observe the low relative standard error at long times of flight and low energies in Figure 58: This shows the time-energy envelope where the population of contributions is high (yielding an estimate with lower variance).
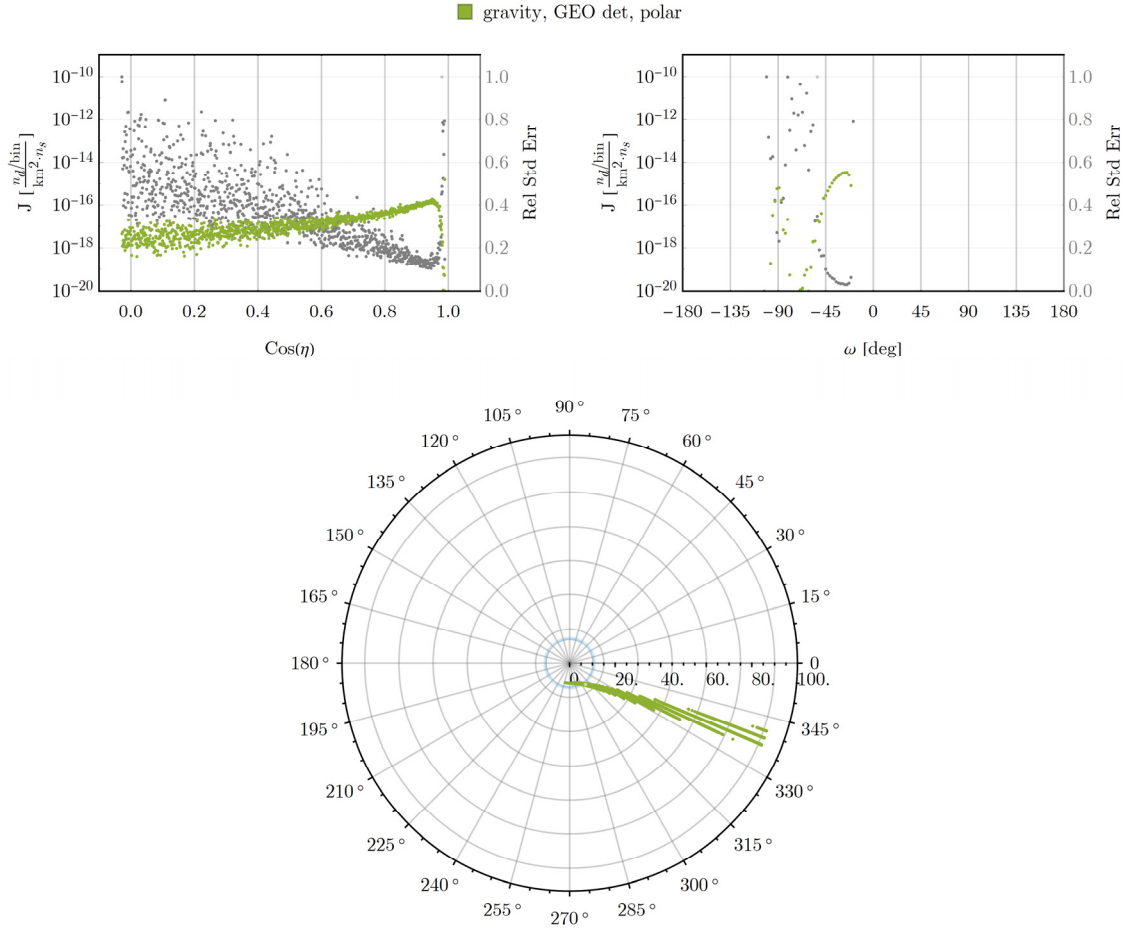
Figure 59: **Intercepted neutron current density as a function of nadir-azimuth computed by HATS-n for a Watt-fission-235 neutron source at 50 km and above the north pole geostationary detector.**

Divergence Factor

The influence of gravity on divergence factor is significant, particularly for longer times of flight. In the case of an source-detector geometry with $\Delta\alpha = 0°$, Figure 60, the divergence factor is initially lower (more divergence) for shorter times of flight. Gravity causes the adjacent trajectories to spread apart faster than just the spatial divergence from the straight-line case. The effect becomes pronounced for middle times of flight (5000 to 7000 seconds) and then the

144

divergence factor begins to increase until it becomes larger than the straight line case for the longest times of flight. This is a result of the change in direction of incidence that influences the effective area of the detector. As in the discussion of divergence factor from relative motions, this increase in effective detector area was due to the incidence angle approaching perpendicular. In this case, the increase in effective area is a result of the turning of the neutron trajectory as it approaches the rendezvous and the closing speed of the neutron with the detector becomes small. The increase in effective area of the detector greatly reduces the divergence at the longest times of flight.
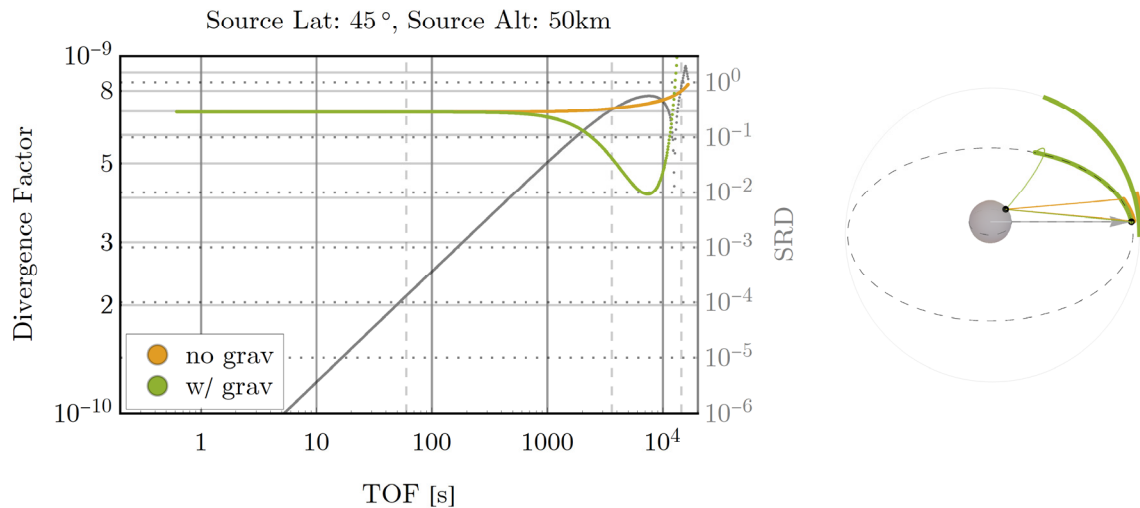
Figure 60: Divergence factor as a function of time of flight from a source at 50 km and 45ºN to a detector at $\Delta\alpha = 0°$ with and without gravity.

Optical Thickness Through the Atmosphere

For a given source-detector geometry, the rendezvous trajectories found with and without gravity have different emission zeniths resulting in wide variation in effective path length through the atmosphere. Figure 61 shows the EPL through the atmosphere to meet a setting detector, with $\Delta\alpha = 83°$, from a source at 50 km and 45°N. For shorter times of flight, the EPL initially remains close to the EPL for the no-gravity intercept. However, as the emission zenith of the orbital trajectory to intercept increases, as shown in Figure 62, the effective path length then falls off for longer times of flight. In general, for longer times of flight on orbital intercepts, the required emission zenith is closer to vertical. This results in a shorter effective path length, hence less attenuation and larger contributions in these late-time bins at the detector.
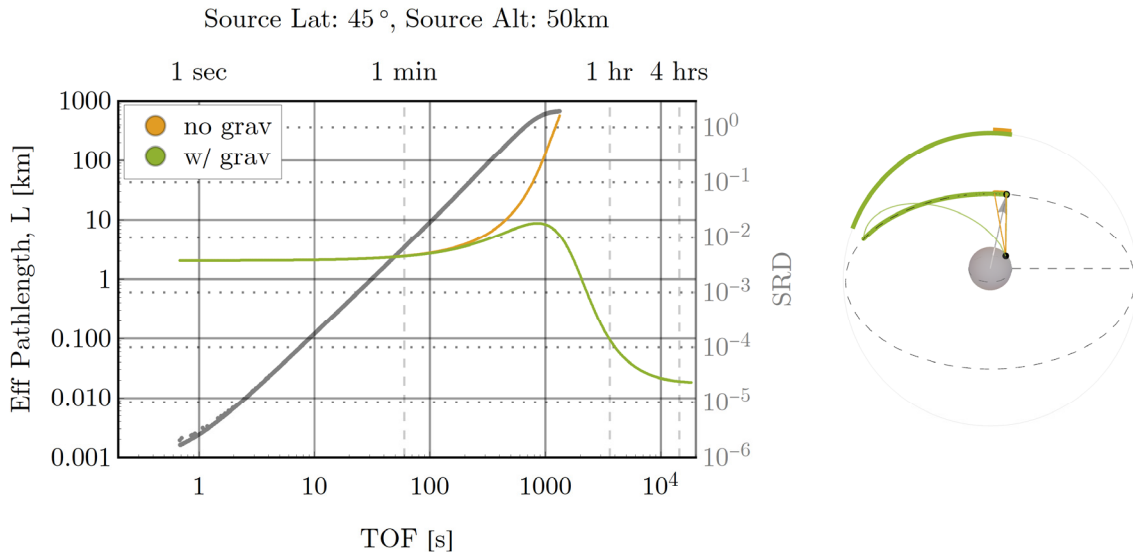
Figure 61: **Effective path length as a function of time of flight from a source at 50 km and 45°N to a detector at $\Delta\alpha = 83°$ and setting at time of emission with and without consideration of gravity.**
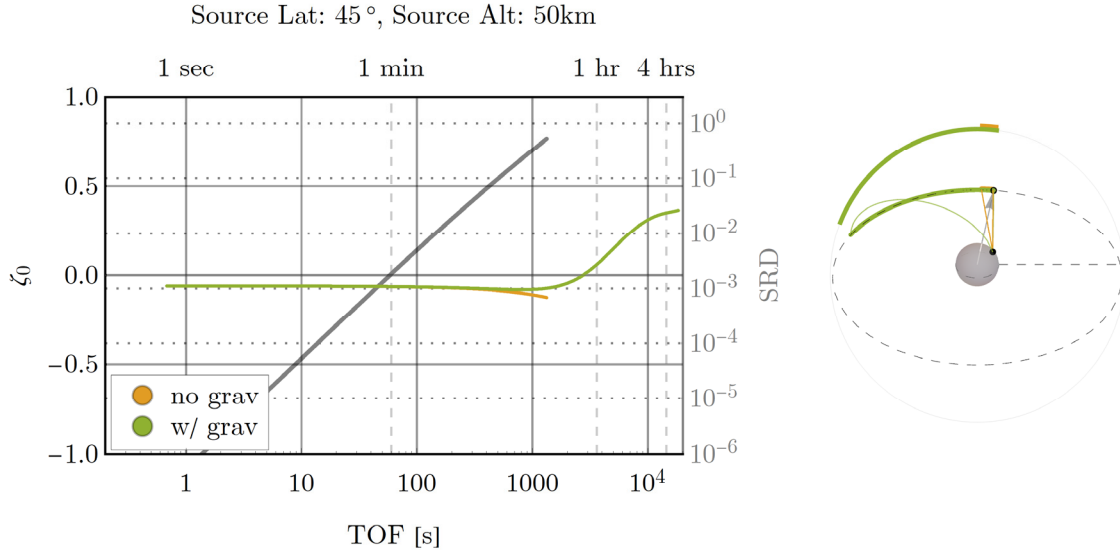
Figure 62: Zenith cosine as a function of time of flight from a source at 50 km and 45ºN to a detector at $\Delta\alpha = 83°$ and setting at time of emission with and without consideration of gravity.

An Example of Combined Influence: Detector Motion and Gravity

With insight from exploration of the special features investigated during this research, it is informative to observe some of the changes visible in the results from a run of HATS-n for a simple problem geometry. For this example, limit consideration of special features of the problem to detector motion and gravity. Figure 63 and Figure 66 show the results from the HATS-n code for a Watt-fission-235 source at 50 km and 45ºN with a detector at $\Delta\alpha = 0°$ at the time of emission. Initially, HATS-n was run with stationary detector and no-gravity approximations (blue), followed by a geostationary detector and no-gravity (yellow). The final calculation was made using a geostationary detector and including gravity in the calculation of neutron flights (green).

147

The time-energy distributions seen by the detector, Figure 63, show little variation (or at least variation small enough to be hidden by the scale of the plot) for short times of flight and high energies. When looking at the results of the transport calculation in this context (this geometry on these scales), the effects of relative motions and gravity are visible, and quite pronounced, for times of flight longer than 1000 seconds and arrival energies less than 10 eV.

Initially, compare the no-gravity stationary detector and geostationary detector cases (blue and yellow). At times of flight longer than 10,000 seconds the intensity of contributions as seen by the detector falls off rapidly with the addition of detector motion. Since, in this particular geometry, the detector has passed its point of closest approach at meridian passage a neutron must have sufficient speed to close the distance with the detector as the distance to the detector increases with time of flight. For times of flight greater than 10,000 seconds, the population of neutrons meeting these criteria falls off rapidly. However, recall from the discussion of relative motions that many of these long time of flight intercepts computed by HATS-n result from neutrons with insufficient energy to reach geostationary altitude should gravity be taken into account. If the HATS-n model were to account for this, the sharp drop in contribution intensity would shift from time of flight of 10,000 seconds back to approximately 1,000 seconds.

Next, consider the HATS-n estimate including both detector motion and gravity (green). At long times of flight, there is a decrease in the intensity of

contributions as seen by the detector. This is attributed to the influence of the divergence factor and effective path length to the detector for these intercept trajectories. Figure 64 shows that for times of flight less than 10,000 seconds and arrival energies greater than 0.1 eV, the divergence factor is small reducing the magnitude of contributions. For times of flight greater than 10,000 seconds and arrival energies below 0.1 eV the divergence factor increases due to increasing effective area of the detector at intercept and the magnitude of contributions recovers. The change in magnitude of the accumulated histories is visible in the HATS-n output, but distorted by the competing influence of effective path length on the trajectories resulting in these contributions. Figure 65 shows that for times of flight longer than 1,000 seconds and arrival energies less than 1 eV the effective path length through the atmosphere for the trajectory that includes the consideration of gravity is shorter resulting in a larger contribution at the detector due to less attenuation in the atmosphere.
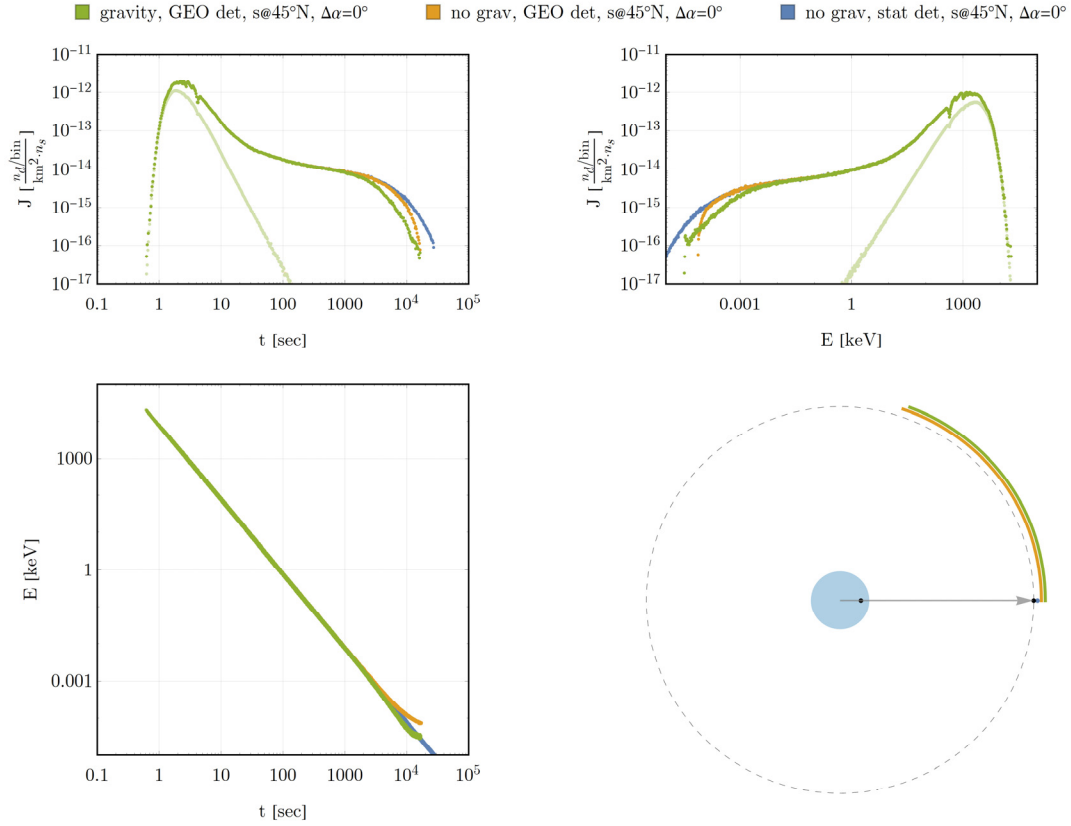
Figure 63: HATS-n time-energy distribution of contributions from a Watt-fission-235 source at 50 km and 45°N to stationary and geostationary detectors at $\Delta\alpha = 0°$ at time of emission without gravity and geostationary detector with gravity.
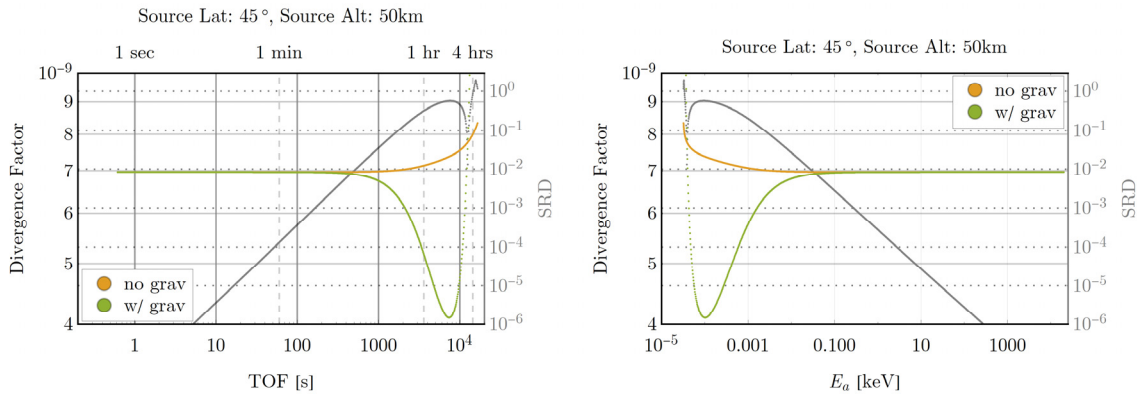
Figure 64: Divergence factor as a function of time of flight and arrival energy from a source at 50 km and 45°N to a geostationary detector at $\Delta\alpha = 0°$ at time of emission with and without gravity.

150
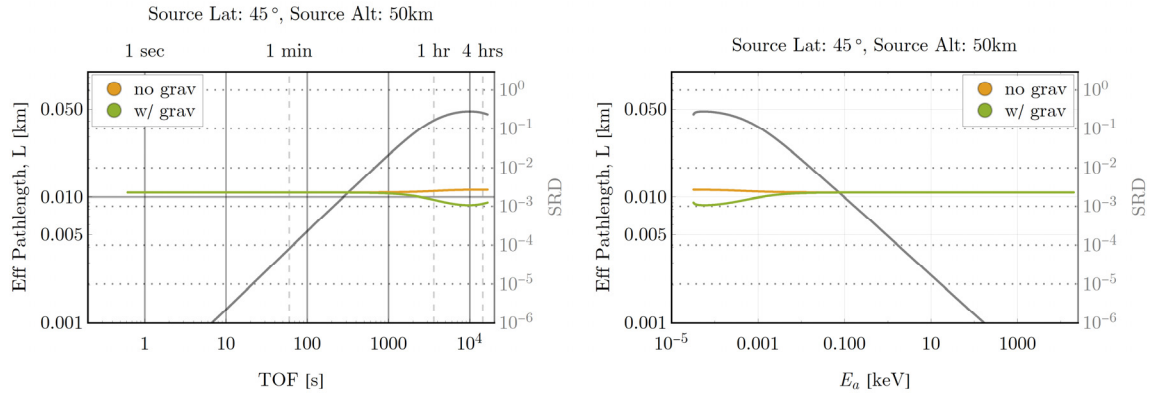
Figure 65: **Effective path length as a function of time of flight and arrival energy from a source at 50 km and 45°N to an overhead geostationary detector at $\Delta\alpha = 0°$ at time of emission with and without gravity.**
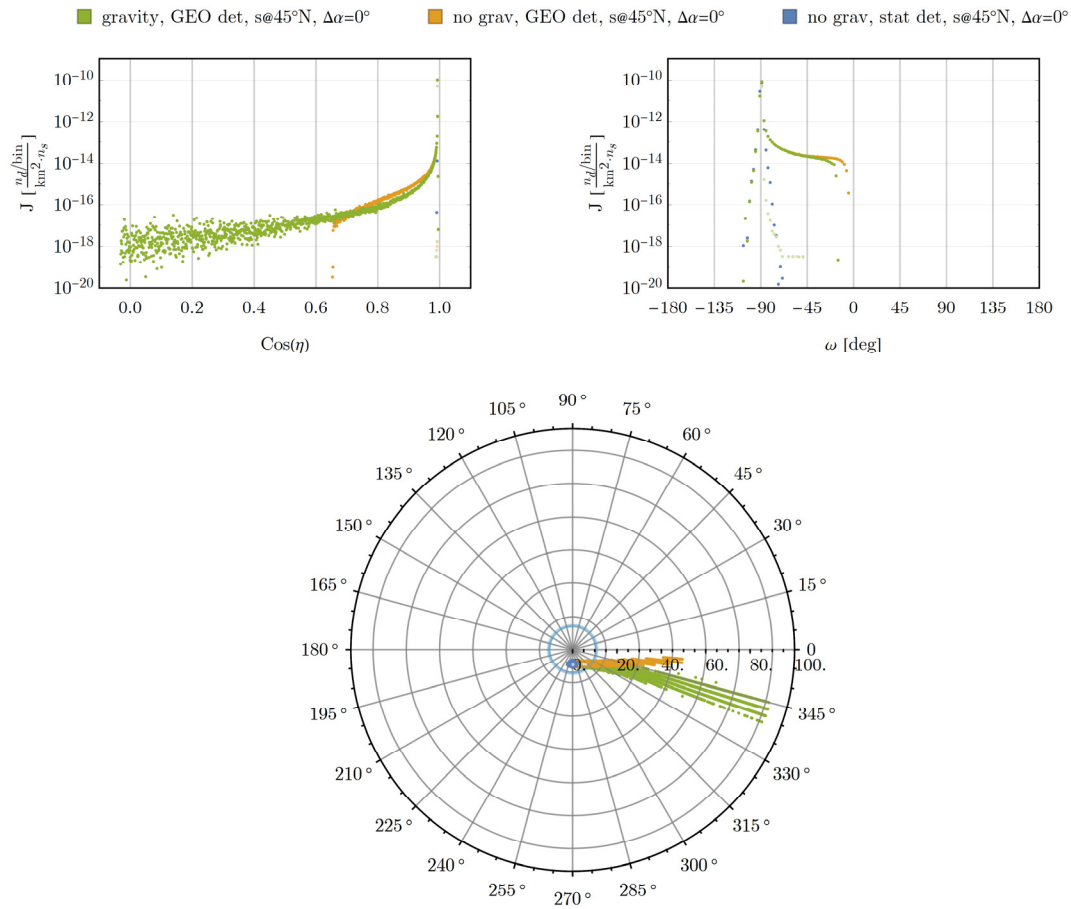
Figure 66: **HATS-n nadir-azimuth distribution of contributions from a Watt-fission-235 source at 50 km and 45°N to overhead stationary and geostationary detectors at $\Delta\alpha = 0°$ at time of emission without gravity and geostationary detector with gravity.**

151

Fidelity of the Atmosphere Model

Continuous vs Discrete Representation

Consider a path from the surface of the earth straight up to 86 km. The EPL in this limiting vertical case is simply

$$L = \int_0^{86} \frac{\rho(z)}{\overline{\rho}} \, dz \,. \tag{75}$$

A combinatorial-geometry approach would model the atmosphere as a set of concentric annuli (e.g., n uniformly-spaced shells in each atmospheric layer) with uniform density. If the uniform density in each shell is chosen to be equal to the density at the center altitude of the layer, this is effectively a composite midpoint approximation to the integral, but only in this vertical case ($\zeta = \pm 1$)
The EPL by this approximation through any layer is

$$\frac{\Delta Z_b}{n} \sum_{i=1}^{n} \frac{\rho(z_i)}{\overline{\rho}} \tag{76}$$

where ΔZ_b is the geometric thickness of the atmospheric layer, n is the number of concentric shells of uniform density, and each z_i is the altitude at the geometric middle of a shell. The precision achieved by this approximation for a vertical path is shown below for various values of n. Also plotted is the precision achieved by application of a Gauss-Legendre n-point quadrature on the full thickness of each layer.
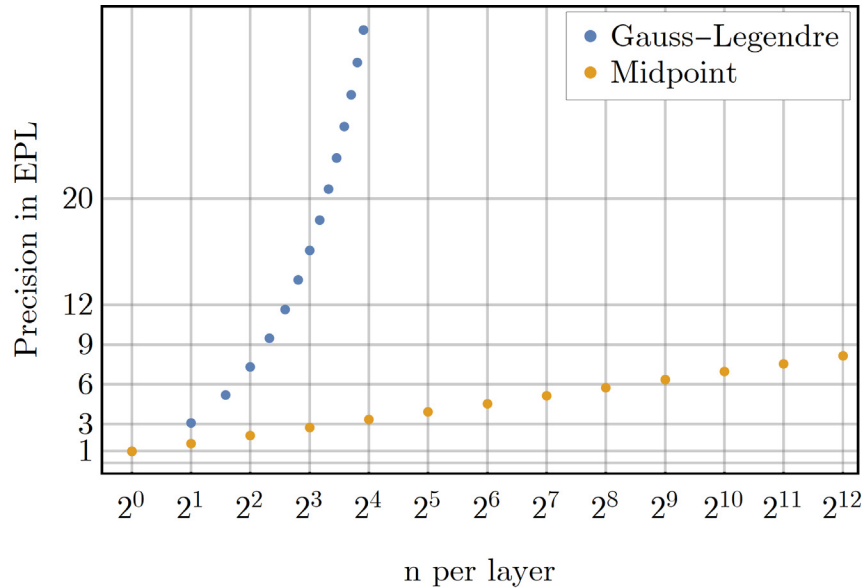
Figure 67: Precision achieved in effective path length computed using discrete constant-density cells (midpoint quadrature) and continuous full layer quadrature (Gauss-Legendre) for vertical paths.

Six digits of precision is achieved in the many-shelled model with 512 shells per layer (3584 shells for the 7 layers of the atmosphere model from the surface up to 86 km), whereas six digits are obtained by application of just one 5-point Gauss-Legendre quadrature in each layer.

Note that this comparison is for a full-thickness effective path length. In the case that the path length is not full thickness (the actual application of the model), the many-shelled representation applies an effectively coarser approximation on the shorter path (although without requiring new evaluations of the density function) resulting in degraded precision. The approach of treating each layer continuously is easily extended to partial layers without degrading precision (but requires evaluation of the density function at each quadrature point for Gauss-Legendre).

For an other than vertical path (still from the surface to 86 km altitude), the effective path length is

$$L = \int_0^S \frac{\rho\big(z(s)\big)}{\overline{\rho}}\, ds = \int_0^{86} \frac{\rho(z)}{\overline{\rho}} \frac{R_\oplus + z}{\sqrt{R_\oplus^2 \zeta_0^2 + 2R_\oplus z + z^2}}\, dz \tag{77}$$

and the many-shelled approximation is

$$L \approx \frac{\Delta Z_b}{n} \sum_{i=1}^{n} \frac{\rho(z_i)}{\overline{\rho}} \frac{R_\oplus + z_i}{\sqrt{R_\oplus^2 \zeta_0^2 + 2R_\oplus z_i + z_i^2}}\,. \tag{78}$$

Performance is degraded by the shape of $ds\,/\,dz$. This is more easily seen by considering the integral with respect to s, because it has the same integrand as in the vertical case. However, if $|\zeta| < 1$, the curvature of the path puts more of the path below the center altitude than above it. To have composite midpoint, the density would have to be evaluated at the center of the s interval along the path through each annulus. This is impractical, so that the quadrature loses the accuracy of a midpoint method. The local truncation error of midpoint quadrature is third order, so that the composite quadrature with fixed limits of integration has order $1\,/\,n^2$ convergence as the grid is refined. However, with the integrand evaluated at off-center points, the local truncation error is only second-order This means that the composite quadrature has order $1/n$ convergence as the mesh is refined. The closer the path is to horizontal, the farther the evaluation points are from the center (in s), and the greater the error.

To show this, Figure 68 adds the precision achieved for various values of n on horizontal ($\zeta_0 = 0$) and nearly horizontal ($\zeta_0 = 0.07$) paths. Note the significant degradation in precision for the many-shelled approach from the vertical case. Note that the continuous layer approach using Gauss-Legendre maintains precision because its local truncation error is tenth order. It is adequate for $\zeta_0 \geq 0.07$ because it captures the shape of the integrand factor $ds \,/\, dz$. However, that factor is singular at $z = 0$ for $\zeta = 0$, requiring another approach for $\zeta < 0.07$.
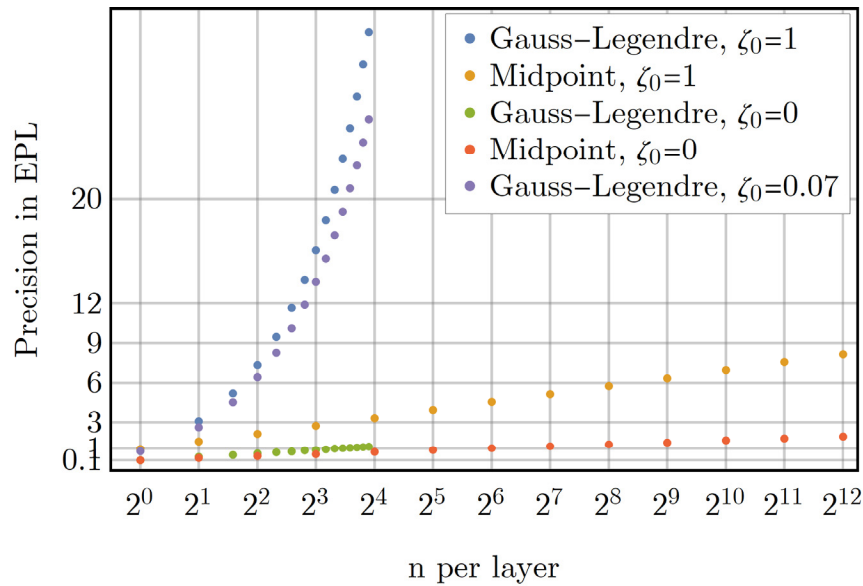
Figure 68: **Precision achieved in effective path length computed using discrete constant-density cells and continuous-density full layer Gauss-Legendre quadrature for vertical and horizontal paths.**

However, note the degraded performance of the Gauss-Legendre quadrature for small ζ_0. In this case ($\zeta_0 \leq 0.07$), the effective path length may be evaluated using the formulation from its definition in (47):

$$L = \int_0^{\Delta s} \frac{\rho\big(z_0 + \Delta z(s)\big)}{\bar{\rho}}\, ds \; .$$

Evaluation of this integral incurs higher computational cost than the formulation integrating over z (mainly because the values of the density function cannot be precomputed), but preserves precision for small ζ_0.

Figure 69 adds the precision achieved for other values of ζ_0 ($\zeta_0 = 0.0001$ and $\zeta_0 = 0.001$) and the better conditioned formula for small ζ_0. The cases for vertical and horizontal bound the effect.
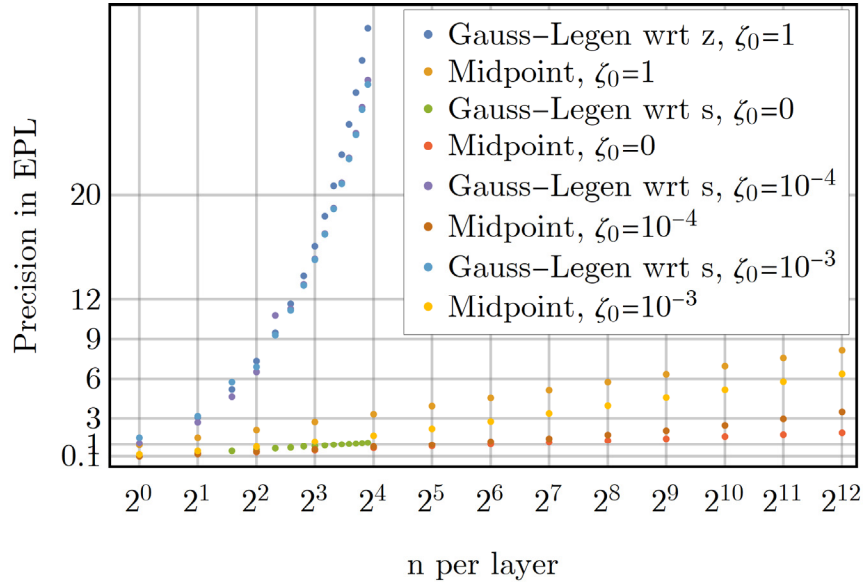
Figure 69: **Precision achieved in effective path length computed using discrete constant-density cells and continuous-density full-layer Gauss-Legendre quadrature for vertical, horizontal, and nearly horizontal paths.**

High Altitude Atmosphere

The EPL on a vertical path from 86 to 1000 km (the top of the turbulently mixed portion of USSA-76) is equivalent to a path length of approximately 3.2

centimeters through sea-level density atmosphere. For a sense of scale at higher altitude, this is approximately equal to a vertical path in the final four kilometers of the atmosphere up to 86 km.

Effective Path Length

The EPL as a function of zenith cosine ζ_0 for various starting altitudes to the top of the extended atmosphere is shown in Figure 70. Except for the extended scale, and addition of higher starting altitudes, this figure is not visibly different from the effective path length plotted without the extended atmosphere in Figure 9. The symmetric relative difference in effective path length when ignoring the extended atmosphere is shown in Figure 71 for paths beginning at 86 km and below.
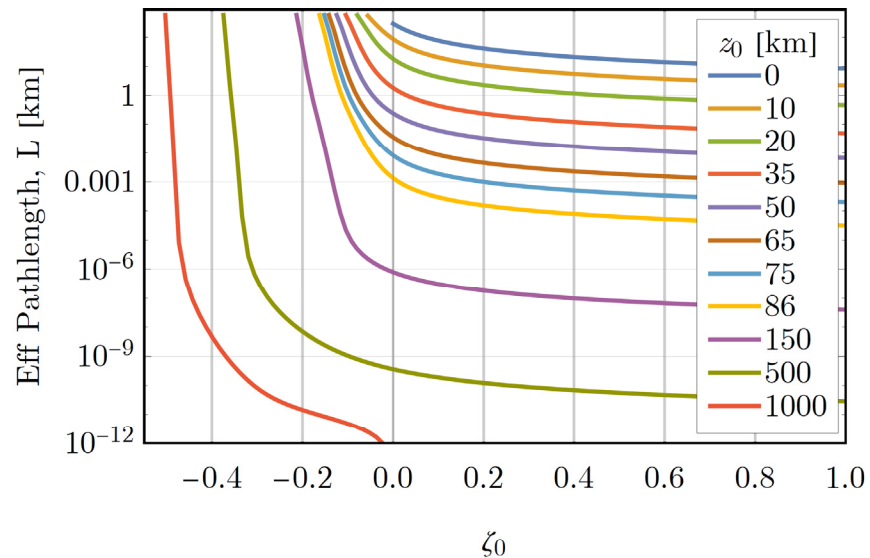
Figure 70: Effective path length to the top of the extended atmosphere (1000 km) for various starting altitudes.
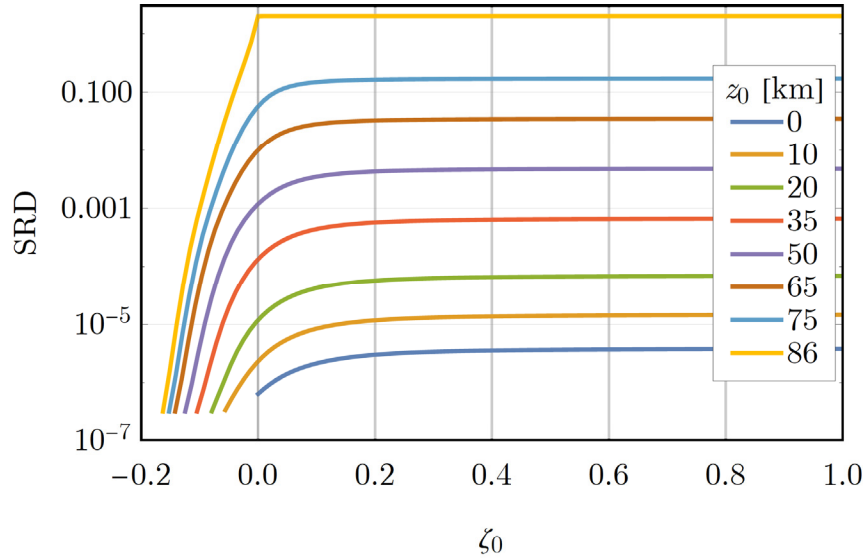
Figure 71: Symmetric relative difference when including the extended atmosphere in effective path length to the top of the extended atmosphere (1000 km) for starting altitudes 86 km and below.

Spatial Distribution of Scatters

The spatial distribution of scatters changes with the extension of the atmosphere model, but due to the highly rarified atmosphere at these altitudes, the probability of scatters occurring in this region is small. Further, for a distant detector (e.g. a detector in geostationary orbit), the change in the size of the view of the earth due the additional thickness of the extended atmosphere is also small.

Atmospheric Constituents

Relative error in total interaction cross section for the atmosphere is shown in Figure 72. Across the full range of energies, five good digits in the total cross section for the atmosphere is achieved by including the eight most abundant

isotopes in the atmosphere from Table 4. Note that the SRD increases upon addition of the sixth atmospheric constituent (^{12}C). This is due to the larger relative cross section of ^{12}C relative to the other constituents (being added to the model in order of abundance, *not* in order of increasing interaction cross section). This presents an interesting dilemma for the choice of constituents for the atmosphere representation: While a particular constituent may be more rare than others, its contribution to the total interaction cross section for the atmosphere could be of a greater magnitude (and vice versa).
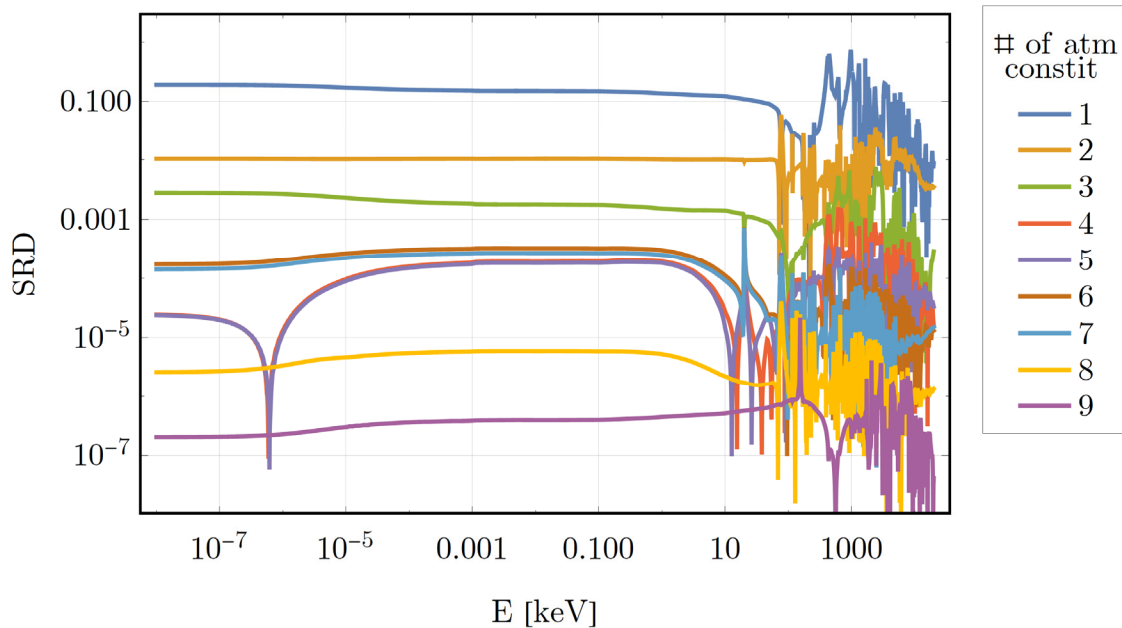
Figure 72: **Relative error in total atmospheric cross section for various numbers of included atmospheric constituents.**

X. Summary

Relative Motions

The influence of relative motions on the problem is considerable and the changes required to include it in the transport calculations are not trivial. Detector motion requires a new procedure to solve the rendezvous problem, and the properties of any neutron rendezvous with the detector are influenced. Figure 73 shows the symmetric relative difference as a function of time of flight for the properties of neutron rendezvous (emission energy, arrival energy, emission zenith cosine, arrival nadir cosine, divergence factor, and effective path length) with and without detector motion. The SRD generally increases, for all the properties of the rendezvous, with increasing time of flight to the detector. Accounting for detector motion also introduces the possibility that a clear line of sight to the detector becomes obstructed by the earth (or vice versa) during the time scale of the problem. This introduces two special cases not accounted for when motion of the detector is ignored: The rising detector with obstructed line of sight at time of emission that comes into view during the time scale of the problem, and the setting detector with clear line of sight at time of emission that drops out of view during the time scale of the problem.
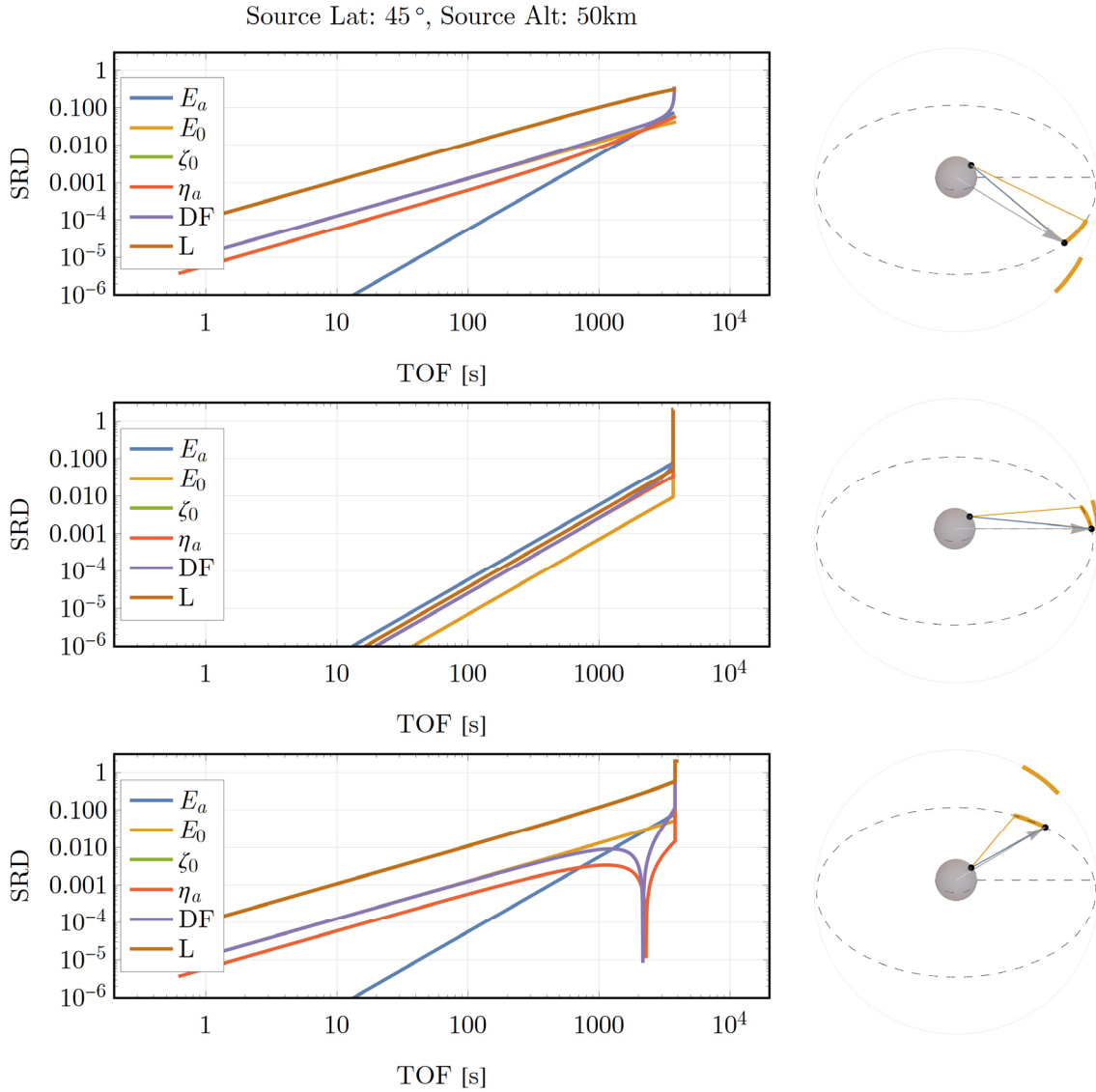
Figure 73: Symmetric relative difference (SRD) in properties of neutron rendezvous as a function of time of flight to a geostationary detector with and without detector motion (without gravity) for source-detector orientations with line of sight.

Calculation of the divergence factor is changed to account for motion of the emission location (velocity of the source at the moment of emission or of the center of mass in a scatter) which changes the effective distance from the emission to the detector and motion of the detector which changes the effective

area of the detector for the intercept. The calculation of optical thickness along a trajectory through the atmosphere is changed because the atmosphere rotates in the ECI frame in which the neutron trajectory is fixed. Particles in the transport medium (the atmosphere) undergo random thermal motion and bulk motion due to rotation of the earth. The influence of random thermal motion on interaction cross sections is accounted for by Doppler broadening the cross sections, but also contributes variance to the scattering kinetics calculations performed during the transport due to the contribution of an atmospheric particle's kinetic energy to the total energy available in the system (that is a scatter). Bulk motion of the transport medium is generally smaller than other velocities considered in the transport calculation, but is of concern because errors introduced in the path-length calculations by ignoring it are systematic. Motion of the source is not negligible in the context of the air-to-space neutron transport problem and can greatly influence the population of low-energy neutrons able (or unable) to intercept the detector. This effect is increased by the inclusion of gravity.

Gravity

The influence of gravity on the transport problem is profound, especially when combined with detector motion; including gravity requires considerable procedural changes to the transport calculation. To account for gravity, the rendezvous problem is solved using the same procedure as described for the

rendezvous problem with detector motion with the exception that each stage of

the solver includes solving an orbital targeting problem known as Lambert's

problem. The rendezvous properties of neutrons intercepting the detector change

even more considerably when accounting for gravity than when adding motion of

the detector. Figure 74 shows the symmetric relative difference as a function of

time of flight for the properties of neutron rendezvous (emission energy, arrival

energy, emission zenith cosine, arrival nadir cosine, divergence factor, and

effective path length) with and without gravity. The SRD generally increases, for

all the properties of the rendezvous, with increasing time of flight to the detector.

The rendezvous problem is further impacted when accounting for gravity by the

fact that a clear line of sight to the detector is no longer a requisite to achieve a

clear flight path to the detector: With gravity, neutrons may follow orbital

trajectories *around* the earth, or *over* the horizon to intercept a detector that has

no view of the emission location. Solutions partially or fully ignored by a

transport calculation that does not account for gravity are the rising and setting

detector cases, the special setting case with a temporal interruption of a clear

flight path to the detector, polar and other high latitude sources, and detectors

on the side of the earth opposite the source.
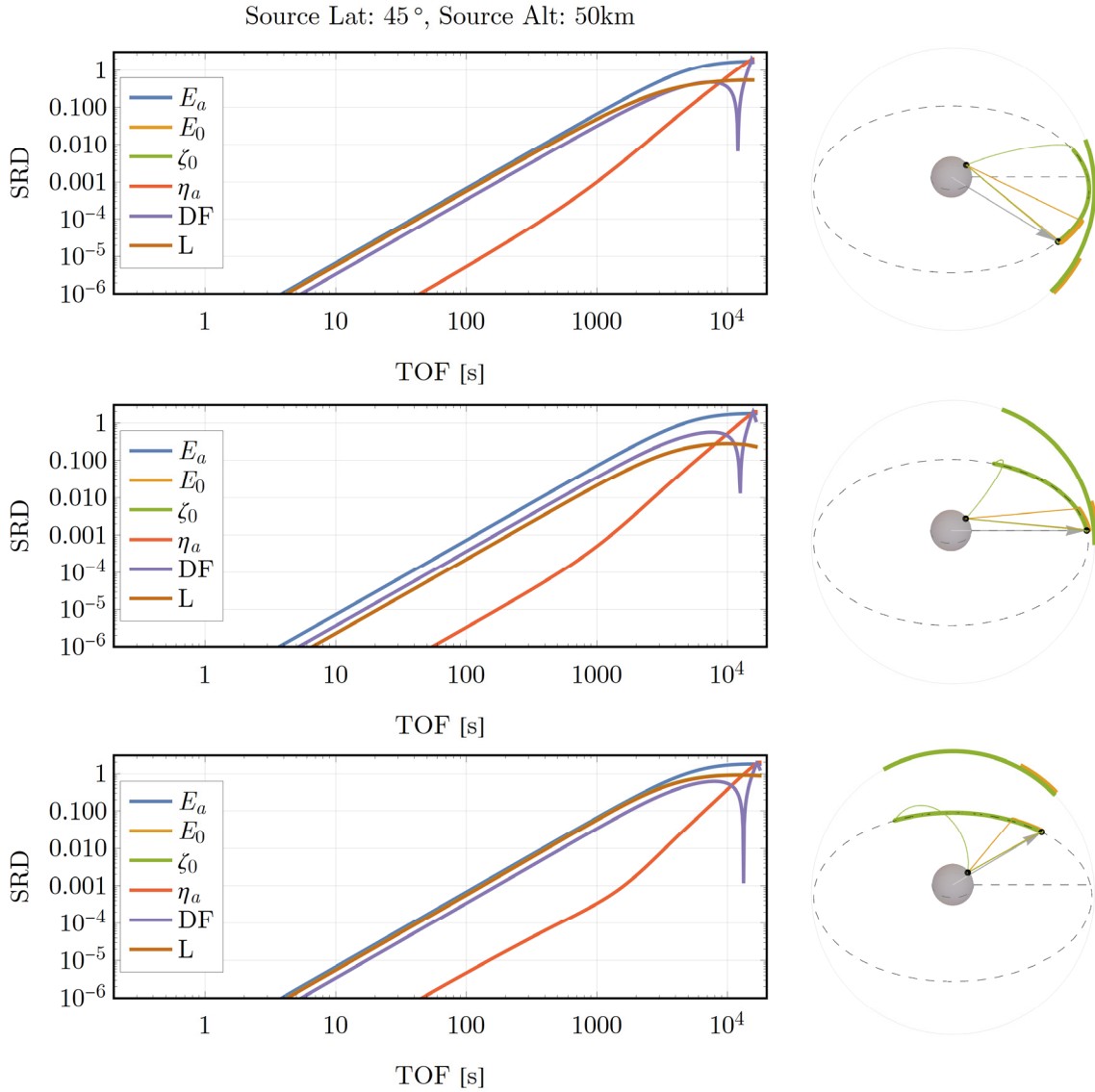
Figure 74: **Symmetric relative difference (SRD) in properties of neutron rendezvous as a function of time of flight to a geostationary detector with and without gravity for source-detector orientations with line of sight.**

As with relative motions, the formulation of the divergence factor changes when accounting for gravity. I chose to empirically estimate the divergence factor by applying a shooting algorithm as an alternative to direct computation, which would require handing the many special geometric and numerically-sensitive cases

that arise. The optical thickness through the atmosphere also requires new formulations to account for the shape of an orbital trajectory through the atmosphere, but the general approach to computing effective path lengths remains unchanged except for the new formulae.

Fidelity of the Atmosphere Model

Fidelity of the atmosphere model drives both accuracy and overhead computational cost of computation for the air-to-space transport problem. It is essential to incorporate the continuous variation of the atmosphere density in order to compute the required path-length integrals with accuracy and precision. Approaches that discretize the atmosphere model into layers of uniform density introduce errors in the path-length calculations. The addition of a high-altitude atmosphere to the model influences the path-length calculations and the geometric distribution of scatters, but these effects are small due to the highly rarefied atmosphere at high altitudes. The number of atmospheric constituents included in the atmosphere influences the interaction cross sections and the kinetics of scatters during the transport calculation. Similar to the influence of thermal motion of atmospheric nuclei, the influence on cross sections can be accounted for, but the influence of the different scattering kinetics of rare atmospheric constituents introduces variance into the result of the transport calculation.

Radioactive Decay

The radioactive decay of free neutrons is not negligible on the time scale of solutions to air-to-space transport problems. The effect of radioactive decay should also not (if possible) be applied to binned estimates as a post-processing effect as this introduces discretization error. Given the trivial cost of adjusting each computed contribution for radioactive decay between neutron emission and rendezvous with the detector, radioactive decay of free neutrons should be accounted for at each next-event arrival during the transport calculation.

Ranges of Influence

The most profound influences found in the air-to-space neutron transport problem result from detector motion and gravity. In general, detector motion and gravity have little influence on high energy and short time of flight ranges of the transport problem in the context of the time-energy and direction distributions of neutrons at the detector. The influence grows, but remains small, for moderate energies and middle times of flight. For low energy and long times of flight, the influence of relative motions and gravity is profound in both the time-energy and direction distributions of neutrons as seen by the detector.

Missing Solutions

In addition to the time-energy and direction distribution ranges over which the influence of relative motions and gravity is considerable, the special cases introduced (rising & setting detector geometry, temporal interruption of a clear flight path, detectors behind the earth, and polar or other high latitude sources) demonstrate features of solutions, *and even the existence of entire sets of solutions*, that are lost when the special features of the air-to-space neutron transport problem are not included in a transport code.

Source Velocity

Additionally, the velocity of the source should always be included in transport computations for the air-to-space problem in two ways. (1) Depending on the directions of the source velocity and of the emitted neutron velocity, it adds or subtracts energy from the emitted neutron (in the ECI frame). Because of gravity, this energy determines whether the neutron can reach the detector. The energy distribution of emitted neutrons falls rapidly with decreasing energy at low energies. Therefore, the population of neutrons able to reach the detector becomes dependent on emission direction. (2) The velocity of the source is required for the calculation of correct divergence factors for first-flight neutrons arriving at the detector With the trivial computational cost of including source

167

motion, there is little justification for its exclusion from any model for the air-to-space neutron transport problem.

Special Features Contributing Variance

When conducting a Monte Carlo study of a given problem, it is not only the expectation value that is of interest, but also the variance of the estimate obtained by the simulation. The variance in the estimate can be attributed to two general sources: First, *simulation variance*, or variance as a result of the Monte Carlo process of sampling a finite number of histories to estimate the behavior of a system. Second, and relevant to this discussion, is *physical variance* or variance introduced to the estimate because physical processes modeled in the simulation themselves have variance. Two of the special features of the air-to-space transport problem that were investigated during this research fall into this category: The effect of thermal motion of particles in the atmosphere and the effect of rare atmospheric constituents on scattering kinematics. The influence of thermal motion and rare atmospheric constituents on the expectation value estimated by a Monte Carlo simulation of the air-to-space neutron transport problem is small. However, if the variance of the estimate is of interest (for study or if a specific certainty needs to be achieved), these features need to be included in the simulation to fully characterize the variance of any estimate obtained.

The HATS-n Code

The High-Altitude Neutrons to Space (HATS-n) code developed in support of this research is a well-designed and appropriately targeted tool for continuing investigation of the air-to-space neutron transport problem. It is important to remember that when considering this class of problems, approaches that discretize the atmosphere into constant-density cells should be avoided. These approaches introduce high computational overhead (for raytracing) by complicating the otherwise trivial problem geometry and introduce considerable error in the evaluation of density integrals through the atmosphere to determine optical thickness. While codes like HATS-n and HASTEN may not be appropriate for all research questions posed for the air-to-space class of problems, it is the opinion of the author that at the time of this writing, there are no other codes or tool available to the transport community that perform adequately in accuracy, precision, or computational speed for the air-to-space neutron transport class of problems.

XI. Conclusions

The objective of this research was to *identify*, *characterize*, and *quantify* influences of the special features of the air-to-space neutron transport problem to provide information on features that should be included in a Monte Carlo simulation to enhance fidelity for yet-to-be-specified applications. A secondary goal was to *demonstrate* the influence of these special features in the context of a Monte Carlo code. The research objectives were met. Special features in the areas of relative motions, gravity, and fidelity of the atmosphere model were identified and described, and then investigate to the extent necessary to quantify them or add them to the HATS-n code product. Considerable effort was spent developing well-conditioned and efficient methods for solving various portions of the problem, both in the context of the special features and the context of the air-to-space problem as a whole.

The special features of the air-to-space neutron transport problem investigated and demonstrated during this research have considerable influence on the transport calculations required for analysis of the problem. Some influences (detector motion, gravity) introduce additional, sometimes considerable, computational effort and complexity to the otherwise simple process for the Monte Carlo estimator for neutron current as seen by a satellite-based detector. However, the influence of these features is such that they need to be included as part of the baseline set of assumptions to the problem (in contrast to

the traditional set of neutron transport assumptions in which they are ignored). Should a transport problem be posed in which only high energy and early time neutrons are of interest, it is possible that increased computational speed could be a suitable justification for neglecting the effects of detector motion and gravity. However, for the general class of air-to-space neutron transport problems, the range of neutron energies and times of flight is such that the effects of the special features of the problem (detector motion and gravity included) *cannot be ignored.*

Other special features of the problem, such as source motion and radioactive decay of free neutrons, may or may not have a significant influence on the problem (depending on the energy and time scales to which the problem is restricted), but the computational cost of including these features is so trivial that any effort invested in justifying their inclusion is simply wasted. Similarly, thermal motion of atmospheric nuclei and rare atmospheric constituents influence the variance of any estimate obtained from the simulation at a largely trivial computational cost. In most cases, the variance of any estimate obtained via a Monte Carlo simulation is of interest, so these features should also be included. Finally, the accuracy, precision, and computational efficiency of the calculation of path-length integrals is a cornerstone of any Monte Carlo approach to the air-to-space neutron transport problem. These integrals are not adequately approximated by approaches that discretize the atmosphere into layers of uniform density. Any approach to the air-to-space neutron transport problem

171

should treat the variation of atmospheric properties with altitude continuously. This results in both more correct and more computationally-efficient calculation of the path-length integrals.

Appendix A. Overview of the HATS-n Code

The HATS-n code is a purpose-built Monte Carlo code written in modern Fortran to simulate the transport of neutrons from a source in the atmosphere to a distant detector in space. The HATS-n code was initially a branch of the HASTEN code developed by Professor Kirk Mathews at AFIT. The HASTEN code is a research tool developed to test various flux-at-a-point estimators in the context of the air-to-space neutron transport problem.

Commonality with HASTEN

Although initially developed as a branch of the HASTEN project, the current HATS-n shares very little code with the original HASTEN. The main program and other routines for executing neutron histories and accumulating results is largely common between the projects (although no effort has been made to maintain commonality, so the similarities are largely procedural rather than actual interchangeable code), as well as some of the low-level support routines and modules. However, the majority of the code required to perform any step within a neutron history has been revised or replaced to account for the special features of the problem explored during the course of this research. Additionally, significant revisions were made throughout the common and revised code targeting implementation on massively parallel architectures.

Target Architecture

The HATS-n Fortran code is targeted for implementation on a massively parallel shared memory architecture: Specifically the Intel® Xeon Phi™ x100 series of coprocessors as a natively executed coarray Fortran application. The available computing hardware for development and testing was an Intel® Xeon Phi™ x100 31S1P coprocessor capable of hosting 228 parallel images with 8 gigabytes of shared memory. This imposes a memory limit of approximately 30 megabytes per image during execution (in general, small for a neutral particle transport simulation). The memory limit could be relaxed with incorporation of shared variables, but tuning of parallel performance of the application was not pursued in this research. The memory footprint of the code was reduced by using variable length lists in place of large arrays and by storing minimally processed cross section data. The trade for the small memory footprint is increased overhead in list management and the computational cost of interpolating and reconstructing interaction cross sections throughout the simulation.

Program synchronization and data sharing is implemented as a single program multiple data (SPMD) approach of fully independent program images with no shared variables during the generation of histories. Shared problem setup data is distributed to each image during the setup phase of the program. Each image then runs an assigned number of neutron histories and writes the raw results to disk. Once all images have completed the assigned work, a single image merges, processes, and outputs the results from the entire set of images.

Modules and Descriptions

1. HASTE DRIVER: Main program. Manages setup, running histories, and processing results as well as synchronization and sharing during SPMD execution.

2. Results: Contains routines for reading/writing raw image tallies and results, merging individual image results, and writing final results to file.

3. MC Neutron: Contains routines necessary for execution of a single neutron history: emission, raytracing, scattering, next-event estimation, and killing. Contains type definition for collection of variables defining a neutron in the phase space.

4. Find Trajectory: Routines for determining a trajectory from an emission point to a detector. Depending on problem setup inputs, solves the rendezvous problem ignoring or accounting for gravity and ignoring or accounting for relative motions.

5. Detectors: Contains routines for definition and setup of the detector object, as well as receiving and recording of tallies in the detector grid.

6. Tallies: Contains routines for definition, setup, and management of the time-energy-direction grid that is part of a detector object.

7. Neutron Scatter: Routines for sampling or setting properties of neutron interactions, computing per- and post- scatter quantities. Also contains type definitions for collections of variables defining the scatter model and next interaction properties.

8. Target Motion: Contains routines for sampling the velocity of the target particle due to thermal motion and combining with rotational atmosphere and wind velocities.

9. Path Lengths: Routines for tracing the geometry and optical thickness of rays through the atmosphere: point and altitude of

closest approach, distance to edge of the scattering medium, effective path length (with and without gravity), and line of sight checks.

10. Satellite Motion: Routines used by detector object to determine position and velocity of the detector given simulation time.

11. Divergence: Routines to compute divergence factor (with and without gravity) accounting for relative motion of the emission point and the detector during the flight of a neutron from emission to the detector.

12. Astro Utilities: Contains routines for astrodynamics calculations for determining properties of orbital trajectories and solving orbit propagation (Kepler's) and orbit determination (Lambert's) problems.

13. Setups: Routines for reading and processing estimator input and problem definitions.

14. Sources: Contains routines for definition and setup of the neutron source object, as well as distributions and sampling of emission energies.

15. Random Directions: Routines for sampling scattered directions and determining the constrained scattering angles to achieve rendezvous trajectories.

16. Cross Sections: Routines and type definitions for reading and storing raw ENDF cross section data. Routines for reconstructing pointwise cold or broadened cross sections given energy of the incident neutron and temperature of the scattering medium.

17. Neutron Utilities: Routines for computing properties of the neutron in the phase space.

18. Atmospheres: Interface routines to make atmospheric properties of a continuous atmosphere model available to other modules. Also contains type definitions and setup routines for the atmosphere object and generic atmosphere models (isothermal-exponential, linear, uniform).

19. Statistics: Statistics routines for processing tallies into results.

20. Global: Contains fundamental and derived constants used throughout the code.

21. US Std Atm 1976: Routines and functions to compute temperature, pressure, density, and composition as functions of altitude according to the 1976 U.S. Standard Atmosphere.

22. Interpolation: Interpolation routines mainly used in interpolating ENDF cross sections (linear-linear, linear-log, log-linear, log-log, histogram).

23. Legendre Utilities: Routines for evaluation of Legendre expansion angular distributions for scattered directions.

24. Sorting: Routines for sorting lists.

25. Random Numbers: Random number generators, specifically from the Intel® Math Kernel Library™ (MKL). Provides faster generators with better properties than the intrinsic random number generators, as well as a selection of independent random number generators specifically designed for parallel applications.

26. FileIO Utilities: Support routines for creating, modifying, deleting files and folders and/or dumping and reading variables to/from unformatted files.

27. Utilities: Support routines performing general mathematical or commonly used computational tasks (quadratic roots, cross products, vector length, bisection search, etc.)

28. Kinds: Contains parameter definitions for Fortran kind selections for consistent typing (single, double, quad, etc.) of Reals and Integers.

Appendix B. Summary of U.S. Standard Atmosphere 1976

The relevant information, equations, and data from the 1976 U.S. Standard Atmosphere (NOAA, NASA, USAF, 1976) are reviewed here for easy reference and also to document minor changes and assumptions in the implementation of the model for application to the transport problem. Further, relevant tables and plots are reproduced (in part or in whole) to provide a local reference and verification of interpretation because of poor readability in the original reference. Relevant physical constants used in the model are listed in Table 5. Values of the constants listed in Table 5 may have been refined since the publication of the atmosphere model, but the original values are used (for implementation of the atmosphere model) to maintain consistency with the original publication. Further, only the portions of the model are included which are required to compute atmospheric temperature, density, and fractional composition as a function of altitude as these are the only relevant quantities for the scope of the research problem.

Constant	Symbol	Value
earth radius	$R_\oplus$	6356.766 km
Acceleration due to gravity at sea level	g_0	9.80665 m/s^2
Gas constant	R^*	8.31432$\times$10^3 N·m/(kmol·K)
Mean molecular weight of sea level air	M_0	28.9644 kg/kmol
Avogadro constant	N_A	6.022169$\times$10^{26} kmol^{-1}

Sea Level to 86 kilometers

Below 86 km, the atmosphere is divided into seven layers in which the scale is considered by geopotential height instead of geometric altitude. Geopotential height H is related to geometric altitude Z by

$$H = \frac{R_\oplus Z}{R_\oplus + Z} \qquad (79)$$

(NOAA, NASA, USAF, 1976, p. 8). For geometric altitude expressed in kilometers (km), the corresponding geopotential height has units of kilometers′ (km′).

Temperature

The molecular temperature of the atmosphere in each layer is given by

$$T(H) = f_M(Z)\left(T_b + L_b\left(H - H_b\right)\right) \tag{80}$$

where T_b is the temperature at the base of the layer, L_b is the lapse rate, H_b is the geopotential height at the base of the layer, and

$$f_M(Z) = \left(1 - 2\left(Z - Z_{i-1}\right)\right)\left(M_0\Big/M\right)_{i-1} + 2\left(Z - Z_{i-1}\right)\left(M_0\Big/M\right)_i \tag{81}$$

is the interpolated ratio of atmosphere mean molecular weight at sea level to the mean molecular weight at the geometric altitude Z corresponding to geopotential height H (NOAA, NASA, USAF, 1976, pp. 9-10). Values for T_b, L_b, and H_b are listed in Table 6. Values for Z_i and $(M_0 / M)_i$ on which to interpolate for f_M are listed in Table 7. The molecular temperature from sea level to 86 km geometric altitude is plotted in Figure 75.

Table 6: Reference levels and temperature lapse rates (NOAA, NASA, USAF, 1976, p. 3), and computed base temperatures and pressures from the surface to 86 geometric kilometers.

Sub-script b	Geopotential Height (km′) H_b	Lapse Rate (K/km′) L_b	Base Temp (K) T_b	Base Pressure (N/m²) P_b
0	0	-6.5	288.15	101325
1	11	0.0	216.65	22632.0336239
2	20	1.0	216.65	5474.87437676
3	32	2.8	228.65	868.014988511
4	47	0.0	270.65	110.905629144
5	51	-2.8	270.65	66.9384346264
6	71	-2.0	214.65	3.9563844998

Table 7: Molecular weight ratio for various geopotential heights and geometric altitudes.
(NOAA, NASA, USAF, 1976, p. 9)

Geometric Altitude (km) Z_i	$\left(\dfrac{M_0}{M}\right)_i$
≤ 80.0	1.000000
80.5	0.999996
81.0	0.999989
81.5	0.999971
82.0	0.999941
82.5	0.999909
83.0	0.999870
83.5	0.999829
84.0	0.999786
84.5	0.999741
85.0	0.999694
85.5	0.999641
86.0	0.9995788
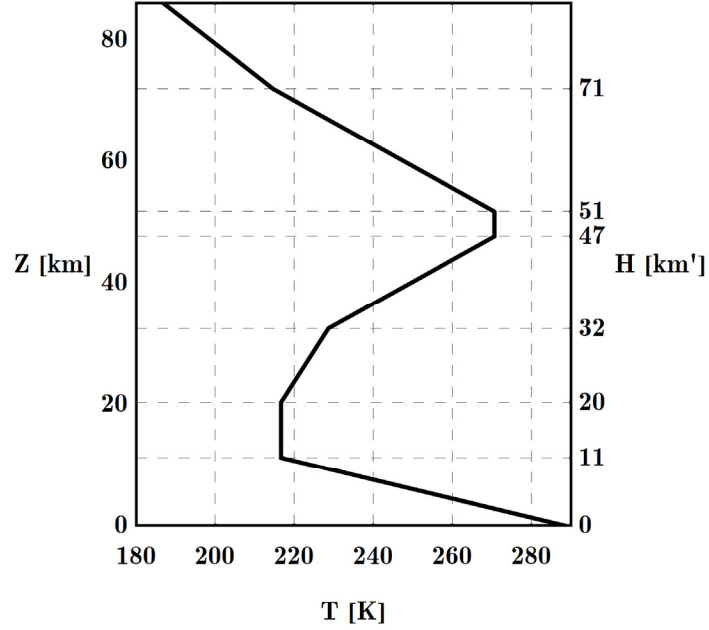
Figure 75: Temperature as a function of geometric altitude below 86 km.

Density

The atmospheric pressure (necessary for computing density) in each layer is

$$P(H) = \begin{cases} P_b \left(\dfrac{T_b}{T(H)} \right)^{\left(\frac{g_0' M_0}{R^* L_b} \right)} & L_b \neq 0 \\[2em] P_b e^{\left(-\frac{g_0' M_0 \left(H - H_b \right)}{R^* T_b} \right)} & L_b = 0 \end{cases} \tag{82}$$

where P_b is the pressure at the base of the layer (NOAA, NASA, USAF, 1976, p. 12). Computed values for P_b are listed in Table 6. The atmospheric pressure from sea level to 86 km geometric altitude is plotted in Figure 76.

182
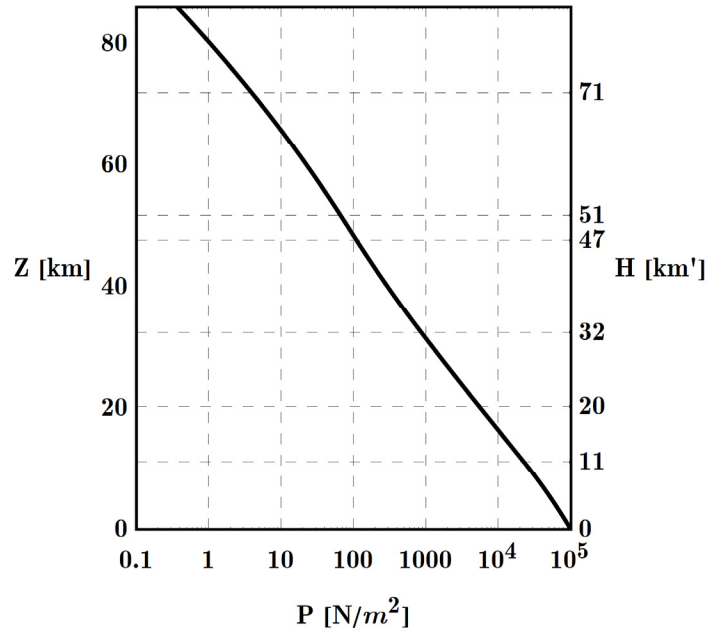
Figure 76: Atmospheric pressure as a function of geometric altitude below 86 km.

The atmospheric density may then be computed by

$$\rho(H) = \frac{M_0}{R^*} \frac{P(H)}{T(H)} \tag{83}$$

(NOAA, NASA, USAF, 1976, p. 15). The atmospheric pressure from sea level to 86 km geometric altitude is plotted in Figure 77.

183
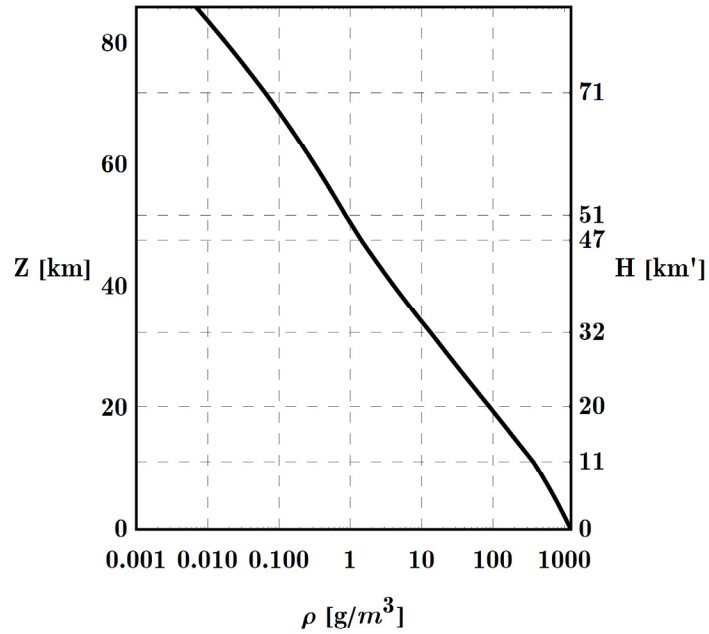
Figure 77: Atmospheric density as a function of geometric altitude below 86 km.

Composition

Below 86 km geometric altitude, the atmosphere may be considered homogeneously mixed with relative fractions of constituents constant from sea level as listed in Table 8 (NOAA, NASA, USAF, 1976, p. 3).

Table 8: Molecular weights and fractional volumes for constituents of sea level atmosphere.
(NOAA, NASA, USAF, 1976, p. 3)

Species	Molecular Weight (kg/kmol)	Fractional Volume F_i
N_2	28.0134	0.78084
O_2	31.9988	0.209476
Ar	39.948	0.00934
CO_2	44.00995	0.000314
Ne	20.183	0.00001818
He	4.0026	0.00000524
Kr	83.80	0.00000114
Xe	131.30	0.000000087
CH_4	16.04303	0.000002
H_2	2.01594	0.0000005

Above 86 kilometers

Above 86 km geometric altitude, the atmosphere is modeled in five main layers scaled by geometric altitude.

Temperature

Atmospheric temperature as a function of geometric altitude above 86 km is given by

$$T(Z) = \begin{cases} T_b + L_b\left(Z - Z_b\right) & b = 7,9 \\[2ex] T_c + A\sqrt{1 - \left(\dfrac{Z - Z_8}{a}\right)^2} & b = 8 \\[3ex] T_{12} - \left(T_{12} - T_{10}\right)e^{-\frac{L_9\left(Z - Z_{10}\right)\left(R_\oplus + Z_{10}\right)}{\left(T_{12} - T_{10}\right)\left(R_\oplus + Z\right)}} & b \geq 10 \end{cases} \qquad (84)$$

where

$$T_c = \frac{T_9\left(L_9\left(Z_9 - Z_8\right) - T_9\right) + T_8^2}{L_9\left(Z_9 - Z_8\right) + 2\left(T_8 - T_9\right)} \cong 263.190647$$

$$A = T_8 - T_c \cong -76.32348$$

$$a = \frac{A\left(Z_9 - Z_8\right)}{\sqrt{A^2 - \left(T_9 - T_c\right)^2}} \cong -19.942882$$

(NOAA, NASA, USAF, 1976, pp. 10-11). Values for T_b, L_b, and Z_b are listed in Table 9. The atmospheric temperature from sea level to 500 km geometric altitude is plotted in Figure 78.

The derivative of temperature with respect to geometric altitude will also be required to compute number densities of species for the density calculations that follow

$$\frac{dT(Z)}{dZ} = \begin{cases} L_b & b = 7,9 \\[2em] -\dfrac{\dfrac{A}{a}\left(\dfrac{Z - Z_8}{a}\right)}{\sqrt{1 - \left(\dfrac{Z - Z_8}{a}\right)^2}} & b = 8 \\[3em] L_9\left(\dfrac{R_\oplus + Z_{10}}{R_\oplus + Z}\right)^2 e^{-\frac{L_9\left(Z - Z_{10}\right)\left(R_\oplus + Z_{10}\right)}{\left(T_{12} - T_{10}\right)\left(R_\oplus + Z\right)}} & b \geq 10 \end{cases} \qquad (85)$$

(NOAA, NASA, USAF, 1976, pp. 10-11).

Table 9: Reference levels, function designations, and base temperatures for the atmosphere above 86 km geometric altitude (NOAA, NASA, USAF, 1976, p. 4)

Sub-script b	Geometric Altitude (km) Z_b	Lapse Rate (K/km) L_b	Functional Form	Base Temp (K) T_b
7	86	0.0	linear	186.867167
8	91	----	elliptical	186.867167
9	110	12.0	linear	240
10	120	----	exponential	360
11	500	----		999.235602
12	1000	----		1000

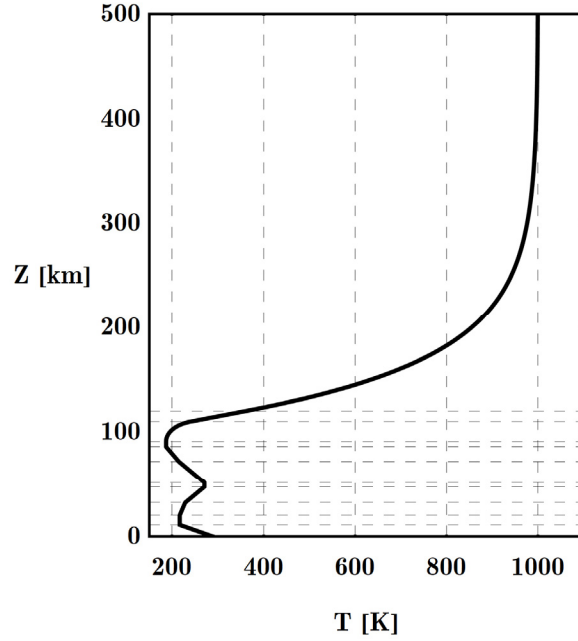**Figure 78: Temperature as a function of geometric altitude up to 500 km.**

Density

Atmospheric density above 86 km geometric altitude is

$$\rho(Z) = \frac{\sum M_i n_i(Z)}{N_A} \tag{86}$$

where M_i is the molecular weight of the i-th species and $n_i(Z)$ is the number density of the i-th species at geometric altitude Z (NOAA, NASA, USAF, 1976, p. 15). Values for M_i are listed in Table 10.

Table 10: Molecular weights and reference number densities for atmospheric constituents above 86 km geometric altitude. (NOAA, NASA, USAF, 1976, p. 13)

Sub-script i	Species	Molecular Weight (kg/kmol) M_i	Reference ($Z = 86$ km) Number Density (m⁻³) n_i^{86}	Background gas count k_i
1	N_2	28.0134	1.129794×10^{20}	1
2	O	15.9994	8.6×10^{16}	1
3	O_2	31.9988	3.030898×10^{19}	1
4	Ar	39.948	1.351400×10^{18}	3
5	He	4.0026	7.5817×10^{14} *	3
6	H	1.00794	$n_6^{500} = 8.0 \times 10^{10}$	5

* This value is incorrectly listed as 7.5817×10^{10} in Table 9 of the U.S. Standard Atmosphere 1976 publication (NOAA, NASA, USAF, 1976, p. 13). The value used here was chosen to agree with plotted and tabulated data from the same reference and confirmed in Table 2 of (NASA, 1976, p. 10) which is the source document for the primary reference for the atmosphere model.

Values of $n_i(Z)$ for all species except molecular Nitrogen $(i = 1)$ and atomic Hydrogen $(i = 6)$ are computed from

$$n_i(Z) = n_i^{86} \frac{T_7}{T(Z)} e^{-\int_{Z_7}^{Z} \left(f_i(Z) + h_i(Z) \right) dZ} \tag{87}$$

where

$$f_i(Z) = \frac{g(Z)}{R^* T(Z)} \frac{D_i(Z)}{D_i(Z) + K(Z)} \left[M_i + \frac{\bar{M}_i(Z) K(Z)}{D_i(Z)} + \frac{\alpha_i R^*}{g(Z)} \frac{dT(Z)}{dZ} \right] \tag{88}$$

$$g(Z) = g_0 \left(\frac{R_\oplus}{R_\oplus + Z} \right)^2 \tag{89}$$

$$D_i(Z) = \frac{a_i}{\sum\limits_{j=1}^{k_i} n_j(Z)} \left(\frac{T(Z)}{273.15} \right)^{b_i} \tag{90}$$

$$K(Z) = \begin{cases} 1200 & 86 \leq Z < 95 \\ 1200e^{1-400/\left[400-\left(Z-95\right)^2\right]} & 95 \leq Z < 115 \\ 0 & 115 \leq Z < 1000 \end{cases} \tag{91}$$

$$\bar{M}_i(Z,k) = \begin{cases} M_0 & Z \leq 100 \\ \dfrac{\sum\limits_{j=1}^{k_i} n_j(Z)M_j}{\sum\limits_{j=1}^{k_i} n_j(Z)} & Z > 100 \end{cases} \tag{92}$$

$$h_i(Z) = Q_i \left(Z - U_i \right)^2 e^{-W_i\left(Z-U_i\right)^3} + q_i \left(u_i - Z \right)^2 e^{-w_i\left(u_i-Z\right)^3} \tag{93}$$

and values for α_i, a_i, b_i, Q_i, U_i, W_i, q_i, u_i, and w_i are listed in Table 11, Table 12, and Table 13. For verification purposes, a plot of $D_i(Z)$ for each species is reproduced in Figure 79.

Table 11: Species dependent constants for thermal diffusion and molecular diffusion coefficients (NOAA, NASA, USAF, 1976, p. 5).

Sub-script i	Species	α_i	a_i	b_i
1	N_2	0.00	----	----
2	O	0.00	6.986×10^{20}	0.750
3	O_2	0.00	4.863×10^{20}	0.750
4	Ar	0.00	4.487×10^{20}	0.870
5	He	-0.40	1.700×10^{21}	0.691
6	H	-0.25	3.305×10^{21}	0.500

Table 12: Species dependent coefficients for empirical expression of flux term for computing number density (NOAA, NASA, USAF, 1976, p. 5).

Sub-script i	Species	Q_i	U_i	W_i
2	O	-5.809644×10^{-4}	56.90311	2.706240×10^{-5}
3	O_2	1.366212×10^{-4}	86.000	8.333333×10^{-5}
4	Ar	9.434079×10^{-5}	86.000	8.333333×10^{-5}
5	He	-2.457369×10^{-4}	86.000	6.666667×10^{-4}

Table 13: Additional species dependent coefficients for empirical expression of flux term for computing number density (NOAA, NASA, USAF, 1976, p. 5).

Sub-script i	Species	q_i		u_i	w_i
2	O	-3.416248×10^{-3}	$86 \leq Z \leq 97$	97.0	5.008765×10^{-4}
		0.0	$Z > 97$		
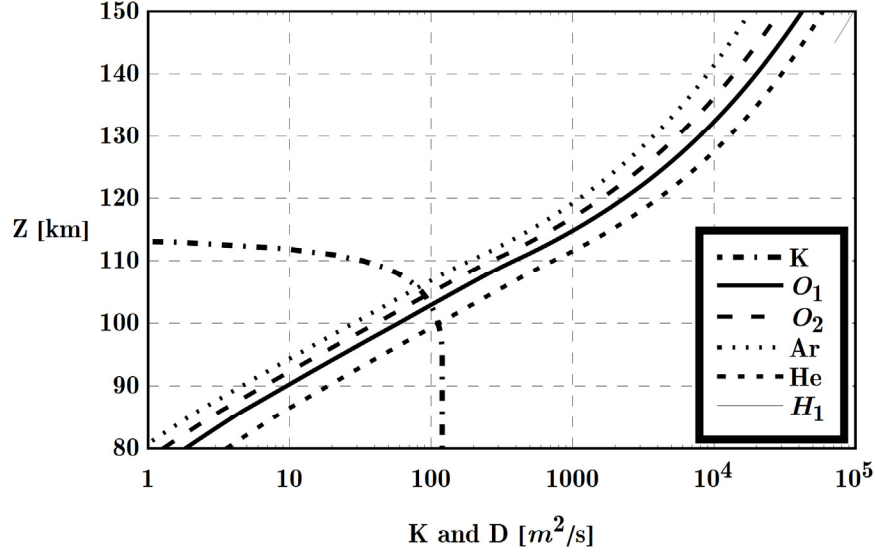
Figure 79: Eddy diffusion (K) and molecular diffusion (O_1, O_2, Ar, He, H_1) coefficients as a function of geometric altitude.

Beginning with molecular Nitrogen $(i = 1)$, (87) is reduced to

$$n_1(Z) = n_1^{86} \frac{T_7}{T(Z)} e^{-\int_{Z_7}^{Z} \frac{\bar{M}_i(Z)g(Z)}{R^* T(Z)} dZ} \tag{94}$$

after applying assumptions and approximations from (NOAA, NASA, USAF, 1976, p. 13). Number densities of atomic and molecular Oxygen $(i = 2, 3)$ may then be computed using (87) and the number density of molecular Nitrogen, followed by Argon and Helium $(i = 4, 5)$ using (87) and the accumulated number densities of molecular Nitrogen, and atomic and molecular Oxygen (NOAA, NASA, USAF, 1976, pp. 13-14). Finally, the number density for atomic Hydrogen $(i = 6)$ is

$$n_6(Z) = \begin{cases} 0 & Z < 150 \\ n_6^{150 \to 500}(Z) & 150 \leq Z < Z_{11} \\ n_6^{500} & Z \geq Z_{11} \end{cases} \tag{95}$$

where

$$n_6^{150 \to 500}(Z) = \left(n_6^{500} - \int_{Z_{11}}^{Z} \frac{\phi p_6(Z,1)}{D_6(Z)} dZ \right) p_6(Z,-1) \tag{96}$$

with

$$p_6(Z,c) = \left(\frac{T(Z)}{T_{11}} \right)^{c(1+\alpha_6)} e^{c \int_{Z_{11}}^{Z} \frac{\bar{M}_6(Z)g(Z)}{R^*T(Z)} dZ} \tag{97}$$

and ϕ is the vertical flux of atomic Hydrogen (7.2×10^{11} m^{-2}·s^{-1}) (NOAA, NASA, USAF, 1976, p. 14). Computed number densities for all species as a function of geometric altitude are plotted in Figure 80.
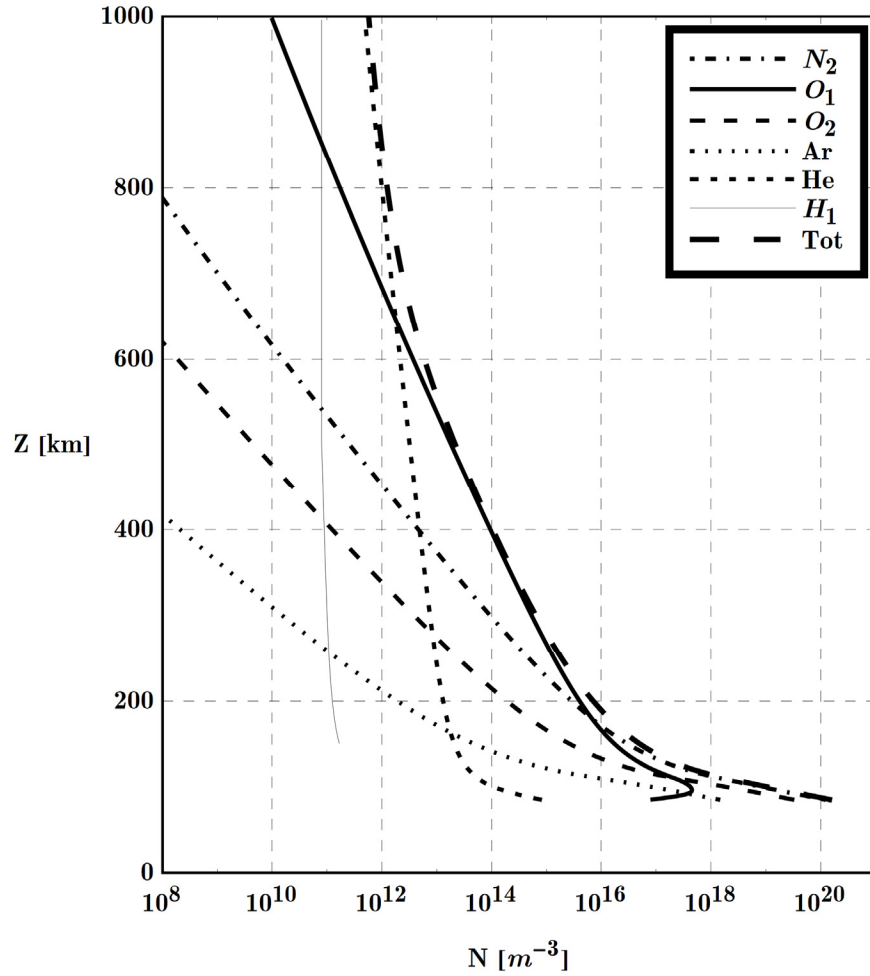
Figure 80: Number density of individual species and total number density as a function of geometric altitude. Reproduces Fig. 5 from (NOAA, NASA, USAF, 1976, p. 13).

Evaluating (86) using the appropriate combinations of (87) through (97), the atmospheric density up to 1000 km is plotted in Figure 81.
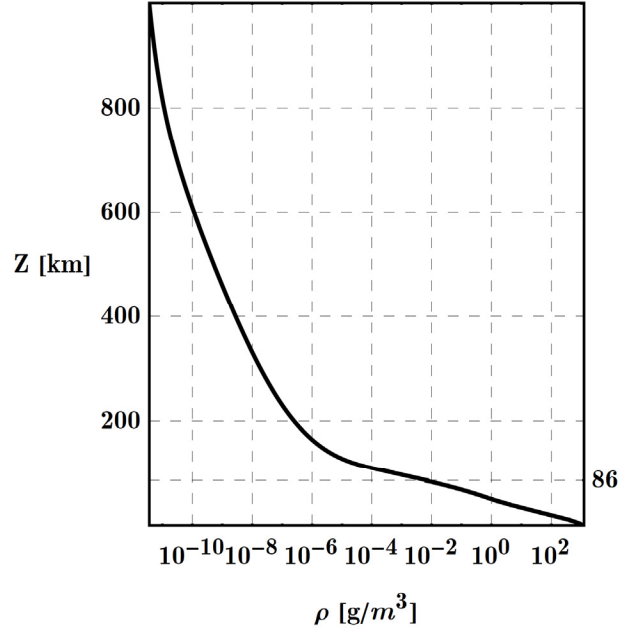
Figure 81: Atmospheric density as a function of geometric altitude above 86 km.

Composition

The relative fractional composition of any species i at geometric altitude Z above 86 km is

$$F_i(Z) = \frac{n_i(Z)}{\sum n_j(Z)}. \tag{98}$$

A Note on Implementation Above 86 km

The calculation of density and composition for the atmosphere above 86 km takes considerable effort. The difficulty is in the series of diffusion problems required to compute the number density of each species. Equation (94) is evaluated for the number density of Nitrogen, but the follow calculations for both

molecular and atomic Oxygen use the number density of nitrogen as a background gas for the diffusion problem solved by evaluation of (87):

Evaluation of (87) by numerical quadrature requires evaluation of (94) at each quadrature point. The computational effort progresses geometrically for Argon and Helium which use Nitrogen and both species of Oxygen as the background gas for the diffusion problem: Evaluation of (87) requires a separate evaluation of itself for each species of Oxygen, each requiring evaluation of (94)… and so on and so forth. The computational effort for even a single number density of Hydrogen is considerable. It is possible to craft the implementation to avoid duplication of effort at the cost of an ever-increasingly complex code structure, but the computational cost of directly computing the number density of species in the atmosphere remains considerable no matter how clever and devious the code designer may be.

To support a Monte Carlo code where the cost of evaluating the atmospheric density function may drive simulation time, I recommend precomputing a table of number densities for each species (much like what was used to generate Figure 80) and choosing an appropriate interpolation scheme. Interpolation error may be managed by selection of the interpolation method and the grid on which number densities are computed and stored, but the slow-down of the Monte Carlo code avoided by precomputing a table of number densities.

Bibliography

Bate, R. R., Mueller, D. D., & White, J. E. (1971). *Fundamentals of Astrodynamics.* New York: Dover Publications, Inc.

Conway, B. A. (1986). An Improved Algorithm Due to Laguerre for the Solution of Kepler's Equation. *Celestial Mechanics, 39*, 199-211.

Cullen, D. E. (2004). *Sampling ENDL Watt Fission Spectra.* Technical Report 203351, University of California, Lawrence Livermore National Laboratory, Livermore, CA.

Dailey, W. T. (2011). *Ray Next-Event Estimator Transport of Primary and Secondary Gamma Rays.* MS Thesis, AFIT/GNE/ENP/11-M04, Air Force Institute of Technology (AU), Wright-Patterson AFB.

Gooding, R. H. (1988). *On the Solution of Lambert's Orbital Boundary-Value Problem.* RAE Technical Report 88027, Royal Aerospace Establishment, London.

Gooding, R. H. (1990). A Procedure for the Solution of Lambert's Oribital Boundary-Value Problem. *Celestial Mechanics and Dynamical Astronomy, 48*, 145-165.

Gooding, R. H., & Odell, A. W. (1988). The Hyperbolic Kepler Equation (and the Elliptic Equation Revisited). *Celestial Mechanics, 44*(3), 267-282.

IAEA. (2017). Evaluated Nuclear Data File (ENDF). Vienna, Austria: International Atomic Energy Agency. Retrieved from https://www-nds.iaea.org/exfor/endf.htm

Kalos, M. (1963). On the Estimation of Flux at a Point by Monte Carlo. *Nuclear Science and Engineering, 16*, 111-117.

Knief, R. A. (2008). *Nuclear Engineering: Theory and Technology of Commercial Nuclear Power* (2nd ed.). La Grange Park, Il: American Nuclear Society.

Lancaster, E. R., & Blanchard, R. C. (1969). *A Unified Form of Lambert's Theorem.* Goddard Space Flight Center. Washington D.C.: National Aeronautics and Space Administration.

LANL. (2015, September). *A General Monte Carlo N-Particle (MCNP) Transport Code.* Retrieved from Los Alamos National Laboratory: https://mcnp.lanl.gov/

Lewis, E. E., & Miller, J. W. (1993). *Computational Methods of Neutron Transport.* La Grange Park, IL: American Nuclear Society, Inc.

Lux, I., & Koblinger, L. (1991). *Monte Carlo Particle Transport Methods: Neutron and Photon Calculations.* Boca Raton, FL: CRC Press, Inc.

Mathews, K. A. (2013-2017). *High Altitude / Space Transport Estimator for Neutrons.* Working Paper, Air Force Institute of Technology.

Mathews, K. A. (2014-2017). Personal Communications: High Altitude Space Transport Estimator for Neutrons (HASTE-n). Wright Patterson AFB, OH.

Morris, D. N., & Benson, P. (1963). *Data for ICBM Re-entry Trajectories.* Santa Monica, CA: The RAND Corporation.

NASA. (1976). *The 1976 Standard Atmosphere Above 86km: Recomendations of Task Group II to COESA.* Washington D.C.

NNDC. (2009). *ENDF-6 Formats Manual.* National Nuclear Data Center. Upton, NY: Brookhaven National Laboratory.

NOAA, NASA, USAF. (1976). *U.S. Standard Atmosphere 1976.* Washington D.C.

Romano, P. K., & Trumbull, T. H. (2014). Comparison of algorithms for Doppler broadening pointwise tabulated cross sections. *Annals of Nuclear Energy*, 358-364.

Serebrov, A. P., Varlamov, V. E., Kharitonov, A. G., Fomin, A. K., Pokotilovski, Y. N., Geltenbort, P., . . . Zherebtsov, O. M. (2008). Neutron lifetime measurements using gravitationally trapped ultracold neutrons. *Physical Review C, 78*(3).

Solbrig, A. W. (1961). Doppler Effect in Neutron Absorption Resonances. *American Journal of Physics, 29*(4), 257-261.

Vallado, D. A. (2001). *Fundamentals of Astrodynamics and Applications* (2nd ed.). El Segundo, CA: Microcosm Press.

Wolfram Research, I. (2017). Mathematica. (Version 11.1). Champagne, Illinois: Wolfram Research, Inc.

Yue, A. T., Dewey, M. S., Gilliam, D. M., Greene, G. L., Laptev, A. B., Nico, J. S., . . . Wietfeldt, F. E. (2013). Improved Determination of the Neutron Lifetime. *Physical Review Letters, 111*(22).

REPORT DOCUMENTATION PAGE

Public reporting burden for this collection of information is estimated to average 1 hour per response, including the time for reviewing instructions, searching existing data sources, gathering and maintaining the data needed, and completing and reviewing this collection of information. Send comments regarding this burden estimate or any other aspect of this collection of information, including suggestions for reducing this burden to Department of Defense, Washington Headquarters Services, Directorate for Information Operations and Reports (0704-0188), 1215 Jefferson Davis Highway, Suite 1204, Arlington, VA 22202-4302. Respondents should be aware that notwithstanding any other provision of law, no person shall be subject to any penalty for failing to comply with a collection of information if it does not display a currently valid OMB control number. **PLEASE DO NOT RETURN YOUR FORM TO THE ABOVE ADDRESS.**

1. REPORT DATE *(DD-MM-YYYY)*	2. REPORT TYPE	3. DATES COVERED *(From - To)*
14-09-2017	PhD Dissertation	Oct 2014 - Sep 2017

4. TITLE AND SUBTITLE

Special Features of the Air-to-Space Neutron Transport Problem

5a. CONTRACT NUMBER

5b. GRANT NUMBER

5c. PROGRAM ELEMENT NUMBER

6. AUTHOR(S)

Dailey, Whitman T., Major, USAF

5d. PROJECT NUMBER

5e. TASK NUMBER

5f. WORK UNIT NUMBER

7. PERFORMING ORGANIZATION NAME(S) AND ADDRESS(ES)
Air Force Institute of Technology
Graduate School of Engineering and Management (AFIT/EN)
2950 Hobson Way, Building 640
Wright-Patterson AFB, OH 45433-7765

8. PERFORMING ORGANIZATION REPORT NUMBER

AFIT/ENP/DS-17-S-022

9. SPONSORING / MONITORING AGENCY NAME(S) AND ADDRESS(ES)
(intentionally left blank)

10. SPONSOR/MONITOR'S ACRONYM(S)

11. SPONSOR/MONITOR'S REPORT NUMBER(S)

12. DISTRIBUTION / AVAILABILITY STATEMENT
Distribution Statement A. Approved for Public Release; Distribution Unlimited

13. SUPPLEMENTARY NOTES
This material is declared a work of the U.S. Government and is not subject to copyright protection in the United States.

14. ABSTRACT
Special features of the air-to-space neutron transport problem are identified, characterized, and quantified to provide information on features that should be included in Monte Carlo simulations to obtain accurate predictions. Currently available codes and tools for Monte Carlo neutron transport calculations do not provide an adequate (in accuracy nor precision nor efficiency) framework for practical transport calculations in the context of the air-to-space neutron transport problem. A new Fortran code, High Altitude Transport to Space for Neutrons (HATS-n), is developed and tested to perform high fidelity Monte Carlo neutron transport calculations for this class of problems. Special features of the air-to-space neutron transport are identified and categorized: The influence of relative motions, the influence of gravity, the influence of the implementation of the atmosphere model, and the influence of radioactive decay of free neutrons. Each special feature is examined individually and methods and procedures are developed for research and practical implementations. Finally, the features are demonstrated in concert using the new HATS-n code.

15. SUBJECT TERMS
neutron transport, radiation transport, Monte Carlo

16. SECURITY CLASSIFICATION OF:			17. LIMITATION OF ABSTRACT	18. NUMBER OF PAGES	19a. NAME OF RESPONSIBLE PERSON
a. REPORT	**b. ABSTRACT**	**c. THIS PAGE**	UU	222	Dr. Kirk A. Mathews
U	U	U			**19b. TELEPHONE NUMBER** *(include area code)* (937) 602-8996

Standard Form 298 (Rev. 8-98)
Prescribed by ANSI Std. Z39.18